

A Large-Stroke Electrostatic Micro-Actuator

by

Shahrzad Towfighian

A thesis
presented to the University of Waterloo
in fulfillment of the
thesis requirement for the degree of
Doctor of Philosophy
in
Mechanical Engineering

Waterloo, Ontario, Canada, 2010

© Shahrzad Towfighian 2010

I hereby declare that I am the sole author of this thesis. This is a true copy of the thesis, including any required final revisions, as accepted by my examiners.

I understand that my thesis may be made electronically available to the public.

Abstract

Parallel-plate electrostatic actuators driven by a voltage difference between two electrodes suffer from an operation range limited to 30 % of the gap that has significantly restrained their applications in Microelectromechanical systems (MEMS). In this thesis, the travel range of an electrostatic actuator made of a micro-cantilever beam electrode above a fixed electrode is extended quasi-statically to 90% of the capacitor gap by introducing a voltage regulator (controller) circuit designed for low frequency actuation. The developed large-stroke actuator is valuable contribution to applications in optical filters, optical modulators, digital micro-mirrors and micro-probe based memory disk drives.

To implement the low-frequency large-stroke actuator, the beam tip velocity is measured by a vibrometer, the corresponding signal is integrated in the regulator circuit to obtain the displacement feedback, which is used to modify the input voltage of the actuator to reach a target location. The voltage regulator reduces the total voltage, and therefore the electrostatic force, once the beam approaches the fixed electrode so that the balance is maintained between the mechanical restoring force and the electrostatic force that enables the actuator to achieve the desired large stroke. A mathematical model is developed for the actuator based on the mode shapes of the cantilever beam using experimentally identified parameters that yields good accuracy in predicting both the open loop and the closed loop responses. The low-frequency actuator also yields superharmonic resonances that are observed here for the first time in electrostatic actuators.

The actuator can also be configured either as a bi-stable actuator using a low-frequency controller or as a chaotic resonator using a high-frequency controller. The high-frequency controller yields large and bounded chaotic attractors for a wide range of excitation magnitudes and frequencies making it suitable for sensor applications. Bifurcation diagrams reveal periodic motions, softening behavior, period doubling cascades, one-well and two-well chaos, superharmonic resonances and a reverse period doubling cascade. To verify the observed chaotic oscillations, Lyapunov exponents are calculated and found to be positive.

Furthermore, a chaotic resonator with a quadratic controller is designed that not only requires less voltage, but also produces more robust and larger motions. Another metric of chaos, information entropy, is used to verify the chaotic attractors in this case. It is found that the attractors have a common information entropy of 0.732 independent of the excitation amplitude and frequency.

Acknowledgements

I would like to show my gratitude to my supervisors, Prof. Eihab Abdel-Rahman and Prof. Glenn R. Heppler, whose guidance, encouragement, careful support and thorough attention from the beginning to the end made this research possible. I specially appreciate careful feedbacks and comments on my thesis from Prof. Eihab Abdel-Rahman.

I am so grateful to Prof. Amir Khajepour for his helpful advice and inspiration. I also wish to express my sincere thanks to Prof. Arsen Hajian for his great help of sharing the testing equipment making this study possible. Thanks to my committee members William Melek and David Wong for their suggestions.

I am also very thankful to my colleagues and co-workers for their assistance: Mohammad Basha, Abdulrahman Seleim, Mahmoud Khater, Yanhui Bai, Andrew Logan, and my friends for being there when I needed them: Nasim Paryab, Kamran Shavezipur, Sepehr Forouzanfar, Sara sharifian, and Ali Najafi-Sohi. I would like to acknowledge CMC Microsystems for providing fabrication services, NSERC for postgraduate scholarship, and CFI for financial support.

I am forever indebted to my parents Fatemeh and Sohrab for their kindness, constant support and continuous encouragements. Last but not least, to my husband Hasan, thank you for your true love, support and endless understanding during my studies, without which I could not make it through.

Dedication

To my beloved parents, Fatemeh and Sohrab

To my wonderful loving husband, Hasan

Table of Contents

List of Tables	ix
List of Figures	xvii
List of Symbols	xviii
1 Introduction	1
1.1 Overview	1
1.2 Motivation	2
1.3 Objectives	3
1.4 Thesis Outline	4
2 Background and Literature Survey	5
2.1 Electrostatic Micro-actuators	5
2.2 Extended stability in micro-electrostatic actuators	6
2.3 Chaotic micro-oscillator	11
2.3.1 Chaos	11
2.3.2 Applications of chaos	15
2.3.3 Nonlinear Dynamics in MEMS	17

3	System Model	23
3.1	Open-Loop Actuator	23
3.1.1	Static Analysis	29
3.2	Closed-loop Actuator	31
3.3	Static Response	33
3.3.1	Stable and Bi-stable Actuator	34
3.4	Eigenvalue Problem	41
3.5	Dynamic Response	43
3.5.1	Stable Actuator	43
3.5.2	Bi-stable Actuator	44
3.5.3	Force Sweep	48
3.5.4	Frequency Sweep	51
3.6	Actuator Realization	57
3.7	Summary	62
4	Low Frequency Experiment	63
4.1	Open Loop Actuator	63
4.1.1	Open Loop Experiment Configuration	63
4.1.2	Data Processing	65
4.1.3	Actuators	66
4.1.4	Parameter Identification	68
4.2	Closed Loop Actuator	76
4.2.1	Closed loop Experimental Set-up	76
4.2.2	Large-Stroke Actuator	77
4.3	Virtual regulator	88
4.4	Superharmonic Resonances	89
4.5	Summary	94

5	Quadratic Resonator Model	96
5.1	New Regulator Function	96
5.2	Actuator Model	98
5.3	Static Analysis	100
5.4	Dynamic Analysis	102
5.4.1	Force Sweep	104
5.4.2	Frequency Sweep	106
5.4.3	Information Entropy	108
5.5	Summary	110
6	Concluding Remarks	112
6.1	Thesis Contributions	112
6.2	Thesis Publications	113
6.2.1	Journal papers	113
6.2.2	Conference papers	114
6.3	Future Work	115
	APPENDICES	116
	A Publisher Permission	117
	References	119

List of Tables

3.1	Actuator series I parameters [1]	31
3.2	Beam dimensions corresponding to the α values used in Figure 3.7.	37
3.3	Eigenvalues for the fixed points at $V_{in} = 110$ V in Figure 3.11.	42
3.4	Actuator Series II parameters	58
4.1	The electrostatic actuator material properties	70
5.1	Actuator parameters	100
5.2	Eigenvalues of the equilibrium points at $V_{in} = 2$ V using the second controller design	101

List of Figures

2.1	Electrostatic actuator.	6
2.2	Polychromator grating [2].	7
2.3	Optical modulator [3].	8
2.4	Optical modulator two operating modes [3]: a) Frequency Modulation b) Amplitude modulation.	8
2.5	Leveraged bending method to increase the range of motion of a micro-cantilever [4].	9
2.6	A ball in double well potential [5].	12
2.7	Phase portrait [5].	12
2.8	a) projected phase space trajectories for chaotic oscillation of a ball rolling on a surface b) experimental 2D potential surface [6].	14
2.9	Poincaré maps for the displacement of a point on a buffeting panel for four perturbations of the stiffness of upstream spring [7].	16
3.1	Schematic of micro-beam oscillator.	24
3.2	FBD for a small element along the beam.	24
3.3	Nondimensional deflection of the beam tip versus DC voltage V_{DC}	30
3.4	Closed loop system.	32
3.5	Nondimensional deflection of the beam tip versus voltage, V_{in} for the closed-loop system.	35
3.6	Roots of the equilibrium equation q_1 in complex plane.	36

3.7	Roots of the one-mode equilibrium equation for a constant $G^2\alpha = 0.0002$.	37
3.8	Roots of the one-mode equilibrium equation Eq. (3.50) in the complex plane for different voltage gains.	38
3.9	Effect of the voltage gain G on the static deflection versus DC voltage, V_{DC} curve.	39
3.10	Stability diagram in the parameter space of voltage gain, G and voltage, V_{in} .	40
3.11	Effect of displacement gain, Ψ on static pull-in graph for $G = 0.8$	41
3.12	Nondimensional frequency versus input voltage V_{DC}	43
3.13	The nondimensional phase portrait and beam deflection, V_s for the system with gain of $G = 4$ in Figure 3.9, and excitations of $V_{AC} = 0$ V, $V_{DC} = 26.2$ V.	44
3.14	The phase portrait, beam tip deflection w_1 and controller output voltage, V_c for $\mu = 0.7$, $\omega = 3.5158$, $V_{AC} = 0.7$ V, and the initial conditions ($q_1 = 0.86$, $\dot{q}_1 = 0$, $V_c = 18.43$ V).	45
3.15	The phase portrait, beam tip deflection w_1 and controller output voltage, V_c for $\mu = 0.7$, $\omega = 3.5158$, $V_{AC} = 0.9$ V, and the initial conditions ($q_1 = 0.86$, $\dot{q}_1 = 0$, $V_c = 18.43$ V).	46
3.16	The phase portrait, beam displacement and controller output voltage for $\mu = 0.1$, $\omega = 4.45$, $V_{AC} = 0.86$ V and the initial conditions ($q_1 = 0.86$, $\dot{q}_1 = 0$, $V_c = 18.43$ V).	47
3.17	The phase portrait, beam displacement and controller output voltage for a three-mode model $\mu = 0.7$, $\omega = 2.8$, $V_{DC} = 100$ V, $V_{AC} = 0.9$ V, and the initial conditions ($q_1 = 0.91$, $\dot{q}_1 = 0$, $V_s = 35.7$ V).	47
3.18	The bifurcation diagram of the actuator constructed from a force sweep V_{AC} at the natural frequency of the lower equilibrium $\omega_l = 1.98 \equiv 86$ kHz.	49
3.19	The nondimensional phase portraits and fast fourier transforms (FFT) using a one-mode model, the system parameters $\mu = 0.7$, $\omega = 1.98 \equiv 86$ kHz, a) Period 1 $V_{AC} = 4.1$ V, b) Period 2 $V_{AC} = 4.4$ V, c) Period 4 $V_{AC} = 4.7$ V.	49
3.20	The nondimensional phase portrait and FFT of the chaotic attractor at $\mu = 0.7$, $\omega = 1.98 \equiv 86$ kHz, $V_{AC} = 4.861$ V.	50

3.21	Phase portrait of the period 10 orbit at an excitation amplitude $V_{AC} = 4.883$ V and the frequency of excitation $\omega_l = 1.98 \equiv 86$ kHz.	51
3.22	Phase portrait of a primarily one-well chaotic attractor at an excitation amplitude $V_{AC} = 4.9$ V and the frequency of excitation $\omega_l = 1.98 \equiv 86$ kHz.	51
3.23	The bifurcation diagram sweeping the frequency of excitation at $V_{AC} = 4$ V, single-sided Poincaré sections obtained at the period of excitation.	52
3.24	The bifurcation diagram sweeping the frequency of excitation at $V_{AC} = 4$ V, double-sided Poincaré sections obtained at the intersection with the zero velocity axis.	53
3.25	Phase portraits and FFT for the periodic orbits at the a) natural frequency of the lower equilibrium $\Omega = \omega_l = 1.98 \equiv 86$ kHz b) the superharmonic resonance of order two $\Omega = \frac{\omega_l}{2} = 0.99 \equiv 43$ kHz c) the superharmonic resonance of order three $\Omega = \frac{\omega_l}{3} = 0.66 \equiv 28$ kHz d) the superharmonic resonance of order six $\Omega = \frac{\omega_l}{6} = 0.33 \equiv 14$ kHz.	55
3.26	a) Phase portrait, b) Lyapunov exponent c) Displacement time history d) controller output voltage of the one-well chaotic attractor when $V_{AC} = 4$ V and $\Omega = 1.84$	56
3.27	a) Phase portrait, b) Lyapunov exponent c) Displacement time profile d) controller output voltage of the two-well chaotic attractor when $V_{AC} = 4$ V and $\Omega = 1.081$	57
3.28	Static profile for the actuator series II in Table 3.4.	58
3.29	The bifurcation diagram sweeping the nondimensional frequency of excitation at fixed $V_{DC} = 18.5$ V, $V_{AC} = 0.8$ V for the actuator series II in Table 3.4.	60
3.30	a) Phase portrait b) velocity time history c) controller output voltage d) displacement time history of the period four at $V_{DC} = 18.5$ V, $V_{AC} = 0.8$ V and $\Omega = 1.344 \equiv 34.5$ kHz for the actuator series II in Table 3.4.	60
3.31	a) Phase portrait b) velocity time history c) controller output voltage d) displacement time history of the chaotic attractor at $V_{DC} = 18.5$ V, $V_{AC} = 0.8$ V and $\Omega = 1.975 \equiv 58$ kHz for the actuator series II in Table 3.4.	61

3.32	a) Phase portrait b) velocity time history c) controller output voltage d) displacement time history of the chaotic attractor at $V_{DC} = 18.5$ V, $V_{AC} = 0.8$ V and $\Omega = 1.58 \equiv 46.4$ kHz for the actuator series II in Table 3.4. . . .	61
4.1	Experimental configuration.	64
4.2	Doppler effect principle	64
4.3	Two signals with frequencies of 0.1 Hz and 0.9 Hz appear identical under a sampling rate of 1 Hz. (Aliasing effect).	65
4.4	Layout of the actuators in MEMS Pro L-Edit software. a)Top view, b)cross section.	67
4.5	A white-light image of the electrostatic actuator by WYKO NT1100 Optical Profiler.	67
4.6	SEM image of the actuator fabricated with POLYMUMPS.	68
4.7	Frequency response of a beam with the nominal dimensions of $150 \times 10 \times 2$ μm and a capacitor gap of $2\mu\text{m}$ where the AC voltage is 2 V. Solid line shows the fitted data on the experimental results.	70
4.8	Natural frequency as a function of DC voltage for a beam with dimensions of $L = 166.1$ μm , $b = 10$ μm , $h = 2.2$ μm , and $d = 2.1$ μm : – Simulations, \diamond experimental results.	71
4.9	Compliance frequency response of a beam with dimensions of $150 \times 10 \times 2$ with gap of $2\mu\text{m}$ when the applied AC voltage is 2 V.	71
4.10	Frequency response of the beam tip velocity with dimensions of $L = 166.1$ μm , $b = 10$ μm , $h = 2.2$ μm , $d = 2.1$ μm at $V_{DC} = 9.07$ V, and $V_{AC} = 2$ V : – Simulations, \diamond experimental results, – fitted data on the experimental results.	72
4.11	Frequency response of a beam with the nominal dimensions of $175 \times 10 \times 2\mu\text{m}$ and a capacitor gap of $2\mu\text{m}$ where AC voltage is 1.30-1.4 V.	73
4.12	Compliance frequency response of a beam with dimensions of $175 \times 10 \times 2\mu\text{m}$ and a capacitor gap of $2\mu\text{m}$ where AC voltage is 1.30-1.4 V.	73

4.13	Natural frequency as a function of DC voltage for the beam with dimensions of $L = 185 \mu\text{m}$, $b = 10 \mu\text{m}$, $h = 1.9 \mu\text{m}$, and $d = 1.9 \mu\text{m}$:– Simulations, \circ experimental results.	74
4.14	Natural frequency versus DC voltage beam for the with dimensions of $125.6 \times 10 \times 1.9 \mu\text{m}$ with a gap of $1.8 \mu\text{m}$ where AC voltage is 1.7-1.76 V. \circ : experimental results, –: simulations.	75
4.15	Static response for a beam with the dimensions of $125.6 \times 19 \times 1.9 \mu\text{m}$ with a gap of $1.8 \mu\text{m}$	75
4.16	Schematic of the feedback control system	76
4.17	Closed loop displacement simulated response. Dashed line shows the location of unstable equilibrium points, the solid line shows the stable equilibrium location. (Beam dimension are $131 \times 20 \times 1.9 \mu\text{m}$, gap of $1.9 \mu\text{m}$, and controller parameters are $\Psi = 0.5 \text{ V}$, $G = 4.8$.)	78
4.18	Block diagram of the low frequency controller.	79
4.19	Schematic of the low frequency control circuit [8].	80
4.20	Picture of the low frequency control circuit.	81
4.21	Closed-loop response to an excitation of $v = 2.7 \text{ V}$, $\omega = 10 \text{ kHz}$. – – measured, – simulated. a) beam tip velocity, b) beam tip displacement up to 37%, c) controller voltage V_c , d) Regulated voltage $G(V_{in} - V_c)$. (Beam dimension are $131 \times 20 \times 1.9 \mu\text{m}$, the gap is $1.82 \mu\text{m}$, and the controller parameters are $\Psi = 0.5 \text{ V}$, $G = 4.8$.)	82
4.22	Closed-loop control response to excitation at $v = 2.69 \text{ V}$, $\omega = 10 \text{ kHz}$. – – measured, – simulated: a) beam tip velocity, b) beam tip displacement up to 54%, c) controller voltage V_c , d) regulated voltage $G(V_{in} - V_c)$. (Beam dimension are $131 \times 20 \times 1.9 \mu\text{m}$, the gap is $1.75 \mu\text{m}$, and controller parameters are $\Psi = 0.5 \text{ V}$, $G = 4.8$.)	83
4.23	Closed loop response to excitation at $v = 2.88 \text{ V}$, $\omega = 10 \text{ kHz}$. – – measured, – simulated: a) beam tip velocity, b) beam tip displacement up to 52%, c) controller voltage V_c , d) regulated voltage $G(V_{in} - V_c)$. (Beam dimension are $131 \times 20 \times 1.9 \mu\text{m}$, the gap is $1.9 \mu\text{m}$, and controller parameters are $\Psi = 0.5 \text{ V}$, $G = 4.8$.)	84

4.24	Closed loop response to excitation at $v = 2.92 V, \omega = 10kHz$. $--$ measured, $-$ simulated. a) beam tip velocity, b) beam tip displacement up to 67%, c) controller voltage V_c , d) Regulated voltage $G(V_{in} - V_c)$. (Beam dimension are $131 \times 20 \times 1.9 \mu m$, the gap is $1.9 \mu m$, and controller parameters are $\Psi = 0.5 V, G = 4.8$.)	85
4.25	Closed loop response to excitation at $v = 3 V, \omega = 10kHz$. $--$ measured, $-$ simulated. a) beam tip velocity, b) beam tip displacement up to 78%, c) controller voltage V_c , d) regulated voltage $G(V_{in} - V_c)$. (Beam dimension are $131 \times 20 \times 1.9 \mu m$, the gap is $1.9 \mu m$, and controller parameters are $\Psi = 0.5 V, G = 4.8$.)	86
4.26	Closed loop response to excitation at $v = 3.2 V, \omega = 10kHz$. $--$ measured, $-$ simulated: a) beam tip velocity, b) beam tip displacement up to 90%, c) controller voltage V_c , d) regulated voltage $G(V_{in} - V_c)$. (Beam dimension are $131 \times 20 \times 1.9 \mu m$, the gap is $1.9 \mu m$, and controller parameters are $\Psi = 0.5 V, G = 4.8$.)	87
4.27	Peak actuator displacement versus peak voltage ($2v$). $--$ simulated unstable equilibrium points, $-$ simulated stable equilibrium points, \circ experimental results. (Beam dimension are $131 \times 20 \times 1.9 \mu m$, gap of $1.9 \mu m$, and controller parameters are $\Psi = 0.5 V, G = 4.8$.)	88
4.28	Beam open loop response to a modified input waveform: a) Beam tip velocity b) Beam tip displacement c) Actuator input voltage. $--$ measured, $-$ simulated response to excitation at $v = 3 V, \omega = 10kHz$ for a beam with dimensions of $131 \times 20 \times 1.9 \mu m$ with the gap of $1.82 \mu m$, and controller simulated parameters of $\Psi = 0.5 V, G = 4.8$.)	89
4.29	The superharmonic resonance of order 8 obtained when the controller parameters are $G = 2, \Psi = 0.5 V$, and the excitation is $v = 3.56 V, \omega = 10 kHz$. a) beam tip velocity, b) beam tip displacement, c)Fast Fourier Transform of the tip velocity, d) Phase portrait.	90
4.30	The superharmonic resonance of order 6 obtained when the controller parameters are $G = 2, \Psi = 0.5 V$, and the excitation is $v = 3.56 V, \omega = 13 kHz$. a) beam tip velocity, b) beam tip displacement, c)Fast Fourier Transform of the tip velocity, d) Phase portrait.	91

4.31	The superharmonic resonance of order 5 obtained when the controller parameters are $G = 2$, $\Psi = 0.5 V$, and the excitation is $v = 3.55 V$, $\omega = 15.7 kHz$. a) beam tip velocity, b) beam tip displacement, c)Fast Fourier Transform of the tip velocity, d) Phase portrait.	92
4.32	The superharmonic resonance of order 4 obtained when the controller parameters are $G = 2$, $\Psi = 0.5 V$, and the excitation is $v = 2.78 V$, $\omega = 21.36 kHz$. a) beam tip velocity, b) beam tip displacement, c)Fast Fourier Transform of the tip velocity, d) Phase portrait.	93
4.33	The superharmonic resonances of an actuator with the nominal dimensions of $175 \times 10 \times 2 \mu m$ and a gap of $2 \mu m$ a) order 6 obtained at $V_{DC} = 5.2 V$, $V_{AC} = 4.7 V$, $\Omega = 13.3 kHz$, b) order 5 obtained at $V_{DC} = 5.2 V$, $V_{AC} = 4.16 V$, $\Omega = 16 kHz$, c) order 4 obtained at $V_{DC} = 5.2 V$, $V_{AC} = 3.88 V$, $\Omega = 20 kHz$, d) order 3 obtained at $V_{DC} = 5.2 V$, $V_{AC} = 3.32 V$, $\Omega = 26.6 kHz$	94
5.1	Graphical solution of Eq. 3.49 showing the balance of mechanical force and the regulated electrostatic force and a zoom at $V_{in} = 140.5 V$ for actuator parameters: Beam dimensions $200 \times 80 \times 4.5 \mu m$ and a gap of $3 \mu m$, controller gains $\Psi = 6 V$, $G = 0.65$, Modulus of Elasticity $E = 166 GPa$, Density $\rho = 2331 \frac{kg}{m^3}$. – left side of the equation, – – right side of the equation . . .	97
5.2	Graphical solution of Eq. 5.1 showing the balance of the mechanical force and the regulated electrostatic force at $V_{in} = 15 V$ for actuator parameters: Beam dimensions $200 \times 80 \times 4.5 \mu m$ and a gap of $3 \mu m$, quadratic function coefficients $n_0 = -205.2 V$, $n_1 = 1291.4 V$, $n_2 = -1293.6 V$, Modulus of Elasticity $E = 166 GPa$, Density $\rho = 2331 \frac{kg}{m^3}$. – left side of the equation, – – right side of the equation.	98
5.3	Controller output voltage V_c as a function of the nondimensional gap when controller coefficients are $\frac{a_0}{\sqrt{\alpha}} = 20.1939 V$, $\frac{a_1}{\sqrt{\alpha}} = 142.6973 V$, $\frac{a_2}{\sqrt{\alpha}} = 142.6973 V$	99
5.4	Nondimensional deflection of the beam tip versus input DC voltage when controller coefficients are $\frac{a_0}{\sqrt{\alpha}} = 3.8697 V$, $\frac{a_1}{\sqrt{\alpha}} = -88.0195 V$, $\frac{a_2}{\sqrt{\alpha}} = 104.78 V$ (first design).	101

5.5	Nondimensional deflection of the beam tip versus input DC voltage when controller coefficients are $\frac{a_0}{\sqrt{\alpha}} = 20.1939 \text{ V}$, $\frac{a_1}{\sqrt{\alpha}} = 142.6973 \text{ V}$, $\frac{a_2}{\sqrt{\alpha}} = 142.6973 \text{ V}$ (second design).	102
5.6	a) Phase portrait of chaotic oscillation , b) Nondimensional beam tip displacement, c) Controller output voltage V_c , for the second design and $\frac{K_I}{T} = 0.1776 \frac{1}{\text{s}}$, at $V_{DC} = 2 \text{ V}$, $V_{AC} = 1 \text{ V}$, $\Omega = 90.4 \text{ kHz}$. (Crosses show the location of saddles and circles show the location of nodes.)	103
5.7	Bifurcation diagram constructed from a force sweep of V_{AC} at $V_{DC} = 0$ at four different fixed frequencies. $\circ \Omega = 90.4 \text{ kHz}$, $\times \Omega = 91.8 \text{ kHz}$, $\square \Omega = 93.22 \text{ kHz}$, and $\cdot \Omega = 94.64 \text{ kHz}$	105
5.8	a) Phase portrait of chaotic oscillation , b) nondimensional beam tip deflection, c) controller output voltage V_c , for the second design and $\frac{K_I}{T} = 0.1776 \frac{1}{\text{s}}$, at $V_{DC} = 0 \text{ V}$, $V_{AC} = 1 \text{ V}$, and $\Omega = 90.4 \text{ kHz}$. The cross shows the location of saddle and the circle shows the location of stable equilibrium point.	106
5.9	Bifurcation diagram constructed from a frequency sweep at $V_{AC} = 1.23 \text{ V}$ and $V_{DC} = 0$	107
5.10	Bifurcation diagram constructed from a frequency sweep at $V_{AC} = 1 \text{ V}$ and $V_{DC} = 0$	108
5.11	Information entropy for the chaotic attractor of the second design $\frac{K_I}{T} = 0.1776 \frac{1}{\text{s}}$ at $V_{DC} = 0 \text{ V}$, $V_{AC} = 1 \text{ V}$, and $\Omega = 90.4 \text{ kHz}$. The initial conditions are q_0 at equal increments between $[0.28-0.66]$, \dot{q}_0 is constant at 0.1 , and $V_{c0} = 0 \text{ V}$	109
5.12	Information entropy for the chaotic attractor of the second design $\frac{K_I}{T} = 0.1776 \frac{1}{\text{s}}$ at $V_{DC} = 0 \text{ V}$, $V_{AC} = 1.8 \text{ V}$, and $\Omega = 94.64 \text{ kHz}$. The initial conditions are q_0 at equal increments between $[0.28-0.66]$, \dot{q}_0 is constant at 0.1 , and $V_{c0} = 0 \text{ V}$	110

List of Symbols

Symbols are listed in alphabetical order.

A	Cross section area
E	Modulus of Elasticity
G	Voltage gain
I	Area moment of inertia
K_I	Integrator gain
L	Beam Length
q_n	n^{th} generalized coordinate
V_{AC}	Input AC voltage
V_{DC}	Input DC voltage
V_{in}	Input voltage
V_c	Controller output voltage
b	Beam Width
c	Damping coefficient
d	Initial gap
h	Beam thickness
r	Controller damping
t	Time in seconds
T	Time constant
\hat{t}	Nondimensional time
\hat{w}	Beam deflection in the normal direction to the beam
w	Nondimensional beam deflection in the normal direction to the beam
α	Electromechanical coupling coefficient
Ψ	Displacement gain
Φ_n	n^{th} mode shape of a straight beam
ρ	Density
μ	Normalized damping coefficient
ε_0	Permittivity of free space
ω	Normalized circular frequency of excitation

Chapter 1

Introduction

1.1 Overview

Parallel-plate electrostatic actuators are restricted to an operation range 1/3 of the capacitor gap. Such a drawback excludes many applications such as optical devices. A large-stroke electrostatic micro-actuator is developed in this study that can operate up to 90% of the gap. The travel range is extended, from the previously reported quasi-static actuation range of 60% of the gap [9], using a voltage regulator (controller). The actuator is implemented by connecting the MEMS resonator to an electronic voltage controller circuit that uses the feedback of beam tip velocity measured by a vibrometer. The voltage regulator reduces the voltage and hence the electrostatic force magnitude at large deflections to balance it with the mechanical restoring force. The controller can be configured to have two stable and one unstable equilibrium points (bi-stable) or one stable and one unstable equilibrium points. The large-stroke actuator is developed from the configuration with one stable and one unstable equilibrium points located close to the substrate. A mathematical model is also developed for the actuator to predict the system behavior.

The bi-stable actuator is used to produce chaos. A detailed study of the chaotic resonator is presented that include finding amplitudes and frequencies for steady-state chaotic oscillations in one and two wells arising from cascades of period-doubling bifurcations. The chaotic metrics of Fast Fourier Transform (FFT), Lyapunov exponent and the information entropy are used to verify and measure the irregularity of chaotic vibrations. A quadratic

controller is also introduced to reduce the operating voltages and to simplify the implementation of the controller circuit. The new resonator show an intermittent route to chaos in one potential well. This study presents a useful source for researchers studying use of MEMS nonlinear resonators.

1.2 Motivation

Due to their ease of fabrication and low cost, electrostatically actuated MEMS have been widely used in optical devices [2, 3, 10, 11], digital micro-mirrors [12–14], data storage systems [15], and telecommunication devices [16]. The main drawback of parallel-plate electrostatic actuation is their limited range of static actuation up to 33% of the gap, beyond which the actuator loses stability as the mechanical restoring force is over-powered by the electrostatic force and the actuator pulls into the substrate. Methods have been proposed to extend the travel range of electrostatic actuators, including the leveraged bending [4], series capacitor [17], and current control [18]. Charge and current control are very difficult to perform in MEMS because of very small capacitance magnitudes and other methods require high actuation voltage, on the order of five times the pull-in voltage. However, using a closed loop control system with controller output less than 10 V, Lu and Fedder [9] actuated up to 60% of the gap in parallel-plate electrostatic actuators. The lack of a method that requires relatively small voltage and can extend the travel range to the entire gap of a parallel-plate electrostatic actuator motivated this study. A comprehensive study of the literature on the travel extension is presented in Chapter 2.

Large-stroke electrostatic actuators are also of interest from the point of view of nonlinear dynamics. Due to the nonlinear electrostatic force, MEMS electrostatic actuators are inherently highly nonlinear. One can benefit from this behavior to develop nonlinear chaotic resonators that show higher sensitivity to system parameter changes. One of the applications of the chaotic resonator, reported by Yin et al. [19], is detection of corrosion in macroscale piezoelectric beam with the dimensions $280 \times 15 \times 1.27$ mm. It was converted to a van der Pol oscillator using a nonlinear feedback control system. Using the sensitivity vector and probability density function methods, they detected mass variations as small as 0.07% of the beam mass. Despite few applications of chaos in macroscale, there is no evidence of chaos applications in MEMS because of the complex dynamic behavior of these

systems. An investigation of a MEMS nonlinear oscillator that shows sustained chaotic oscillations would be a valuable asset in this area that can open doors to new applications benefiting from nonlinear behavior rather than avoiding it.

1.3 Objectives

The objectives of this study are classified into three main subjects:

- **Development of a mathematical model for an electrostatic micro-actuator**

Using mode shapes of a micro-cantilever beam, a mathematical model for a parallel-plate electrostatic actuator consisting of a moving cantilever beam above a fixed electrode is presented. The continuous equations of motion including the electrostatic forcing, damping and restoring forces are converted to discrete equations using separation of variables and Galerkin's method to study the beam tip motion. The model accuracy is improved from the lumped model commonly used elsewhere.

- **Development of a large-stroke parallel-plate electrostatic actuator**

To extend the actuation range of parallel-plate electrostatic actuators to the entire gap, a voltage regulator (controller) is added to the micro-actuator. The control law originated by Lu and Fedder [9] is employed to a simplified structure of a micro-cantilever beam rather than the complex structure of a suspended plate with meandering springs. The system model takes into account all the nonlinearities of the system instead of the linear model originally used. Not only the control law is simplified for low frequency applications, but also the actuator is implemented differently using an optical sensor and an analog controller circuit rather than using a capacitive sensor and a variable gain. Using the modified system, quasi-static actuation ranges larger than the reported 60% are targeted. Large stroke actuators are beneficial for optical sensors, and memory devices applications.

- **Development of a chaotic micro-resonator**

A chaotic micro-resonator is developed and the bifurcation diagrams are obtained to illustrate operating voltage and frequency ranges for period doubling, one-well and

two-well chaos as well as periodic responses. The leading Lyapunov exponent and FFT are used to verify the existence of chaos.

A second generation voltage regulator is also introduced demonstrating superior performance. The chaotic micro-resonator requires less voltage and produces larger motions. It would also have less noise in the electronic circuit as the singularity of the previous controller is removed. Further, the new controller can tune the size and location of potential wells. Chaotic oscillations can be created in one or two potential wells. Another chaotic metric, information entropy, is used to verify the existence of chaotic attractors. The chaotic resonator has the potential to be used in secure communication systems, random number generators or high resolution mass detection sensors using the applied chaotic metrics.

1.4 Thesis Outline

This thesis is divided to 6 Chapters. Chapter 2 summarizes the literature on extended stability electrostatic actuators and chaotic resonators. Chapter 3 develops the model of the closed loop. Chapter 4 presents the fabrication, experimental setup, and implementation of the large-stroke actuator. Chapter 5 describes a new quadratic controller with improved performance. Finally Chapter 6 summarizes the contributions and presents future work.

Chapter 2

Background and Literature Survey

2.1 Electrostatic Micro-actuators

Microelectromechanical systems (MEMS) grew during the past decade due to their small size, low energy consumption, and ease of fabrication. One of the common actuation methods used in these devices is electrostatic actuation. The electrostatic actuator most commonly used is a variable capacitor consisting of a fixed and a moving electrode that is driven by the voltage difference between the two electrodes (see Figure 2.1). The position of the moving electrode is determined by the balance of the mechanical restoring force and the electrostatic force. The electrostatic force between the two completely overlapping electrodes is defined as

$$f_e = \frac{\varepsilon_0 b L V^2}{2(d-w)^2} \quad (2.1)$$

where w is the moving electrode displacement in the z -direction, and ε_0 is the permittivity of the air. Other parameters are shown in Figure 2.1. The moving electrode can be a rigid mass supported by a spring or a cantilever beam, where the mechanical restoring force is the spring force of the beam that tends to bring the beam to the undeflected position.

MEMS electrostatic actuators are widely used with applications found in micro-switches for telecommunication [16], micro-mirrors for pattern recognition [3], and digital micro-mirrors for projection in television applications [12–14]. Two aspects targeting the applicability improvement of such devices are investigated in this thesis. The first aspect addresses the main drawback of such systems that is the pull-in instability restricting

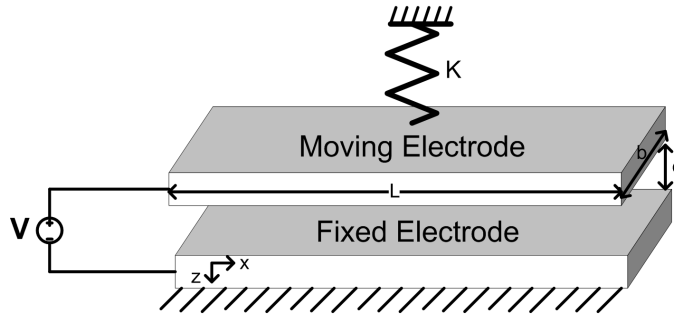


Figure 2.1: Electrostatic actuator.

the static and dynamic actuator motions to one third, and two thirds of the electrostatic gap [20], respectively. Such limitations prevent these actuators from reaching their full potential. The second aspect focuses on development of a chaotic micro-oscillator for use as a sensor. The two aspects of this research are carried out by adding feedback control systems to the electrostatic actuator to control the actuator voltage. The feedback control plays two roles:

- extending the stable operation of the actuator, and
- creating a chaotic micro-resonator.

A summary of current literature on both research topics follows.

2.2 Extended stability in micro-electrostatic actuators

Extending the range of electrostatic actuation is desired for many applications including MEMS optical switches [11], tunable laser diodes for long-distance optical fiber communications [10], polychromator gratings [2], optical modulators [3], and millipede data storage systems [15]. The examples of polychromator gratings [2] and optical modulators [3] are explained to emphasize the application of large range electrostatic actuation. Polychromator gratings [2] are programmable optical filters that are designed to pass light with a specific wavelength. A schematic of these filters is shown in Figure 2.2. In this filter, the mirrors

are perpendicular to the input light direction and are positioned at relative controllable vertical distances to allow a particular output. The mirrors are driven electrostatically and a large actuation range is needed to enable the filter to pass light within the spectroscopic wavelength range as the maximum wavelength is proportional to the maximum actuation range [4]. Another example is the light modulator shown in Figure 2.3 that consists of one fixed and one moving electrode that is attached to a micro-mirror. The mirror can modulate the amplitude or the frequency of the incident light depending on the excitation voltage configuration shown in Figure 2.4. Exciting the top electrode and one of the bottom electrodes, the mirror tilts and acts as an amplitude modulator (see Figure 2.4 b), while exciting the top electrode and both of the bottom electrodes, the mirror moves down and acts as a frequency modulator (see Figure 2.4 a). In the frequency modulation mode, the actuator motion is limited to one-third of the gap which significantly reduces the functionality of the device in image correction applications [3].

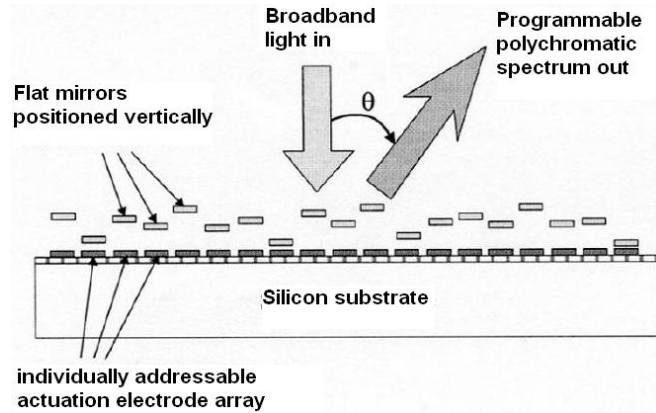


Figure 2.2: Polychromator grating [2].

To extend the travel range of electrostatic actuators beyond the conventional one-third of the gap, researchers used methods including: series capacitors [17], leveraged bending [4], and control circuitry [9]. Using a capacitor in series, Chan et al. [17] increased travel up to 60% of the gap experimentally with the price of high voltage requirements. Adding a capacitor in series with double the gap, they kept the electrostatic force constant in the original actuator by controlling the voltage difference between actuator plates. As the gap decreases in the actuator because of the actuator motion beyond 30% of the gap, its capacity increases rapidly, while the voltage across the actuator plates decreases as

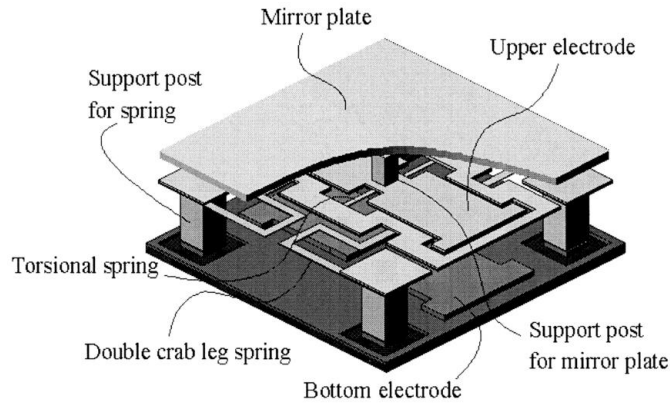


Figure 2.3: Optical modulator [3].

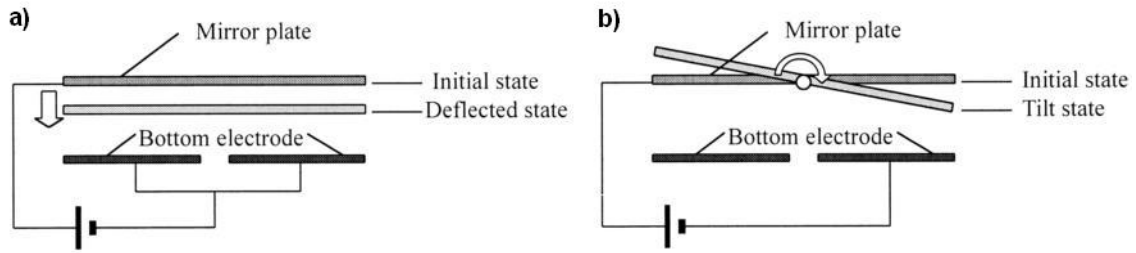


Figure 2.4: Optical modulator two operating modes [3]: a) Frequency Modulation b) Amplitude modulation.

the square of the actuator gap in the electrostatic force expression helping to keep the electrostatic force constant (Equation 2.1). Theoretically, it should have been possible to operate over the full gap of the actuator, but the challenges they faced in realizing the system, including parasitic capacitances, limited the range to 60% of the gap.

Leveraged bending [4] is another method to increase the actuation range that applies the electrostatic force only to a portion of the actuator (see Figure 2.5). For example in a cantilever beam actuated with a fixed electrode beneath it, the electrode is placed under the half-span closer to the support so that the beam tip can move the entire gap. The disadvantage of this method is also the high input voltage required.

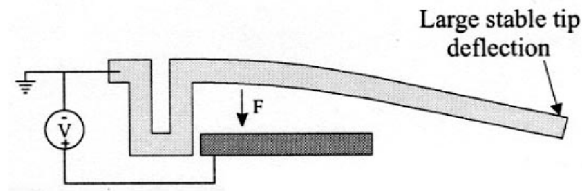


Figure 2.5: Leveraged bending method to increase the range of motion of a micro-cantilever [4].

There are a few studies on charge control [21, 22], current control [18], and voltage control [23, 24], that seek to extend the travel range of the electrostatic actuators. Other approaches include sliding mode control [25], and different nonlinear feedback controllers [26–28].

Using voltage control, Chen et al. [23] stabilized the tilt angle of an electrostatic micro-mirror beyond its pull-in angle. They control the actuation voltage to always make the slope of the mechanical torque larger than the electrostatic torque in the static torque versus tilt angle curve to stabilize the angle of the mirror. To do that, they choose a target angle beyond pull-in, and regulate the voltage in such a way that the voltage is set to a value slightly above the pull-in voltage once the angle is less than the target angle and it declines linearly once the angle goes beyond the target angle. They use the tilt angle feedback, measured by an optical position sensor, to dynamically change the voltage to achieve a desired angle. They were able to extend the stable operation range to 10° from an open-loop pull-in angle of 6.1° . Simulation studies correlated well with experiments at low actuation angles, but at large actuation angles, the linear mechanical and damping force models could not predict the overshoot accurately.

Current control is examined by Guardia et al. [18]. They used two configurations of open loop and closed loop for driving the actuator with a current source. They analyzed the current driving method and showed full gap actuation is achievable with voltage five times the open-loop pull-in voltage, less than the voltage required for the voltage driving method. Experimentally they obtained actuation up to 48% of the gap compared to an open-loop pull-in at 30%. The drawback of this method was that the actuator was stable for a short period of time.

There are a number of studies using charge control for extending electrostatic actuation

[21, 22]. Using a switched-capacitor circuit, Seeger et al. [22] controlled the charge of an electrostatic actuator. They showed analytically that the pull-in instability can be eliminated by taking advantage of parasitic capacitance present in the actuator employing 5.2 smaller voltage compared to voltage controlled systems. They experimentally achieved 83% of the gap. However, tip-in instability, which arises from a small rotation of the parallel plate actuator, and snapping could not be eliminated using this technique.

Using charge control with static and dynamic feedback, Maithripala et al. [21] improved the transient response of the MEMS electrostatic actuator and stabilized the actuator around any equilibrium point over the gap. The control method was based on input-output linearization and proved to reduce the control voltage. The study of the controller was further expanded [29] to yield a general control model to both stabilize and enhance realization of the system. Two general control techniques are introduced. The first uses voltage and charge feedbacks to stabilize the system. The second uses velocity feedback predicted by an observer to impose mechanical damping to control transients.

Employing a nonlinear voltage controller that uses two control methods, feedback linearization and trajectory planning, Agudelo et al. [24] experimentally achieved actuation beyond pull-in for an electrostatic micro-mirror up to 60% of the gap. They used feedback of the mirror tilt angle and the actuation voltage to follow the desired angle beyond pull-in and obtained good agreement with simulation. Simulation also showed actuation in the whole gap, which was limited in practice by the sampling time restricting the actuation to 60%.

A nonlinear output tracking controller is proposed by Owusu et al. [27] to extend the electrostatic actuation range using the feedback of actuator displacement, velocity and charge. Simulations showed robust response in the presence of noise and an increased actuation range to 90%. Further studies on the controller were conducted by Nikpanah et al. [28] who improved the performance of the controller. They eliminated the displacement fluctuations present in the previous study using a switching control technique that made the controller feasible to implement.

An adaptive controller has also been proposed by Piyabongkarn et al. [26] to extend the actuation range of a comb drive electrostatic actuator. The controller is designed to counteract fabrication imperfections in the device. They were able to operate up to 77% of the gap using position feedback of the micro-actuator to generate an electrostatic force

that eliminates the system nonlinearity. Using this method, the poles of the plant are canceled by the zeros of the nonlinear controller making the system behave like a linear system.

2.3 Chaotic micro-oscillator

2.3.1 Chaos

Chaos is an aperiodic behavior in a deterministic nonlinear dynamic system, such that the system response does not cross the same point in the phase plane twice while staying within a bounded region of the phase plane. That means that the motion has infinite period. Chaos can only be realized in systems with three or more degrees of freedom [5]. The system response shows sensitivity to initial conditions. That is, in chaotic systems, two trajectories starting close to each other in phase space, will move exponentially away from each other over a very short amount of time [30].

A system with two potential wells, that is a bi-stable system with two stable equilibrium points is a typical system used to produce chaotic oscillation. The behavior of a bi-stable system is simply represented by Strogatz [5] for a damped particle moving along a one dimensional potential field with two wells and a hump that corresponds to the two stable equilibria and the unstable equilibrium at the middle, respectively (Figure 2.6). The system is shaken periodically from side to side. Once the shaking is weak, the particle oscillates at the bottom of either well depending on the initial conditions. When the shaking energy is strong, the particle jumps over the hump from one well to the other for any initial conditions. There is a specific intermediate energy where the particle shows random oscillations, that is passing over the hump to the other well; oscillating in one well and coming back to the other well; staying for a while and jumping to the other, which indicates chaotic oscillations. A projected phase space trajectory of chaotic oscillation for the particle is depicted in Figure 2.7. The figure illustrates a typical chaotic attractor that has an appearance similar to butterfly wings.

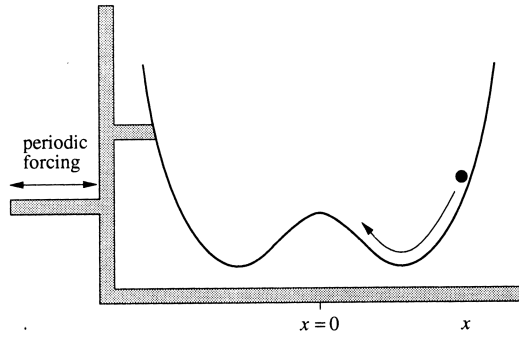


Figure 2.6: A ball in double well potential [5].

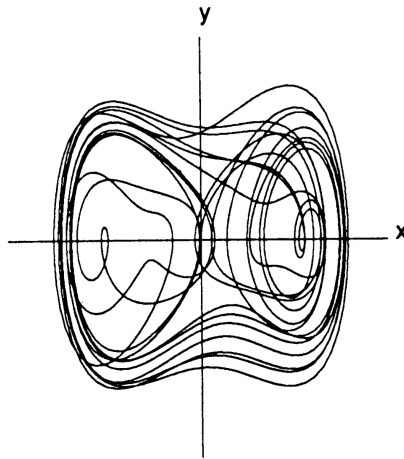


Figure 2.7: Phase portrait [5].

Chaos has been observed experimentally by Holmes and Moon [31, 32] in bending of a beam under temporally periodic loading. Magnetic forces were used to bend a beam that is clamped at one end in a rigid frame. The beam deflection is measured from the midpoint between the magnets, where the unstable equilibrium point is located. A periodic voltage is applied to the frame; for a small amount of time the beam oscillates above one magnet but as the forcing is increased there is a sudden point at which the system begins oscillating back and forth chaotically between the two magnets. The motion of the beam was represented by the Duffing equation:

$$\frac{d^2x}{dt^2} + \delta \frac{dx}{dt} - \beta x + \alpha x^3 = f \cos \omega t \quad (2.2)$$

where x is the beam position measured from the midpoint. The system equation of motion includes negative linear and positive cubic stiffness terms that for a range of periodic forcing that yields chaotic oscillation.

A very recent study by Virgin et al. [6] demonstrated chaotic vibration of a ball moving on a two dimensional potential surface as shown in Figure (2.8 (b)). This study included experimental validation of the simulated chaotic vibrations. They used a machined surface with four potential wells that is forced in a sinusoidal horizontal motion produced by a scotch-yoke mechanism. A digital camera recorded the position of the ball on the surface. For a combination range of excitation frequency and amplitude, the system showed irregular oscillations inside and between the wells. The projected chaotic oscillations obtained from the embedded time series are displayed in Figure 2.8 (a) which shows divergence of two chaotic trajectories starting close to each other. They verified the presence of chaos by having positive Lyapunov exponents and a non-integer fractal dimension between three and four.

The most commonly used metric of chaos is the Lyapunov exponent. It relies on the chaotic system's sensitivity to initial conditions. That is, in chaotic systems, two trajectories starting close to each other in phase space, will move exponentially away in a very short amount of time [30]. Let d_o be a measure of the initial distance between the two starting points, after a small time the distance is

$$d(t) = d_o e^{\lambda t} \tag{2.3}$$

where λ is the Lyapunov exponent. A measure of divergence is obtained by finding the average exponential growth at many points along a trajectory. The criterion for chaos is that the magnitude of one of the Lyapunov exponents is found to be positive. This method is applicable when the time series data is available from numerical simulation or experiment.

The information entropy I is another metric for chaos or to show how unpredictable a system is. For example if the system is completely predictable, then $I = 0$. The procedure to find this property is as follows. First the total number of points on the Poincaré map is counted. Second, the phase plane is divided to small cube cells of size ϵ . Then the number

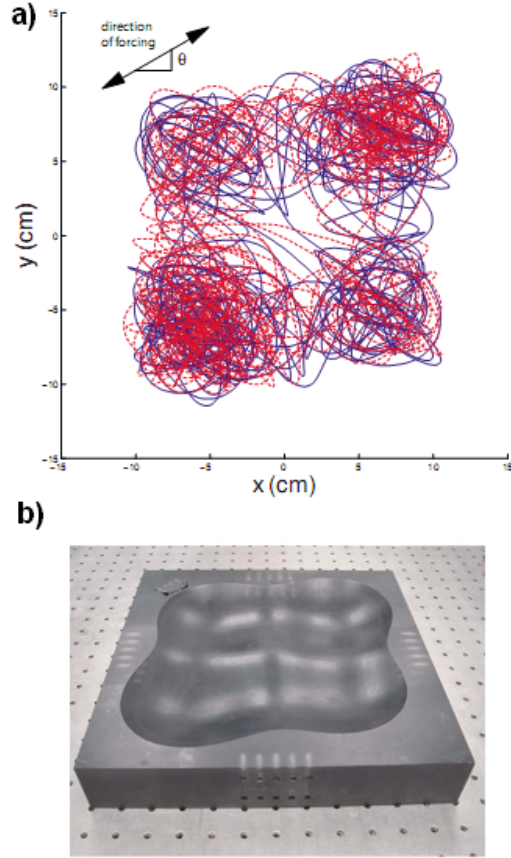


Figure 2.8: a) projected phase space trajectories for chaotic oscillation of a ball rolling on a surface b) experimental 2D potential surface [6].

of points inside each cube is counted and divided by the total number of points to get

$$P_i = \frac{N_i}{N_0}, \quad \sum^N P_i = 1 \quad (2.4)$$

Information entropy is obtained as

$$I(\epsilon) = - \sum^N P_i \log P_i \quad (2.5)$$

Information entropy can be a metric for the changes in chaotic system parameters when it does not depend on the initial conditions of the system, but instead it depends on system parameters like mass and stiffness, changes of which properties are then detected by measuring the change in the information entropy.

2.3.2 Applications of chaos

Appearance of chaos is not usually desired and there are numerous control systems designed to avoid it. On the other hand, there are reports on the constructive use of chaos in macro-systems for structural health monitoring of aeroelastic systems [7,33,34], fault detection in roller bearings [35], and detection of corrosion [19]. Circuit chaotic oscillations have also been used for secured communication [36].

Detection of stiffness changes in aeroelastic systems using chaotic oscillation has been performed by Epureanu et al. [7] who studied the oscillations of a panel forced by buffeting aerodynamic loads. They used the sensitivity of the chaotic response of the panel to detect variations in the stiffness of the mounting point of the upstream end of the panel. They found that the sensitivity of nonlinear and chaotic vibrations to these variations was 4-5 orders of magnitude higher than the sensitivity of the linear response. They could detect changes as small as 15% of the upstream stiffness. The attractor size and relative distribution of points in the Poincaré sections revealed very small changes in the system parameters. In other words, the attractor shape was deformed significantly by small changes in the target parameter, while the stable limit cycles showed insignificant changes in response to similar sized parameter changes. Figure 2.9 shows how the attractor shape and point distribution changed for a small variation in the stiffness of the upstream spring.

Diagnosis of roller bearing damage was carried out using chaos by Ghafari [35]. He utilized three measures of the chaotic attractor, the Lyapunov exponent, the correlation dimension, and information entropy, to measure changes in the state of the attractor and diagnosis the bearing health condition. The faults detected were as small as a localized wear area of 1.6 mm^2 in the inner race or a $0.8 \times 0.8 \text{ mm}$ indentation in the balls of a bearing with an outer diameter of 8 mm.

Chaos has also been used to detect mass variation in a piezoelectric cantilever beam by Yin et al. [19]. The beam was an aluminum plate with dimensions of $280 \times 15 \times 1.27 \text{ mm}$ with two lead zirconate titanate (PZT) patches bonded on both sides at the root of the beam. Nonlinear feedback control was used to turn the beam into a van der Pol oscillator. They drove the oscillator to chaos and reconstructed the state space of the chaotic attractor from time series of the velocity, acceleration, and jerk of a point at the tip of the beam. Calculating the sensitivity vector (SV) proposed in [37], they found the local deformation of the chaotic attractor in state space due to mass variation. In addition, they use the

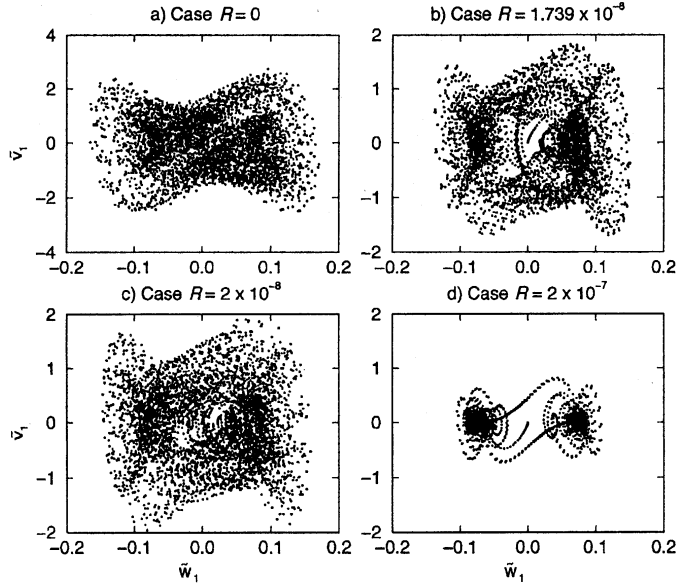


Figure 2.9: Poincaré maps for the displacement of a point on a buffeting panel for four perturbations of the stiffness of upstream spring [7].

method of the probability density function (PDF) to find the ratio of the number of points in a small circle to the total number of points in a sampled attractor in the velocity and acceleration phase-plane before and after adding a mass to the beam. The SV and PDF methods were able to detect 10 mg of mass added at the middle and tip of the beam with maximum error of 0.5 mg for the SV method and 1 mg for the PDF method representing a mass resolution of 0.07% of the total beam mass, which is a finer resolution compared to linear detection methods, such as frequency shift.

Despite the few reported studies on the usefulness of chaos in macro-scale applications, there is no evidence of applying chaos for detection in micro-scale systems. The main reason for this deficiency is the lack of resources on the nonlinear dynamic behaviour of MEMS. Most researchers avoid nonlinear systems due to their complexity. Only in the last decade, have researchers paid attention to the study of nonlinear dynamics in MEMS and NEMS since the main elements of these systems, including cantilever beams and doubly clamped beams, show significant nonlinear responses that cannot be neglected and need thorough study [38]. Such attention is now growing due to the fast growing area of NEMS showing strong chaotic responses that can be effectively used towards developing nonlinear

sensors with improved resolution.

2.3.3 Nonlinear Dynamics in MEMS

For micro-structures in electrostatic fields there are a number of nonlinearities including electrostatic forcing, large deflections, and squeeze film damping [39]. We will focus our review on nonlinear effects appearing in MEMS devices because of electrostatic loading.

Pull-in Instability in MEMS

Parallel-plate electrostatic actuators with a movable electrode are subject to elastic and electrostatic forces. Once the movable plate is perturbed away from its equilibrium position, it either tends to return to the equilibrium position (stable equilibrium) or to move further away (unstable equilibrium). The stable equilibrium position is at its maximum at a specific voltage called the pull-in voltage. Above this voltage instability occurs because the balance between elastic and electrical forces is lost.

A number of researchers have used the Finite Element Method (FEM) to find the pull-in point [40,41]. Gilbert et al. [40] developed a solver that predicts the pull-in voltage. The solver is able to solve static coupled electro-mechanical systems by coupling a mechanical FE solver to an electrostatic Boundary Element (BE) solver.

Other researchers are using analytical and numerical methods to find the threshold of instability. For instance, Zavracky et al. [42] fabricated a cantilever micro-switch and found the switch pull-in voltage. They used a lumped-mass model to represent the switch, equated the electrostatic force to the spring force, and solved the resulting algebraic equation numerically to find the beam deflection. They also solved a boundary value problem representing the static deflection of the beam and accounting for the variation of the electrostatic force along the beam length for the beam deflection. They concluded that the lumped model underestimates pull-in deflection at one third of the gap, whereas the BVP predicts a more realistic deflection at two fifths of the gap.

Luo et al. [43] and Liu et al. [1] used lumped-mass models to predict the pull-in point. On the other hand, Zhang et al. [44] obtained the pull-in deflection for micro-beams with various boundary conditions using a continuous beam model. They assumed that the first

mode shape is the dominant deflection shape and used that mode only to discretize the beam equation.

A more comprehensive analytical method was presented by Younis et al. [45], who investigated the static and dynamic pull-in instability of micro-beams. They used the mode shapes of the beam as the basis function in a Galerkin discretization procedure to obtain the governing ordinary differential equations of the system. They found that using five mode shapes is adequate for prediction of the static behaviour of the micro-beam. The resulting reduced-order model was found to be a fast and accurate simulation method. This method is used to study pull-in behaviour in this thesis for a micro-cantilever beam in an electrostatic field.

Bi-stability and Chaos in MEMS

Bi-stable systems have two stable equilibrium positions. Bi-stability is of interest in electrostatic MEMS because it means having two stable operating points, an extended stable displacement range, and two adjustable capacitance ranges during snap-through and release events. These properties are used to improve the performance of switches and other actuators, variable capacitors, and sensors.

Bi-stability, the presence of two stable equilibria, accompanying an unstable equilibrium is also a common mechanism underlying chaotic motions (Figure 2.6). In smaller scale NEMS, there are recent studies on nonlinear vibration, chaos and their applications [46–48]. Bucks et al. [46] found higher mass detection sensitivity is achieved once a nanomechanical resonator is operated in the nonlinear region. Conley et al. [47] studied the onset of nonlinear planar motion and nonplanar whirling motion of electrostatically excited nanowires with a proposed application in an overload detection mechanism. The study is further developed by Chen et al. [48], in which they presented a bifurcation diagram for the extensive nonplanar chaotic oscillation of a nanowire at increased AC voltages. Chen et al. [48] suggested applying the chaotic nanowire oscillators in random number generation used in secure communications.

In micro-scale, nonlinear responses, bi-stability and chaos have been reported by researchers in atomic force microscopy (AFM) [49–54] applied in surface imaging applications, and electrostatic MEMS [1, 55–64]. An AFM probe consists of a micro-cantilever beam with the tip at its end in close proximity to the surface of a specimen. Bi-stability

has been reported in static response and hysteretic jumps in the frequency response of AFM when the distance of the tip and sample was less than 10nm [52]. The potential energy in the bi-stable region was an asymmetric two-well potential. They also found that the frequency response at large amplitudes contained multiple harmonics due to period doubling.

Bi-stability in MEMS was also investigated for a buckled microbeam [65, 66] and a curved microbeam [61]. Saif [65] studied bi-stability based on buckling of a clamped-clamped microbeam under a tunable compressive force applied by an actuator. Once the compressive force exceeds a critical value, the beam buckles to one of two possible buckling states. The beam is also subjected to a transverse force. At a given compressive force, there is a threshold value of the transverse force at which the system switches from one state to the other. They found a closed form relation between the transverse force and the transverse beam displacement. Furthermore, it was found that the potential energy of the system is modified by adjusting the transverse force making one potential well shallower than the other, thus reducing the energy barrier between the two-wells.

In an extension of the work, Sulfridge et al. [66] generated the threshold transverse load by electrostatic comb drive actuators. They modelled the system using the equation of motion of the buckled beam that contained inertial and geometric nonlinearities. They simulated the midpoint displacement of the beam and found good agreement for threshold force and switching times between the two states in simulation and experiments.

Bi-stability in MEMS was analyzed for electrostatic actuators [59–62] with geometrical nonlinearities paying more attention to static response than dynamic responses. Zhang et al. [59] investigated the static response of an arch-shaped beam that showed either snap-through and pull-in, or only pull-in, under electrostatic loading. The snap-through response led to bi-stability with a large amplitude response. Krylov et al. [61] extended the study of the static response of arch-shaped beams that show bi-stable behavior. The idea is based on the snap-through buckling behavior of a von Mises truss loaded by a force at the centre. Through modelling of the curved electrostatic beam, pull-in behaviour is simulated showing two branches of stable and unstable solutions. They observed two pull-in instabilities, one at a small displacement due to geometrical nonlinearity and the other at a larger displacement due to electrostatic forcing. Pull-in and snap-through voltages of bi-stable arched beams were also derived by Das et al. [62] using a model including the material and geometrical nonlinearities in finite element and boundary element methods. They

simulated the dynamic pull-in and snap-through response without considering damping forces.

There are a few studies on the nonlinear response of electrostatic MEMS [63,64]. Rhoads et al. [63] studied the softening, hardening and mixed behaviour for a fixed-fixed electrostatic microbeam. They assumed damping and electrostatic forces are small and used perturbation methods to find the frequency response of the beam at small amplitudes away from dynamic pull-in. They specified AC, and DC voltage ranges for stable and unstable vibrations of the undamped beam. Zhang et al. [64] studied softening in electrostatic micro-cantilever beam using a lumped model that had both electrostatic force and squeeze film damping. They reported period doubling bifurcations in their simulations.

Dynamic instabilities in MEMS electrostatic actuators due to pull-in and snap-through were also reported [59–62]. Krylov [60] studied the instability of the actuators for voltages above dynamic pull-in using a reduced order model including squeeze film damping. Applying a DC step input, he found that the Lyapunov exponent of the dynamic response is positive for voltages above dynamic pull-in indicating unstable vibrations. The squeeze film damping was also found to be significant for electrodes vibrating close to the substrate.

Chaotic vibrations have been observed in bi-stable non-interdigitated comb drive electrostatic actuators. Wang et al. [56] modelled them using a mass-spring system as a Duffing oscillator with a two-well potential field. Through simulations and experiments they have shown chaotic oscillations in the two-well region of the system. As an extension to this work, De and Aluru [57] presented a model for the system including the electrostatic forcing, nonlinear stiffness, and squeeze film damping. They showed that even in the absence of the nonlinear mechanical and fluidic forces, the system had chaotic motion. Thus, the electrostatic forces were found to be the primary mechanism producing chaos. The boundaries for chaotic motion in the amplitude-frequency space of the applied voltage were found both from experiments and from Melnikov’s method by DeMartini et al. [58]. It was found that Melnikov’s criteria underestimated the AC drive voltage threshold for chaos due to the fact that it predicted transient or attracting chaos and the experiments were showing only the boundary of attracting chaos.

Chaotic oscillations were also found in the motions of an AFM probe in tapping-mode [49–51], where the probe is driven around its natural frequency to tap the sample surface. Ashhab et al. [50] modelled the beam-tip-sample interaction accounting for the

damping and forcing as perturbations to the system Hamiltonian. They found a homoclinic orbit and used the Melnikov's method to find how that orbit breaks up in the presence of perturbations to the Hamiltonian. The orbit breaks up once the stable and unstable manifolds of the orbit intersects non-transversely indicating chaos. By numerical simulation, they found a surface in the space of physical parameters, below which chaotic oscillations happen. With the aid of that diagram, they designed a position and velocity feedback controller to avoid chaotic oscillations.

Chaos in AFM was also reported in some purely experimental studies [53, 54]. They observed and characterized chaos under a variety of operating conditions. They reported “weak” chaos, containing strong periodic oscillation. Raman and Hu [53] reported chaos upon transition from a non-contact regime to a tapping regime. The existence of chaos was confirmed by evaluating the largest Lyapunov exponent of the time series of oscillations. Jamitzky et al. [54] confirmed the presence of chaos by computing the correlation dimension of the time series of the response. Their bifurcation diagram included multiple period regions as well as a chaotic region.

Chaos in electrostatic MEMS was first investigated by Bienstman et al. [55] for doubly clamped beams. They developed an autonomous impact resonator by taking advantage of the pull-in instability in an electrostatic microbeam resonator without a separate control circuit. The microbeam acts as an electrode in a capacitor that is driven at a voltage larger than the pull-in voltage, forcing it to collapse. Thereby, a short circuit occurs that results in capacitor discharge and beam pull-off. Once the beam is oscillating freely in air, charge builds up gradually causing pull-in and the impact happens again. Through simulations they observed chaotic behavior in the system response. They also reported experimental evidence of period doubling. Further nonlinear dynamic studies of doubly clamped electrostatic beams were conducted by Park et al. [38] who converted the chaotic oscillation to large detectable periodic motions using force control.

Chaos has also been studied in a closed loop feedback control system of an electrostatic actuator with capacitive sensing [1]. The feedback control was originally designed by Lu and Fedder [9] for position tracking of probe-based magnetic disk drives using position feedback by a capacitive sensor. They added a constant controller gain that ensures a minimum phase margin of 60° to a linearized model of the actuator. They were able to stabilize the system up to 60% of the gap experimentally. Further studies of the controller [1] kept all the nonlinearities in the model and found a region of bi-stability and chaos

even at low excitation amplitudes. Their goal was to find excitation voltage ranges to avoid bi-stability and nonlinear dynamics.

In this thesis, the control law introduced by Liu [1] is used to create large-stroke electrostatic actuators. These actuators are of interest not only for applications requiring large range of motions but also as platforms to realize chaotic micro-resonators. The controller parameters are designed both for a stable and a bi-stable chaotic system with a wide operating voltage range. A new controller is finally proposed to produce chaos that consumes less voltage and produces less noise.

Chapter 3

System Model

Mathematical models for the electrostatic micro-actuator are developed in this chapter including the open loop and the closed loop system. The closed loop model is investigated for the two purposes of extended-stability actuator and the chaotic micro-resonator. The models are analyzed comprehensively to predict the system responses to a wide range of excitations [67].

3.1 Open-Loop Actuator

The equation of motion of the cantilever beam in an electrostatic field (Figure 3.1) is obtained in this section. A free body diagram for an infinitesimal element of length $d\hat{x}$ along the beam is shown in Figure 3.2. The equation of motion of the element in the vertical direction \hat{z} can be written using Newton's second law. The inertia force acting on the beam element is

$$\rho A(\hat{x}) \frac{\partial^2 \hat{w}(\hat{x}, \hat{t})}{\partial \hat{t}^2} d\hat{x} \quad (3.1)$$

where ρ is the mass density, $A(\hat{x})$ is the cross sectional area of the beam, $\hat{w}(\hat{x}, \hat{t})$ is the deflection of the beam in the \hat{z} direction. Assuming a constant cross section for the element and writing Newton's Second Law for the vertical forces acting on the element, yields

$$\rho A \frac{\partial^2 \hat{w}(\hat{x}, \hat{t})}{\partial \hat{t}^2} d\hat{x} = V - (V + dV) + f(\hat{x}, \hat{t}) d\hat{x}. \quad (3.2)$$

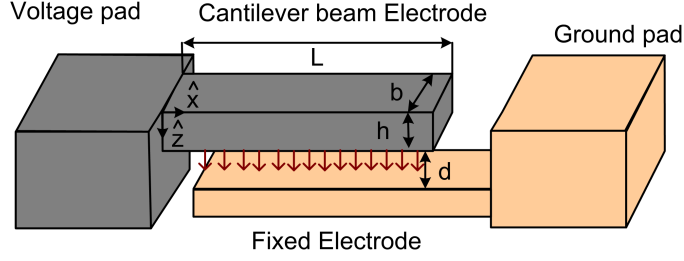


Figure 3.1: Schematic of micro-beam oscillator.

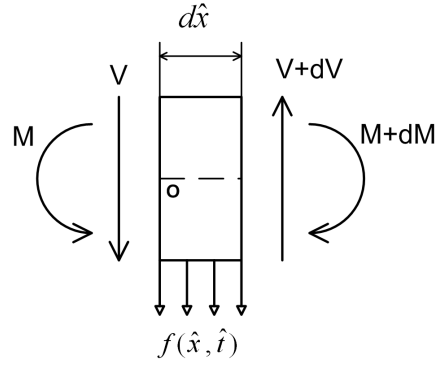


Figure 3.2: FBD for a small element along the beam.

where $f(\hat{x}, \hat{t})$ is a vertical distributed force per unit length acting on a beam element, V is the shear force and dV is variation of the shear force along the element. Writing the moment balance of the element about point o yields the following equation as the moment of inertia of the element is considered negligible:

$$-f(\hat{x}, \hat{t})d\hat{x}\frac{d\hat{x}}{2} + (V + dV)d\hat{x} + M - (M + dM) = 0 \quad (3.3)$$

where M is the moment at the left end of the element and dM is the change in the moment along the element length. Using the equations

$$dV = \frac{\partial V}{\partial \hat{x}}d\hat{x}, \quad dM = \frac{\partial M}{\partial \hat{x}}d\hat{x}, \quad (3.4)$$

and dividing Eq. (3.2) by dx , one obtains

$$\rho A \frac{\partial^2 \hat{w}(\hat{x}, \hat{t})}{\partial \hat{t}^2} = -\frac{\partial V}{\partial \hat{x}} + f(\hat{x}, \hat{t}). \quad (3.5)$$

Dropping higher-order terms in Eq. 3.3, one gets

$$V = \frac{dM}{d\hat{x}} \quad (3.6)$$

Using Eq. (3.6), Eq. (3.5) is written as

$$\rho A \frac{\partial^2 \hat{w}(\hat{x}, \hat{t})}{\partial \hat{t}^2} = -\frac{\partial^2 M}{\partial \hat{x}^2} + f(\hat{x}, \hat{t}) \quad (3.7)$$

On the other hand, from mechanics of material:

$$M(\hat{x}, \hat{t}) = EI \frac{\partial^2 \hat{w}(\hat{x}, \hat{t})}{\partial \hat{x}^2} \quad (3.8)$$

where EI is the flexural rigidity of the beam and is assumed constant. Substituting Eq. (3.8) in Eq. (3.7) results in

$$\rho A \frac{\partial^2 \hat{w}(\hat{x}, \hat{t})}{\partial \hat{t}^2} + EI \frac{\partial^4 \hat{w}(\hat{x}, \hat{t})}{\partial \hat{x}^4} = f(\hat{x}, \hat{t}) \quad (3.9)$$

In the above formula, $f(\hat{x}, \hat{t})$ is the electrostatic force and is written as

$$f(\hat{x}, \hat{t}) = \frac{\varepsilon_0 b V^2}{2(d - \hat{w}(\hat{x}, \hat{t}))^2} \quad (3.10)$$

where ε_0 is permittivity of the free space, b is the beam width, V is the applied voltage and d is the initial gap between the two electrodes. Substituting Eq. (3.10) into Eq. (3.9) yields the equation of motion for a beam in an electrostatic field.

$$\rho A \frac{\partial^2 \hat{w}(\hat{x}, \hat{t})}{\partial \hat{t}^2} + EI \frac{\partial^4 \hat{w}(\hat{x}, \hat{t})}{\partial \hat{x}^4} = \frac{\varepsilon_0 b V^2}{2(d - \hat{w}(\hat{x}, \hat{t}))^2} \quad (3.11)$$

In the presence of damping, the equation becomes

$$\rho A \frac{\partial^2 \hat{w}(\hat{x}, \hat{t})}{\partial \hat{t}^2} + EI \frac{\partial^4 \hat{w}(\hat{x}, \hat{t})}{\partial \hat{x}^4} + c \frac{\partial \hat{w}(\hat{x}, \hat{t})}{\partial \hat{t}} = \frac{\varepsilon_0 b V^2}{2(d - \hat{w}(\hat{x}, \hat{t}))^2} \quad (3.12)$$

Where the viscous damping coefficient per unit length c is used to account for damping losses due to the beam motion through air. To reduce the notations, $\hat{w}(x, t)$ is only shown by \hat{w} . To regularize the singularity in the electrostatic force term, both sides of the equation is multiplied by $(d - \hat{w})^2$ [68], so that Eq. (3.12) becomes

$$\rho A \frac{\partial^2 \hat{w}}{\partial \hat{t}^2} (d - \hat{w})^2 + EI \frac{\partial^4 \hat{w}}{\partial \hat{x}^4} (d - \hat{w})^2 + c \frac{\partial \hat{w}}{\partial \hat{t}} (d - \hat{w})^2 = \frac{\varepsilon_0 b V^2}{2} \quad (3.13)$$

For improving the accuracy in the numerical solution of Eq. (3.13), the following non-dimensional parameters are used:

$$x = \frac{\hat{x}}{L}, \quad w = \frac{\hat{w}}{d}, \quad t = \frac{\hat{t}}{T} \quad (3.14)$$

where L is the beam length, and T is defined in Eq. (3.18). Substitution of the above parameters in Eq. (3.13) results in

$$\frac{\rho A d^3}{T^2} \frac{\partial^2 w}{\partial t^2} (1-w)^2 + \frac{E I d^3}{L^4} \frac{\partial^4 w}{\partial x^4} (1-w)^2 + \frac{c d^3}{T} \frac{\partial w}{\partial t} (1-w)^2 = \frac{\varepsilon_0 b V^2}{2} \quad (3.15)$$

Multiplying both sides of the equation by $\frac{L^4}{E I d^3}$, one gets

$$\frac{\rho A L^4}{E I T^2} \frac{\partial^2 w}{\partial t^2} (1-w)^2 + \frac{\partial^4 w}{\partial x^4} (1-w)^2 + \frac{c L^4}{E I T} \frac{\partial w}{\partial t} (1-w)^2 = \frac{\varepsilon_0 b V^2 L^4}{2 E I d^3} \quad (3.16)$$

Eq. (3.16) is then simplified as

$$\frac{\partial^2 w}{\partial t^2} (1-w)^2 + \frac{\partial^4 w}{\partial x^4} (1-w)^2 + \mu \frac{\partial w}{\partial t} (1-w)^2 = \alpha V^2 \quad (3.17)$$

using T as

$$T = \sqrt{\frac{\rho A L^4}{E I}}, \quad (3.18)$$

and introducing the parameters

$$\mu = \frac{c L^4}{E I T}, \quad (3.19)$$

and

$$\alpha = \frac{\varepsilon_0 b L^4}{2 E I d^3}. \quad (3.20)$$

Since the equation of motion involves a second-order derivative with respect to time and a fourth-order derivative with respect to x , two initial conditions and four boundary conditions are required to determine a unique solution for $w(x, t)$. A solution to Eq. (3.17) will be sought using Galerkin's method with an trial function of the form

$$w(x, t) = \Phi(x)q(t). \quad (3.21)$$

For obtaining the basis function $\Phi(x)$, Eq. (3.21) is substituted in the free vibration form of Eq. (3.17), which results in

$$\ddot{q}\Phi + \dot{q}\Phi\mu + \Phi^{(4)}q = 0 \quad (3.22)$$

where $\Phi^{(4)}$ is the fourth derivative with respect to x . Eq. (3.22) can then be simplified as

$$\frac{\Phi^{(4)}}{\Phi} = \frac{-\ddot{q} - \mu\dot{q}}{q} = \omega^2 \quad (3.23)$$

The equality between the first and third expressions yields

$$\Phi^{(4)} - \omega^2\Phi = 0 \quad (3.24)$$

For solving Eq. (3.24), a solution of the form

$$\Phi(x) = Ae^{sx} \quad (3.25)$$

is sought, where A and s are constants. The auxiliary equation is obtained as

$$s^4 - \omega^2 = 0 \quad (3.26)$$

The roots of this equation are

$$s_{1,2} = \pm\sqrt{\omega}, \quad s_{3,4} = \pm i\sqrt{\omega} \quad (3.27)$$

Therefore, $\Phi(x)$ can be written as

$$\Phi(x) = A_1e^{\sqrt{\omega}x} + A_2e^{-\sqrt{\omega}x} + A_3e^{i\sqrt{\omega}x} + A_4e^{-i\sqrt{\omega}x} \quad (3.28)$$

Eq. (3.28) can be expressed as

$$\Phi(x) = A_1 \cosh(\beta x) + A_2 \sinh(\beta x) + A_3 \cos(\beta x) + A_4 \sin(\beta x), \quad (3.29)$$

which is also called the characteristic function or the mode shape of the beam and

$$\beta^2 = \omega. \quad (3.30)$$

In Eq. (3.29), A_1 , A_2 , A_3 , A_4 , and β are constants that must be determined from the boundary conditions of a cantilever beam:

$$\begin{aligned} w|_{x=0} &= 0, \\ \frac{\partial w}{\partial x}|_{x=0} &= 0, \\ M|_{x=1} &= EI \frac{\partial^2 w}{\partial x^2}|_{x=1} = 0, \\ V|_{x=1} &= EI \frac{\partial^3 w}{\partial x^3}|_{x=1} = 0 \end{aligned} \quad (3.31)$$

where $x = 1$ corresponds to the beam tip. Since there are four boundary conditions and five unknowns, one of the constants of $A_1 \cdots A_4, \beta$ is chosen arbitrarily. Substituting Eq. (3.29) in the boundary conditions of Eq. (3.31), and setting the determinant of the resulting linear system in $A_1, A_2, A_3,$ and A_4 equal to zero leads to the frequency equation

$$1 + \cosh(\beta)\cos(\beta) = 0 \quad (3.32)$$

There are an infinite number of β that satisfy Eq. (3.32). They will be denoted as $\beta_n, n = 1, 2, \dots$, where n is the mode number. The corresponding cantilever beam mode shape Φ_n is

$$\Phi_n(x) = A_n \{ \sin(\beta_n x) - \sinh(\beta_n x) + \gamma_n [\cos(\beta_n x) - \cosh(\beta_n x)] \} \quad (3.33)$$

where

$$\gamma_n = -\frac{\sin(\beta_n) + \sinh(\beta_n)}{\cos(\beta_n) + \cosh(\beta_n)}. \quad (3.34)$$

To normalize the mode shapes with respect to the beam tip modal deflection ($\Phi_n(1) = 1$), A_n is chosen to be

$$A_n = \frac{1}{\sin(\beta_n) - \sinh(\beta_n) + \gamma_n [\cos(\beta_n) - \cosh(\beta_n)]}. \quad (3.35)$$

Therefore, the specific form of the trial function, Eq.(3.21), is

$$w(x, t) = \sum_{n=1}^M \Phi_n(x) q_n(t) \quad (3.36)$$

where M is the number of modes (degrees of freedom) considered in the expansion and q_n is the n^{th} generalized coordinate. Eq. (3.36) is used in Eq. (3.17) to get

$$\begin{aligned} & \sum_{n=1}^M \Phi_n(x) \ddot{q}_n(t) \left(1 - \sum_{n=1}^M \Phi_n(x) q_n(t)\right)^2 \\ & + \sum_{n=1}^M \Phi_n^{(4)}(x) q_n(t) \left(1 - \sum_{n=1}^M \Phi_n(x) q_n(t)\right)^2 \\ & + \mu \sum_{n=1}^M \Phi_n(x) \dot{q}_n(t) \left(1 - \sum_{n=1}^M \Phi_n(x) q_n(t)\right)^2 = \alpha V^2 \end{aligned} \quad (3.37)$$

where $\Phi_n^{(4)}(x)$ is the fourth derivative of Φ_n with respect to x . The Galerkin method is then used; multiplying both sides of Equation (3.37) by the normalized mode shapes $\Phi_i(x)$,

integrating from $x = 0$ to $x = 1$, and using the orthogonality condition:

$$\int_0^1 \Phi_i(x)\Phi_n(x)dx = \kappa_i\delta_{ij} \quad (3.38)$$

where δ_{ij} is the Kronecker delta. The result is a set of M ordinary second-order differential equations in terms of q_n where $i = 1 \dots M$. For a one-mode approximation, the equation is

$$(\ddot{q}_1 + \mu\dot{q}_1 + \omega_1^2q_1)(1 + c_1q_1 + c_2q_1^2) = c_3\alpha V^2 \quad (3.39)$$

where over-dot means derivative with respect to time, ω_1 is the first natural frequency of the beam, and c_1 , c_2 , and c_3 are found after applying Galerkin's method.

3.1.1 Static Analysis

In this section, the static equilibrium of the beam is studied. The equilibrium equation for the cantilever beam describes the balance between the electrostatic force and the elastic force. When the elastic force can not resist the electrostatic force, the bottom electrode pulls-in the top electrode (beam) and stability is lost, this is called the static pull-in point that can be obtained from the static response of the system. The equilibrium equation is obtained from the equation of motion, Eq. (3.37), by setting the time derivatives equal to zero

$$\sum_{n=1}^M \Phi_n^{(4)}(x)q_n(t) \left(1 - \sum_{n=1}^M \Phi_n(x)q_n(t) \right)^2 = \alpha V_{DC}^2 \quad (3.40)$$

Galerkin's method is then applied. The result is a set of cubic polynomial equations in q_n , the solution of which is obtained for an applied voltage V_{DC} . Having solved for each q_n , the beam tip deflection is then found from

$$w(1) = w(1, t) = \sum_{n=1}^M \Phi_n(1)q_n(t) = \sum_{n=1}^M q_n(t) \quad (3.41)$$

For a one-mode approximation, the beam tip deflection $w(1) = q_1$ and the equilibrium equation is

$$\omega_1^2q_1 + c_1q_1^2 + c_2q_1^3 = \alpha c_3V_{DC}^2 \quad (3.42)$$

where c_1 , c_2 , and c_3 are found after integration of the mode shapes and their products. The solution to the algebraic Eq. (3.42) is found numerically and shown in Figure 3.3 for

the actuator series I listed in Table 3.1. The actuator dimensions and gains listed in the table are used for all the simulations in this chapter unless otherwise mentioned. The figure also shows the beam tip deflection versus DC voltage curves obtained using two- to six-mode approximations. The point on the graph where the slope of deflection versus voltage becomes infinite $\frac{\partial w}{\partial V_{DC}} \rightarrow \infty$ is the pull-in point which corresponds to a saddle-node bifurcation. For any voltage value beyond this point, no equilibrium position is available and the beam will snap down to touch the bottom electrode. The pull-in deflection is found to be at 45 percent of the capacitor gap, which is higher than the 33 percent of the gap predicted by lumped-mass models [44].

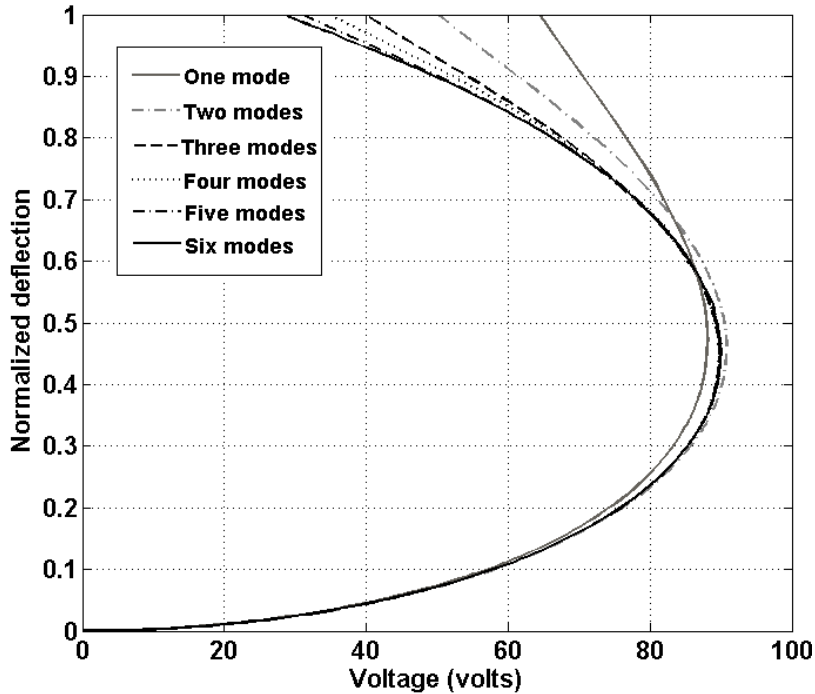


Figure 3.3: Nondimensional deflection of the beam tip versus DC voltage V_{DC} .

The local stability of the two branches of equilibrium points below and above the pull-in point is examined by finding the eigenvalues of the Jacobian matrix evaluated at the equilibrium point. It is found that the real parts of the eigenvalues of points on the lower branch are always negative (stable), while one of the eigenvalues of points on the upper branch is always positive (unstable). At the pull-in point one of the eigenvalues is zero,

indicating a saddle-node bifurcation. For example, at $V_{DC} = 75$ V and using the one-mode model, the eigenvalues at the lower equilibrium point $w_1 = 0.2$ are $(-0.36 \pm 2.8i)$. At the upper equilibrium point $w_1 = 0.83$ the eigenvalues are (0.31) and (-4.44) . Therefore, the lower equilibrium is a stable equilibrium, while the upper equilibrium is an unstable equilibrium. Furthermore, the nondimensional natural frequency of the stable equilibrium point (the imaginary part of the eigenvalues) is smaller than that of the straight beam, 2.8 versus 3.5158, which indicates a decrease in linear stiffness due to the electrostatic force.

Table 3.1: Actuator series I parameters [1]

Parameter	Symbol	Value
Displacement Gain	Ψ	1.527 V
Voltage Gain	G	1
Density	ρ	2331 kg/m ³
Beam Length	L	200 μm
Beam Width	b	80 μm
Beam Thickness	h	4.5 μm
Initial Gap	d	3 μm
Non-dimensional Damping Coefficient	μ	0.73
Permittivity of Air	ε	8.85×10^{-12} F/m
Modulus of Elasticity	E	166 GPa
Controller Damping	r	100

The effect of the number of modes used in the Galerkin approximation (number of degrees of freedom) on convergence is shown in Figure 3.3. Using the first three mode shapes, asymptotic convergence is obtained over the full extent of the lower branch of equilibrium solutions; six modes, at least are required for the solution to converge on the upper branch.

3.2 Closed-loop Actuator

A feedback control system is added to the open loop electrostatic actuator for dual purposes of extending the stable electrostatic actuation range and developing a chaotic oscillator.

The control law employed here was originally developed by Lu and Feddar [9] for probe-based magnetic micro-disk drives. They used a capacitive sensor and a controller to extend the actuator travel range and linearized the nonlinear system model. Further study of the nonlinear system was conducted by Liu et al. [1] using a lumped mass model for the cantilever beam that showed chaotic oscillation in the presence of force disturbances. Here a beam model is used based on the first mode shape, and a comprehensive study is performed on the nonlinear system to investigate its design both for the extended stability actuation and chaotic oscillation. The controller is also implemented differently, namely the capacitive sensor and controller used in the feedback system by Lu and Feddar [9] are replaced by an optical sensor and an analog voltage regulator circuit as described in Chapter 4.

A schematic of the closed-loop system is shown in Figure 3.4. In this figure, V_{in} is the reference input voltage, and V_c is the controller output voltage, and G is a voltage gain. The voltage applied between the two electrodes is $G(V_{in} - V_c)$ that creates the electrostatic forcing on the cantilever beam and is proportional to $F_e \propto G^2 \frac{(V_{in} - V_c)^2}{(d - \hat{w})^2}$.

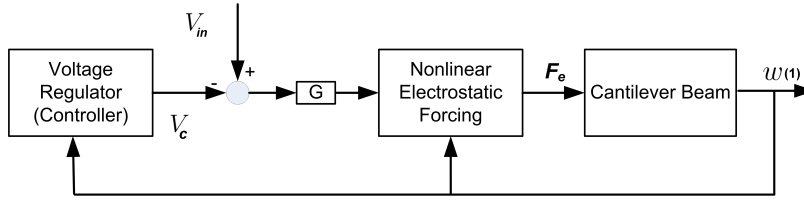


Figure 3.4: Closed loop system.

The equations for the closed-loop system are obtained by replacing V in Eq. (3.17) with the voltage difference between two electrodes. Therefore, the equation of motion becomes

$$\ddot{w}(1-w)^2 + w^{(4)}(1-w)^2 + \mu\dot{w}(1-w)^2 = G^2\alpha(V_{in} - V_c)^2 \quad (3.43)$$

The differential equation for the controller voltage (V_c) is [1]:

$$\dot{V}_c = -r\left(V_c - \frac{w(1)}{1-w(1)}\Psi\right) \quad (3.44)$$

where $w(1)$ is the beam tip deflection, Ψ and r are referred to as the displacement gain and controller damping, respectively. Eqs.(3.43) and (3.44) are treated similar to Eq. 3.37 using

Galerkin's method with the trial function from Eq. (3.36). For a one-mode approximation we get

$$\begin{cases} (\ddot{q}_1 + \mu\dot{q}_1 + \omega_1^2 q_1)(1 + c_1 q_1 + c_2 q_1^2) = c_3 G^2 \alpha (V_{in} - V_c)^2 \\ \dot{V}_c = -r(V_c - \frac{q_1}{1 - q_1} \Psi) \end{cases} \quad (3.45)$$

3.3 Static Response

To investigate the static response of the closed-loop system, equations Eqs. (3.43) and (3.44) are solved by setting the derivatives with respect to time equal to zero. Subsequently, from Eq. (3.44) V_c is then found to be

$$V_c = \frac{w(1)}{1 - w(1)} \Psi \quad (3.46)$$

Substituting Eq. (3.46) into Eq. (3.43) with zero derivatives yields

$$w^{(4)}(1 - w)^2 = G^2 \alpha (V_{in} - \frac{w(1)}{1 - w(1)} \Psi)^2 \quad (3.47)$$

Using Eqs. (3.36) and (3.41) into Eq. (3.47) and simplifying, results in

$$\begin{aligned} & \left(\sum_{n=1}^M \Phi_n^{(4)} q_n \right) \left(1 - \sum_{n=1}^M \Phi_n q_n \right)^2 \left(1 - \sum_{n=1}^M q_n \right)^2 \\ & = G^2 \alpha \left[V_{in} \left(1 - \sum_{n=1}^M q_n \right) - \Psi \sum_{n=1}^M q_n \right]^2 \end{aligned} \quad (3.48)$$

The expression of Φ_n (Eq. (3.33)) is substituted into the above equation; then it is multiplied by Φ_i for $i = 1 \cdots M$, and integrated over the entire normalized beam length. The result is a set of n quintic polynomial equations in terms of q_n for $n = 1 \cdots M$ and their products. For example, using a one-mode approximation, the quintic polynomial is

$$\omega_1^2 q_1 (1 + c_1 q_1 + c_2 q_1^2) = c_3 \alpha G^2 (V_{in} - \frac{q_1}{1 - q_1} \Psi)^2 \quad (3.49)$$

where c_1 , c_2 , and c_3 are found from Galerkin's method. This equation simplifies to

$$q_1^5 + a_4 q_1^4 + a_3 q_1^3 + f_2(V_{in}, G) q_1^2 + f_1(V_{in}, G) q_1 + f_0(V_{in}, G) = 0 \quad (3.50)$$

where $f_n(V_{in}, G)$ are

$$\begin{aligned}
f_2(V_{in}, G) &= b_0 + G^2 (b_1 V_{in} + b_2 V_{in}^2 + b_3) \\
f_1(V_{in}, G) &= d_0 + G^2 (d_1 V_{in} + d_2 V_{in}^2 + d_3) \\
f_0(V_{in}, G) &= e_0 G^2 V_{in}^2,
\end{aligned} \tag{3.51}$$

and all other constants are obtained from Galerkin's formulation. The parameters of the closed-loop system including Ψ and G in Eq. 3.49 can be configured so that the system exhibits bi-stable behavior. The bi-stable system has the potential to exhibit chaotic motions once excited above a threshold value.

3.3.1 Stable and Bi-stable Actuator

To create a chaotic system, controller parameters listed in Table 3.1 are used to realize a bi-stable response. The static beam displacement under DC voltage $V_{in} = V_{DC}$ is illustrated in Figure 3.5 when one to five modes are used in the Galerkin expansion. The curves are obtained by solving Equation 3.48 numerically. The profile has two turning points, which have infinite slopes representing saddle-node bifurcation points.

Once we increase the voltage, two fixed points appear at the left turning point and two fixed points disappear at the right turning point demonstrating saddle-node bifurcations. The stability of the fixed points is investigated in section 3.4. As can be deduced from Figure 3.5 and from the stability analysis of the fixed points, the unstable equilibrium points appear on the section of the curves between the two turning points (is the shaded region of the figure). The branches above and below the shaded region on the profiles are populated with stable equilibrium points. There is also a line of unstable equilibrium points close to unity.

Increasing the number of mode shapes used in the model widens the bi-stable voltage range moving the left bifurcation point to a lower voltage. In the bi-stability region, the upper stable equilibrium point is larger for models with a higher number of modes, meaning that for the same forcing, models with more modes deflect more (softening effect). Similarly, for a certain deflection amount e.g. 0.9, models with fewer modes need more voltage to reach that level of deflection. This effect shows the system is more flexible than would be indicated by using a single DOF model.

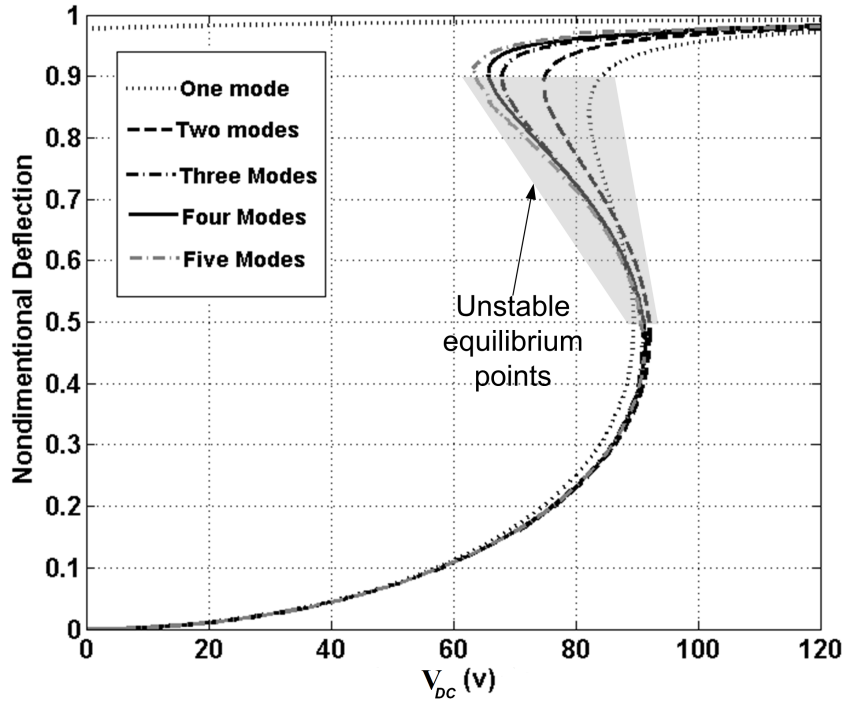


Figure 3.5: Nondimensional deflection of the beam tip versus voltage, V_{in} for the closed-loop system.

Convergence on the lower branch of solutions in Figure 3.5 is achieved using the first two mode shapes only. For the middle and upper branches, convergence is achieved using the first five modes except in the vicinity of the left turning point. Overall a three-mode model shows reasonable accuracy across the full voltage range.

Another way of presenting the roots of the equilibrium equation (3.50) is in the complex plane as depicted in Figure 3.6. The arrows show the direction of increasing voltage V_{in} . The arrows labeled 1 show the variation in the roots as the voltage increases from 0 V to 65 V (the left turning point), number 2 refers to the voltage increasing from 65 V to 90 V, and number 3 refers to voltages increasing from 90 V (the right turning point). From Figure 3.6 it can be deduced that by increasing the voltage in region 1, the two complex roots on the right side move leftward and approach the real axis, while one root moves on the real axis towards the right. As the voltage is increased in region 2, the two complex roots on the right side meet at the real axis and move in two different directions while the third root on left side continues moving to the right along the real axis. So in this region, three real

roots are available corresponding to three equilibrium positions. Subsequently, increasing the voltage in region 3 results in one real root continuing to move to the right along the real axis, while the other two roots approach each other, ultimately meet and bifurcate into the imaginary parts of the complex plane. Therefore, regions 1 and 3 are left with one real root.

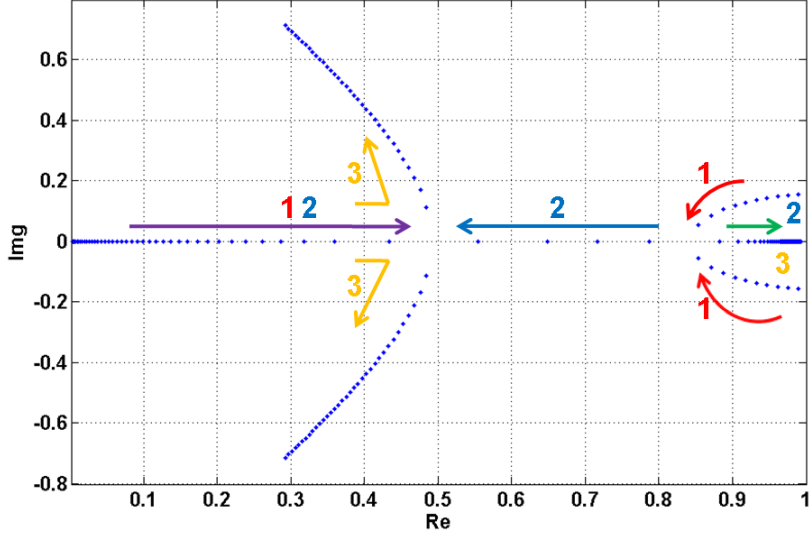


Figure 3.6: Roots of the equilibrium equation q_1 in complex plane.

The movements of the imaginary and real roots in the complex plane are functions of the controller gains and beam dimensions. Inspecting Eq. (3.49), we observe that the roots are function of the gains Ψ and G and the beam dimensions lumped in α given in Eq. (3.20). Changing the dimensions of the cantilever beam, alters α , but the product $G^2\alpha$ and, therefore the roots of Eq. (3.49) can be maintained constant. To demonstrate this observation, Figure 3.7 is plotted for a constant $G^2\alpha = 0.0002$, but for different voltage gains, G and different dimensions (Table 3.2). As can be seen, the roots are identical. Therefore, we can change the gain of the controller G to in order to maintain the same static response under variations in the beam dimensions.

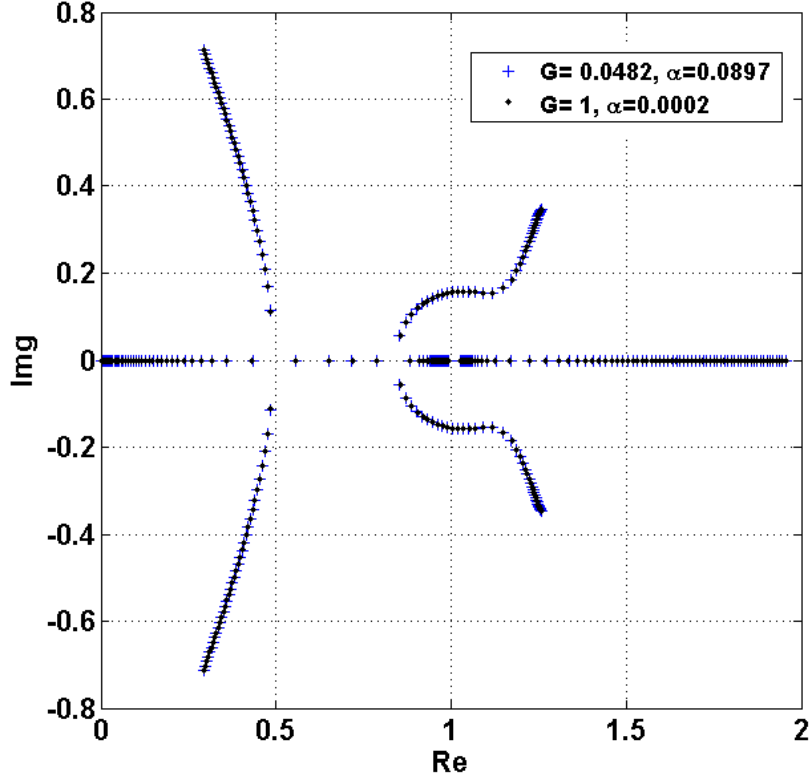


Figure 3.7: Roots of the one-mode equilibrium equation for a constant $G^2\alpha = 0.0002$.

Table 3.2: Beam dimensions corresponding to the α values used in Figure 3.7.

Beam #	α	Length, $L(\mu m)$	Width, $b(\mu m)$	Initial gap, $d(\mu m)$
I-A	0.0002	200	80	3
I-B	0.0897	496	10	3

The impact of changing the voltage gain G on the roots of Eq. (3.50) for the fixed dimensions is demonstrated in Figure 3.8. The results are shown for varying voltage between 0 and 150 V. In this figure and for small values of gain G , the loci of a complex conjugate pair of roots intersect the real axis on the right and another pair intersects the real axis to the left, thereby dividing the real axis left, middle, and right sections. The unstable equilibrium point exist in the middle section, whereas the first and second stable equilibrium points lie in the left and right regions, respectively. The intersections in fact correspond

to the two turning points in Figure 3.5. The complex roots do not co-exist, rather the right pair exists for low voltages and the left pair for high voltages only. For gains higher than 3.5, there is a single pair of complex roots and the loci of these roots do not intersect the real axis. For gains less than 3.5, the two complex branches intersect the real axis at two points resulting in two repeated real roots at each intersection, each corresponds to a different DC voltage. For a voltage gain of about 3.5, the two complex branches meet at a single point on the real axis. That means the voltage range for the unstable equilibrium point on the real axis disappears and the two loci of stable equilibrium points on the right and left sides of the real axis join together. This point is a cusp point in the parameter space of voltage V_{in} and gain G , where we get a triple repeated root. It is a codimension-2 bifurcation, where two control parameters V_{in} and G need to be tuned to achieve this bifurcation. To realize a bi-stable actuator, the controller gain has to be less than the threshold defined by the cusp point. Lowering the gain, for example from $G=3.5$ to $G=1$, leads to an increase in the distance between the two intersections that corresponds to an extended bi-stability voltage range.

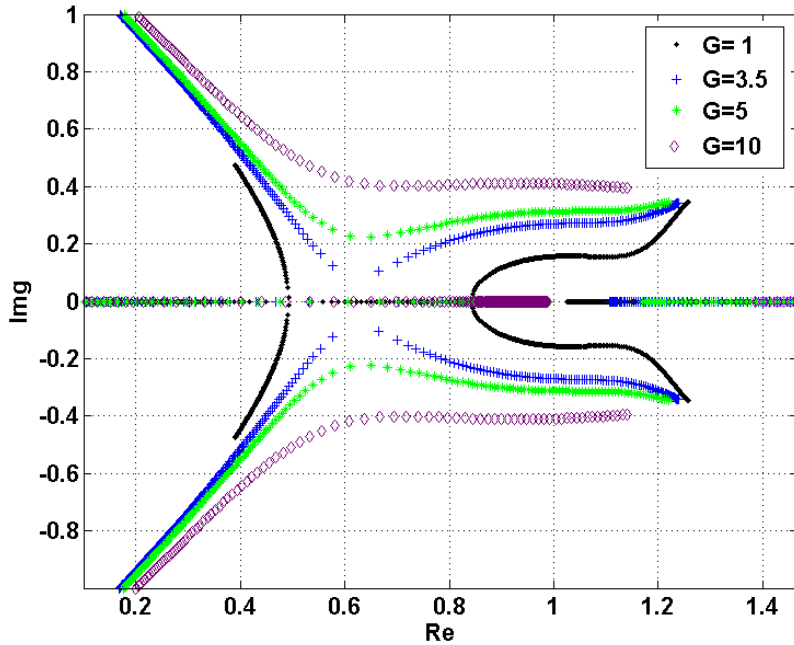


Figure 3.8: Roots of the one-mode equilibrium equation Eq. (3.50) in the complex plane for different voltage gains.

Static profiles to show the effect of gain G on the size of the bi-stability region are depicted in Figure 3.9 using one-mode model. As the voltage gain increases, the actuator requires less voltage to reach a certain point and similarly it travels larger for the same voltage. Below a critical gain value, the bi-stable region vanishes and the two turning points change to an inflection point (cusp point), where a triple repeated root of the polynomial appears. This bifurcation is shown in Figure 3.10. The lines show the location of the saddle node bifurcation points. The intersection of the two solid lines is the location of the cusp point, beyond which the system is stable. An electrostatic actuator with a stable equilibrium point for throughout the gap is a valuable finding that benefits electrostatic actuation applications restrained by pull-in instability.

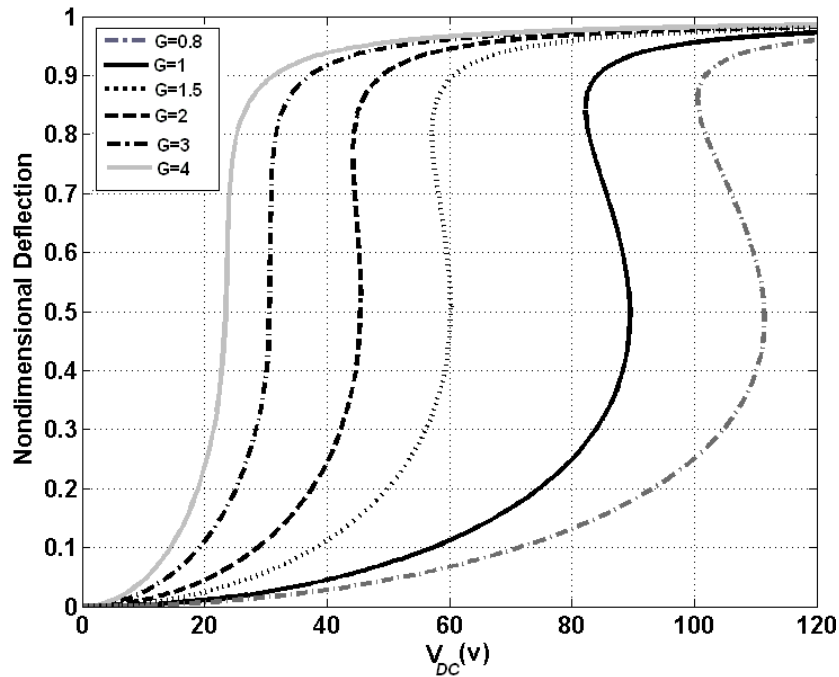


Figure 3.9: Effect of the voltage gain G on the static deflection versus DC voltage, V_{DC} curve.

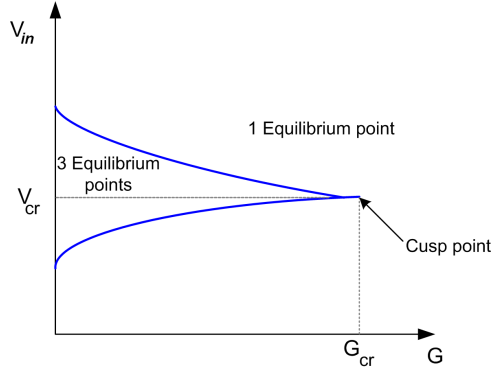


Figure 3.10: Stability diagram in the parameter space of voltage gain, G and voltage, V_{in} .

The size of bi-stability region is also dependent on the displacement gain Ψ that can be used to tune both the voltage and the displacement ranges where bi-stability occurs. Eq. (3.49) indicates that increasing displacement gain Ψ decreases the magnitude of electrostatic force, thus reducing the beam tip deflection and restoring spring force. In other words, it moves the upper equilibrium further away from the substrate, thereby making the actuator response more robust to external disturbances. This is demonstrated in Figure 3.11 using a one-mode model a voltage gain of $G = 0.8$. The rise of displacement gain also decreases the bi-stability range from 9 V for $\Psi = 1.527$ V to 4.5 V for $\Psi = 3$ V.

At a constant displacement gain Ψ , the bi-stability threshold, which classifies the system behavior to either stable or bi-stable can be identified by finding the triple repeated root of Eq. (3.50), that is by solving

$$F(q_1) = (q_1 - p_0)^3 (q_1^2 + p_1 q_1 + p_2) = 0 \quad (3.52)$$

where p_0 is the triple root, and p_1 , and p_2 are constant coefficients. The first and second derivatives with respect to q_1 also vanish at the triple root:

$$\left. \frac{dF}{dq_1} \right|_{q_1=p_0} = 0 \quad \text{and} \quad \left. \frac{d^2 F}{dq_1^2} \right|_{q_1=p_0} = 0. \quad (3.53)$$

Solving Eqs. (3.52) and (3.53) numerically results in the coordinates of the cusp point (V_{in}, G) and the triple real root p_0 . Using the actuator series I in Table 3.1, the threshold of bi-stability was found to be $G_{cr} = 3.471$, and $V_{cr} = 26.965V$ at a nondimensional

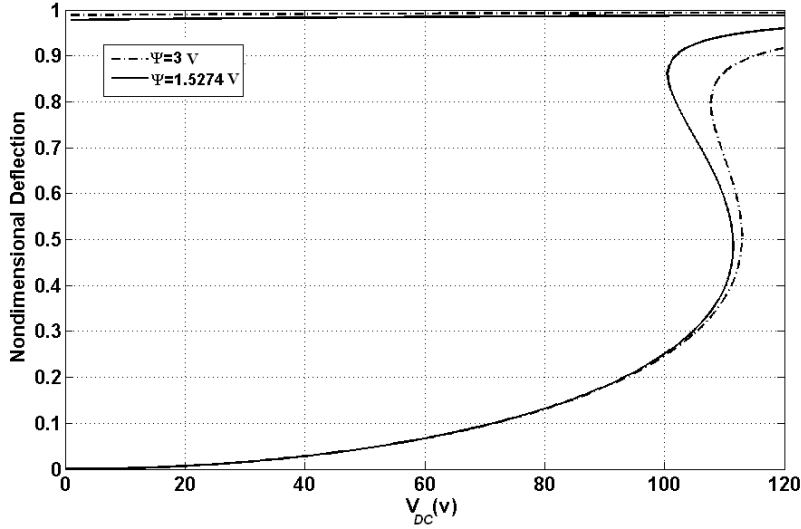


Figure 3.11: Effect of displacement gain, Ψ on static pull-in graph for $G = 0.8$.

deflection $q_{cr} = p_0 = 0.626$. Hence, choosing the gain value beyond G_{cr} at $\Psi = 1.527$ V makes the system stable over the entire gap.

3.4 Eigenvalue Problem

To analyze the closed-loop dynamics, first the state space equations are derived by discretizing Eqs. (3.43) and (3.44) using Galerkin's method. Although the results of the one-mode approximation are qualitatively, but not quantitatively valid, a one-mode model will be used throughout this section since the computational cost of integrating the quantitatively valid three-mode model are prohibitive. Using the first mode approximation, the resulting two differential equations would be in terms of q_1 , the normalized beam tip deflection. Letting $y_1 = q_1$, $y_2 = \dot{q}_1$, and $y_3 = V_c$, the state space equations become

$$\begin{cases} \dot{y}_1 = y_2 \\ \dot{y}_2 = -\mu y_2 - \omega_1^2 y_1 + \frac{c_3 \alpha G^2 (V_{in} - y_3)^2}{1 + c_1 y_1 + c_2 y_1^2} \\ \dot{y}_3 = -r \left(y_3 - \frac{y_1}{1 - y_1} \Psi \right) \end{cases} \quad (3.54)$$

For the dynamic analysis, the input voltage, V_{in} will include a DC and an AC component:

$$V_{in} = (V_{DC} + V_{AC} \cos(\omega t)). \quad (3.55)$$

where ω is the nondimensional circular frequency of excitation, and V_{AC} and V_{DC} are the AC and DC voltages, respectively.

To determine the stability of the fixed points, Eq. (3.54) is linearized about the fixed point. Eq. (3.46) is used in Eq. (3.54) to reduce the third order system to a second order system. The eigenvalues of the Jacobian of the system are then found for a given voltage and static deflection. The signs of the imaginary and real parts of the eigenvalues indicate the stability of the fixed point.

For the bi-stable actuator, the controller gains are set to $G = 0.8$ and $\Psi = 3$ V to obtain a bi-stability voltage range of 4.5 V and an upper stable equilibrium less than %90 of the gap as shown in Figure 3.11. Henceforth, we will adopt these values for the controller gains in conjunction with the actuator parameters in Table 3.1 for all further analysis on the bi-stable actuator up to section 3.6. Using the method described above, the eigenvalues are found in the bi-stable system at the bi-stability region. Table 3.3 shows the eigenvalues for the fixed points at input voltage, $V_{in} = 110$ V (Figure 3.11). Only four roots of Eq. (3.50) are listed in Table 3.3 since the fifth root is non-physical with a value greater than one. The first and third fixed points are stable foci, whereas the second and fourth fixed points are saddles.

Table 3.3: Eigenvalues for the fixed points at $V_{in} = 110$ V in Figure 3.11.

q_1	Eigenvalue 1	Eigenvalue 2
0.37	-0.37 - 1.98i	-0.37 + 1.98i
0.68	1.60	-2.33
0.864	-0.37 - 4.45i	-0.37 + 4.45i
0.985	61.17	-61.90

The eigenvalues of the stable foci also reveal the magnitude of the natural frequency. In Table 3.3, the nondimensional frequencies of oscillation around the first and third fixed points are 1.98 and 4.45 respectively. Since the canonical frequency for the undeflected

cantilever beam is 3.5158 (corresponding to 153.3 kHz), decreasing the frequency at the lower stable equilibrium indicates the dominance of the linear softening effect of the electrostatic forces and increasing the frequency at the upper stable equilibrium point reveals the dominance of the linear hardening effect of the controller. Figure 3.12 shows the nondimensional frequency obtained for the lower and upper stable equilibrium points using a one-mode approximation. It is interesting to note that in the bi-stability region [108 V-112.5 V], the system has a distinct fundamental natural frequency for each equilibrium point shown with black lines. In this graph, double and triple the natural frequency of the lower equilibrium are also shown with blue and magenta lines respectively; their intersections with the dashed black line reveal the possibility of dynamic interactions between the two equilibrium points. That is, once we excite the upper equilibrium at its natural frequency at those intersections, it can excite the lower one.

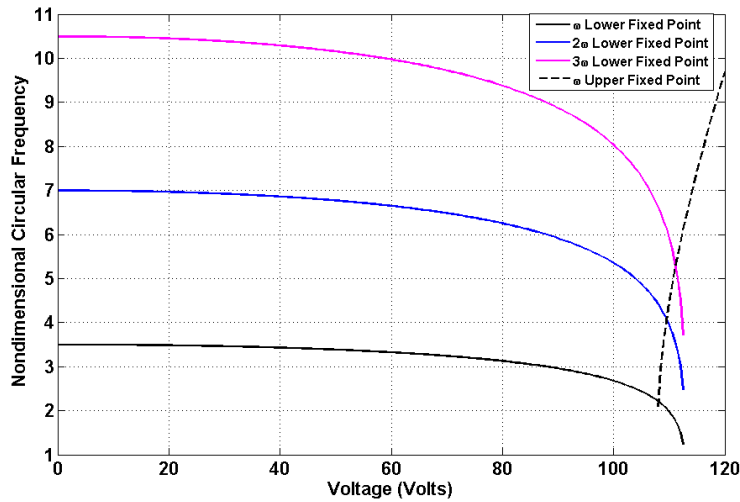


Figure 3.12: Nondimensional frequency versus input voltage V_{DC} .

3.5 Dynamic Response

3.5.1 Stable Actuator

For the stable actuator with the static profile for a voltage gain of $G = 4$ in Figure 3.9, the eigenvalues are obtained to find out the stable region on the profile as described in Section

3.4. Eigenvalues found at different static DC voltage had negative real parts showing the existence of a unique stable equilibrium over 95% of the gap, for example at $V_{DC} = 26.2$ eigenvalues are $-0.36 \pm 6.44i$. However, examining the transient dynamic response of the single stable system to initial conditions reveal stable actuation up to 83% of the gap. Figure 3.13 depicts the phase portrait and the time history of the beam free displacement response both converging to the ultimate dynamically stable equilibrium at 0.8309 of the gap at the maximum $V_{DC} = 26.2$. The results were obtained from numerically integrating of Eq. (3.54) with zero AC voltage. Increasing the DC voltage makes the top electrode pull-in to the bottom electrode and the system loses its stability. However, experimental results were more promising achieving 90% actuation as explained in section 4.2.2 that surpassed the largest actuation reported of 60% [9]. A more detailed study of the single stable system is conducted in section 4.2.2, which compares the experimental and the simulated results of the stable system.

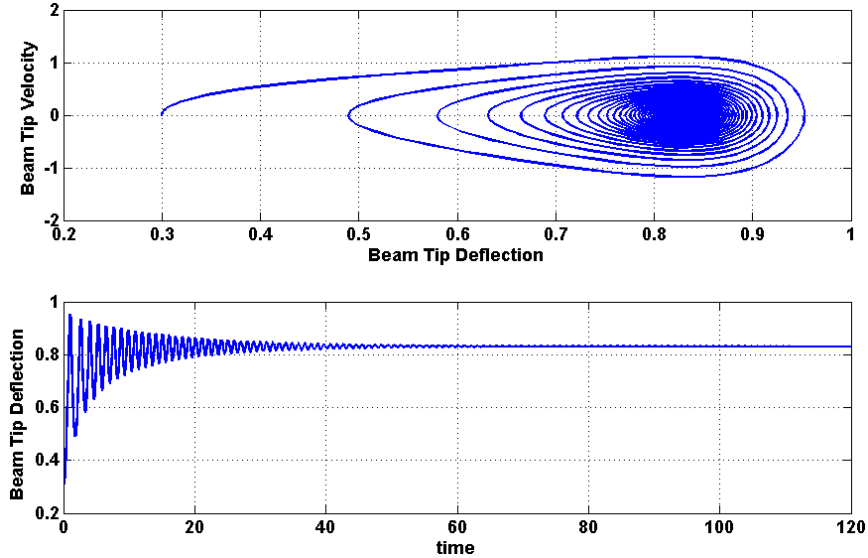


Figure 3.13: The nondimensional phase portrait and beam deflection, V_s for the system with gain of $G = 4$ in Figure 3.9, and excitations of $V_{AC} = 0$ V, $V_{DC} = 26.2$ V.

3.5.2 Bi-stable Actuator

The dynamic response of the bi-stable system is studied by numerically integrating Eq. (3.54). We set the DC voltage to $V_{DC} = 110$ V for all results of the bi-stable actuator unless

otherwise noted. Figures 3.14 and 3.15 show the dynamic response of the system, starting from an initial condition in the vicinity of the upper equilibrium point for $V_{AC} = 0.7$ V and $V_{AC} = 0.9$ V respectively at the excitation frequency of 153.3 kHz. The stable equilibria are marked with circles and the intermediate saddle is shown with a cross. The controller output voltage does not exceed 35 V in the two cases. Since the initial conditions are far from the steady-state orbit, the motions in Figure 3.14 undergoes significant transients before it settles to a limit cycle around the upper equilibrium point in the upper potential well. Figure 3.15 depicts escape from the upper to the lower potential well actuation between the two stable equilibrium points and large motions spanning the range between 27% and 92% of the gap. As the AC voltage is increased from 0.7 V to 0.9 V, the orbit becomes too large for the upper well, touches the stable manifold of the saddle and escapes to the lower well where it settles to a small limit cycle around the lower equilibrium point. The size of the lower well orbit at $V_{AC} = 0.9$ V is smaller than the size of the upper well orbit at $V_{AC} = 0.7$ V, 0.02 versus 0.05, which indicates that the lower potential well is deeper than the upper well. Larger oscillation in the lower well can be found for systems with less damping.

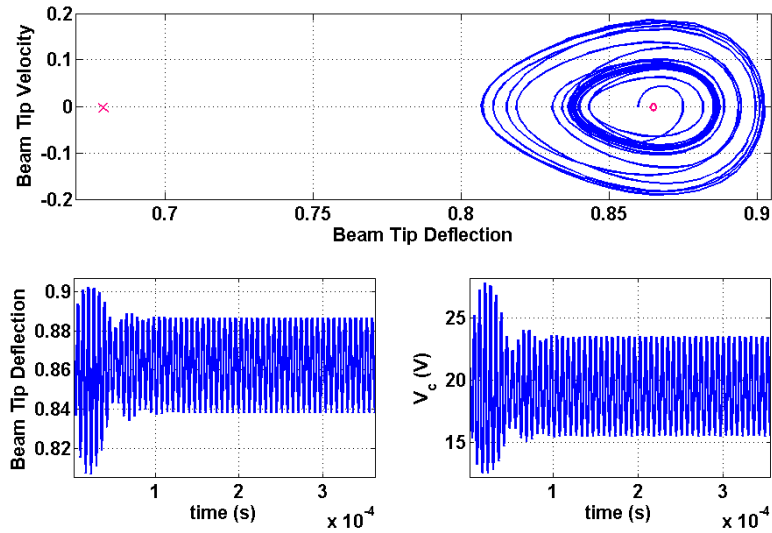


Figure 3.14: The phase portrait, beam tip deflection w_1 and controller output voltage, V_c for $\mu = 0.7$, $\omega = 3.5158$, $V_{AC} = 0.7$ V, and the initial conditions ($q_1 = 0.86$, $\dot{q}_1 = 0$, $V_c = 18.43$ V).

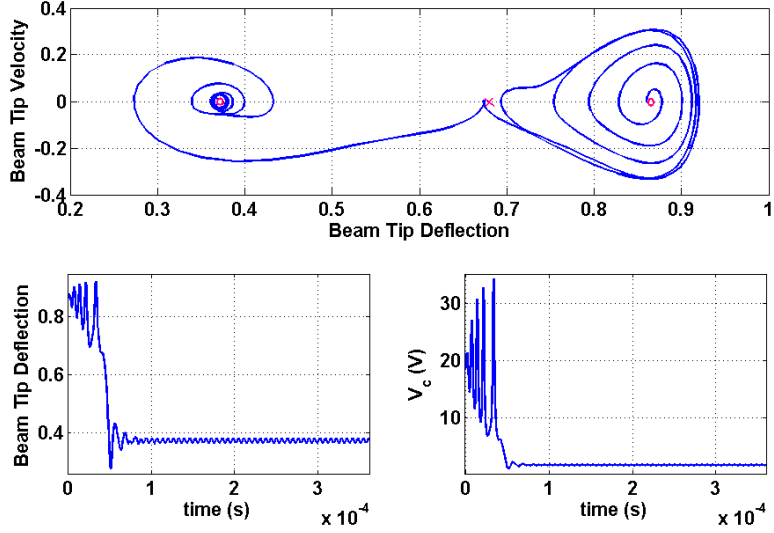


Figure 3.15: The phase portrait, beam tip deflection w_1 and controller output voltage, V_c for $\mu = 0.7$, $\omega = 3.5158$, $V_{AC} = 0.9$ V, and the initial conditions ($q_1 = 0.86$, $\dot{q}_1 = 0$, $V_c = 18.43$ V).

By reducing damping in the system, the basins of attraction for the two potential wells can be illustrated as in Figure 3.16 for an actuator with a reduced damping from 0.7 to 0.1. As can be seen in the figure, the motion starts around the upper equilibrium, grows and touches the stable manifold of the saddle in the middle, leaves the upper well via the stable manifold and is injected into the lower well via the unstable manifold of the saddle, escapes again to the upper well and oscillates for a few cycles between the two wells, finally comes closer to the highly stabilized lower fixed point and ends in small periodic oscillations around it.

The oscillation between the two wells is qualitatively the same using more mode shapes in the model. Using a three-mode model, Figure 3.17 shows the forced oscillation of the actuator when a DC voltage in the bi-stability region for three-mode-model is applied $V_{DC} = 100$ V along with a small AC voltage of 0.9 V. The trajectory starts from an initial condition close to the upper fixed point, it escapes to the lower well and then is attracted to a small limit cycle in that well. The oscillatory nature of the trajectory in the phase plane reveals the characteristic multiple frequency response of the multi-mode model. Although the multi-mode-model results have quantitative differences with the single-mode

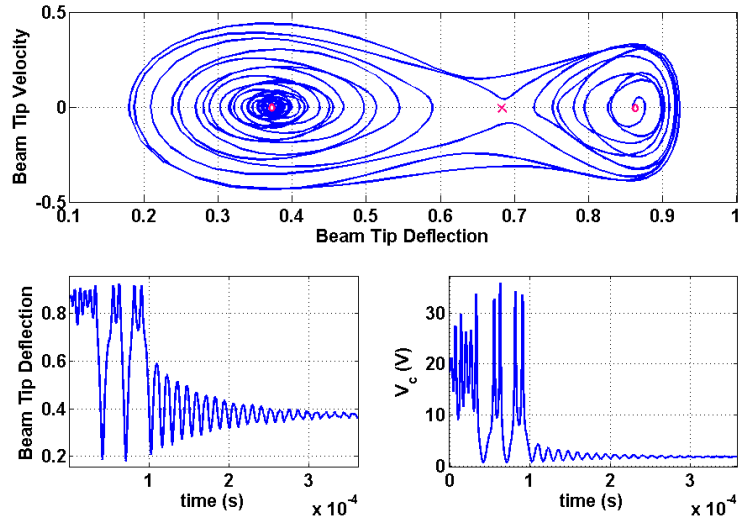


Figure 3.16: The phase portrait, beam displacement and controller output voltage for $\mu = 0.1$, $\omega = 4.45$, $V_{AC} = 0.86 V$ and the initial conditions ($q_1 = 0.86$, $\dot{q}_1 = 0$, $V_c = 18.43 V$).

model results, they are qualitatively the same. A comprehensive study of the steady-state dynamic behavior of the actuator can be performed by sweeping the magnitude and frequency of the excitation voltage as illustrated in the following sections.

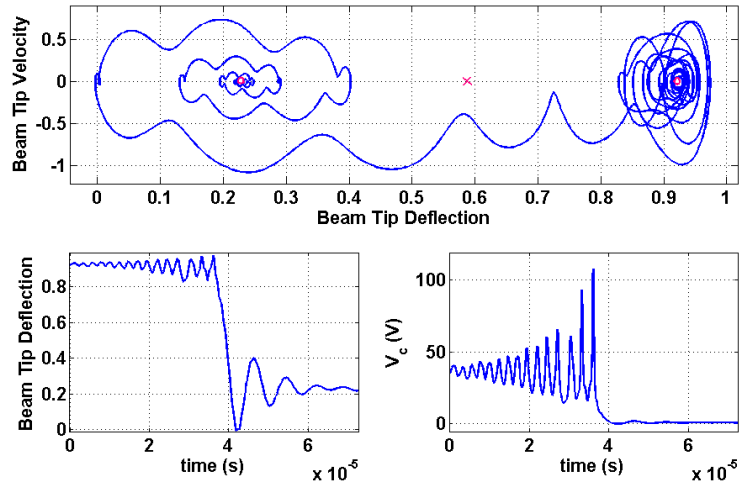


Figure 3.17: The phase portrait, beam displacement and controller output voltage for a three-mode model $\mu = 0.7$, $\omega = 2.8$, $V_{DC} = 100 V$, $V_{AC} = 0.9 V$, and the initial conditions ($q_1 = 0.91$, $\dot{q}_1 = 0$, $V_s = 35.7 V$).

3.5.3 Force Sweep

We sweep the amplitude of the harmonic excitation voltage V_{AC} while holding the excitation frequency fixed at the natural frequency of the lower equilibrium $\omega_l = 1.98 \equiv 86 \text{ kHz}$ (Table 3.3), to obtain the bifurcation diagram of the actuator shown in Figure 3.18. The dynamic system is integrated for a duration of 4000 periods of excitation and the data for the last 128 periods is presented. Poincaré sections are taken by sampling the data at the period of excitation starting from the maximum displacement. The amplitude of excitation starts at 4 V, and once we increase it, the amplitude of response increases until we observe a cascade of period doubling including period 2, and period 4 illustrated in Figure 3.19. Results are shown for the last 100 time units after the transients disappeared at 4, 4.4 and 4.7 V. The number of times the orbit crosses the zero velocity axis divided by two indicates the period number and each orbit completes in period number multiplied by the period of excitation. Multiple periods are also identified by the FFT from the beam tip displacement time series. In the FFT of the period 2 (Figure 3.19 (b)), in addition to the peaks at the period one $n\omega_l$ (3.19 (a)), we see intermediate peaks at $\frac{n}{2}\omega_l$. This trend is also seen in the FFT of period 4 (3.19 (c)).

Period doubling cascade in Figure 3.18 culminates in chaos. The last observable period doubling results in a period 8 followed by chaos in the lower well as the attractor size keeps increasing. Chaos occurs in two bands, one around the lower equilibrium and the other around the middle saddle. The size of the lower band is larger than the upper band. The phase portrait of the chaotic attractor is shown in Figure 3.20 for the voltage of 4.861 V. The two band attractor is clearly seen, and the difference in the size is obvious from comparing the number of zero-velocity axis crossings in the neighborhoods of 0.4 and 0.75 of the gap. A zoom on the area in the FFT plot in Figure 3.20 by the rectangle area in Figure 3.20 (b) is shown in in Figure 3.20 (c) revealing a broad range of frequencies, characteristic of chaotic vibrations. The actuator oscillates primarily in the lower well with brief excursions over the saddle into the upper well. Comparing these results to Nayfeh et al. [69] and Najar et al. [70] that reported period doubling followed by pull-in in a single-well actuator, we conclude that the upper well functions as a barrier against pull-in in this case. In other words, once the energy level of the orbit exceeds that of the lower potential well, it passes the potential hump to the upper well that consumes this additional energy and therefore protecting it from pull-in and letting the chaos happen.

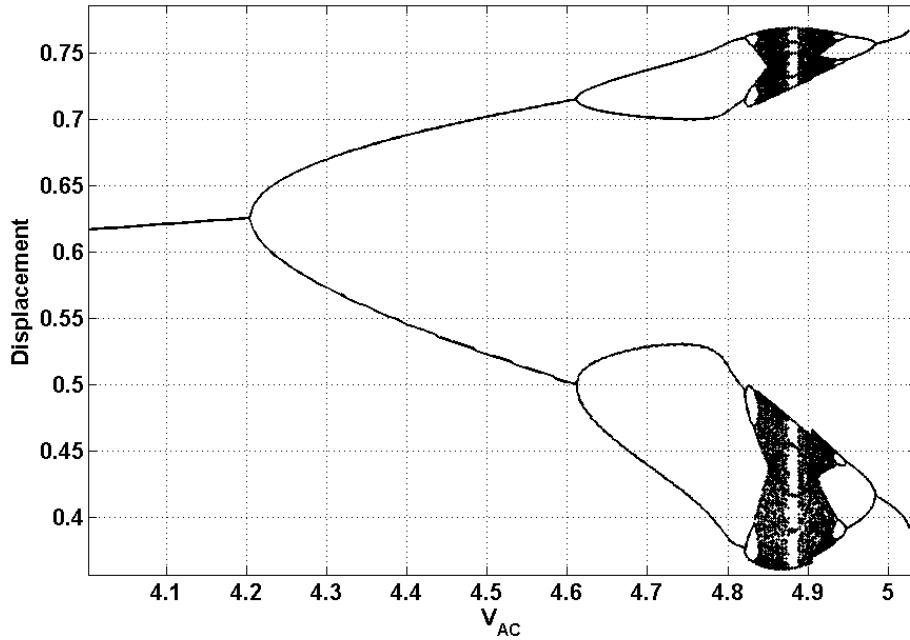


Figure 3.18: The bifurcation diagram of the actuator constructed from a force sweep V_{AC} at the natural frequency of the lower equilibrium $\omega_l = 1.98 \equiv 86 \text{ kHz}$.

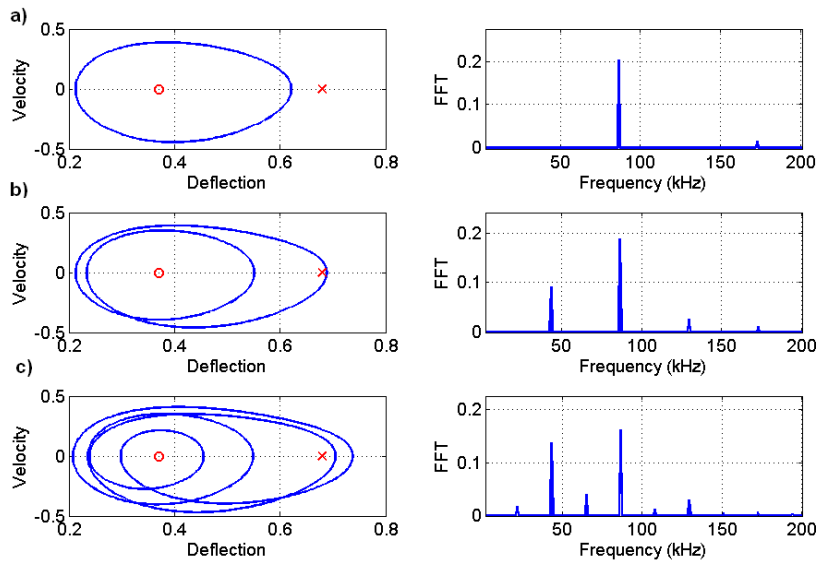


Figure 3.19: The nondimensional phase portraits and fast fourier transforms (FFT) using a one-mode model, the system parameters $\mu = 0.7, \omega = 1.98 \equiv 86 \text{ kHz}$, a) Period 1 $V_{AC} = 4.1 \text{ V}$, b) Period 2 $V_{AC} = 4.4 \text{ V}$, c) Period 4 $V_{AC} = 4.7 \text{ V}$.

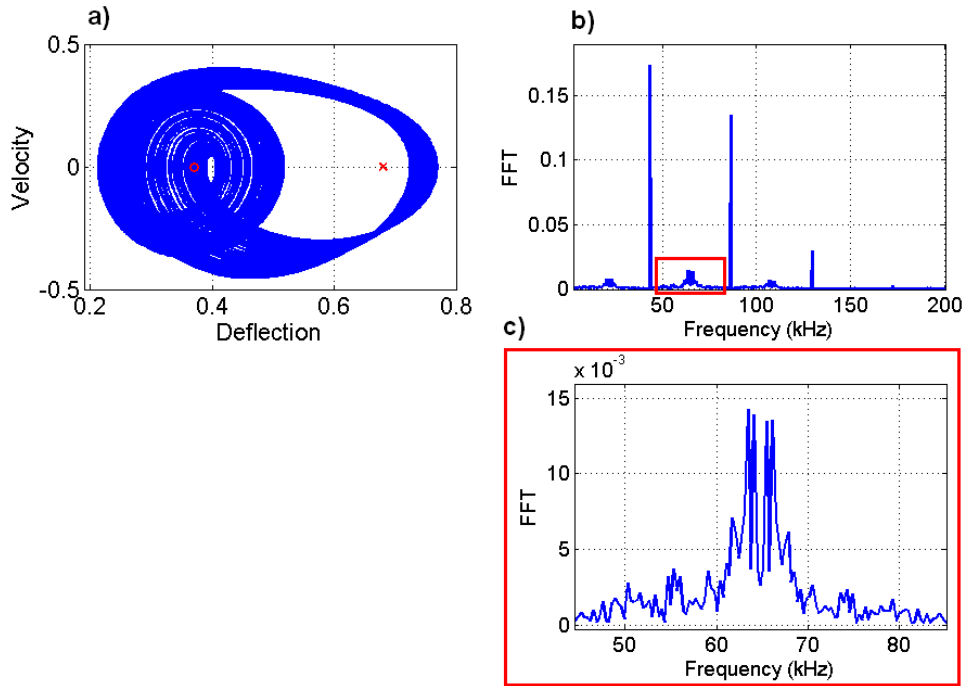


Figure 3.20: The nondimensional phase portrait and FFT of the chaotic attractor at $\mu = 0.7, \omega = 1.98 \equiv 86 \text{ kHz}, V_{AC} = 4.861 \text{ V}$.

Inside the chaotic attractor presented in Figure 3.18, a period 10 window appears for the excitation voltage range of $[4.875 - 4.888]$. The phase portrait of this periodic orbit is shown in Figure 3.21. The orbit crosses the zero velocity axis 20 times, which shows the period number to be 10. Chaos continues after that and the attractor size starts to decrease. A chaotic orbit in that region is illustrated in figure 3.22. The chaotic attractor size is smaller compared to that in Figure 3.20 and the chaotic bands are gradually shrinking. Chaos finally disappears through a cascade of reverse period doubling bifurcation ending in a period 2 orbit at $V_{AC} = 5.03 \text{ V}$, beyond which pull-in occurs. No stable orbits exist beyond this point.

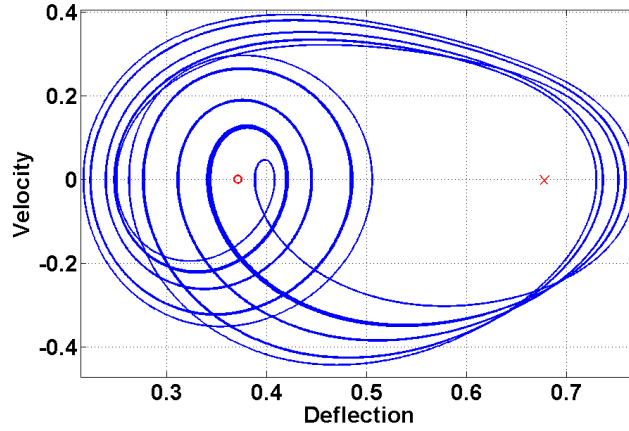


Figure 3.21: Phase portrait of the period 10 orbit at an excitation amplitude $V_{AC} = 4.883$ V and the frequency of excitation $\omega_l = 1.98 \equiv 86$ kHz.

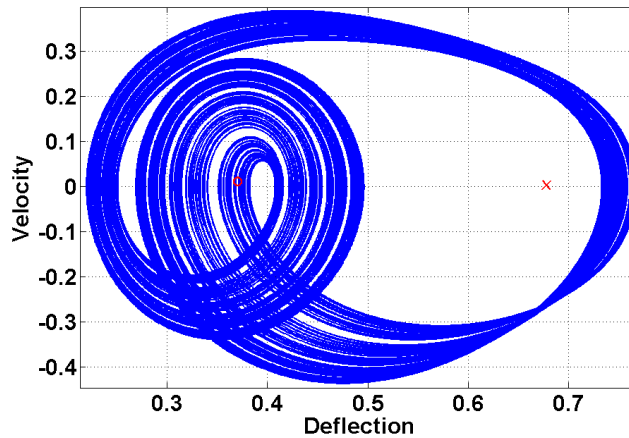


Figure 3.22: Phase portrait of a primarily one-well chaotic attractor at an excitation amplitude $V_{AC} = 4.9$ V and the frequency of excitation $\omega_l = 1.98 \equiv 86$ kHz.

3.5.4 Frequency Sweep

A two-well chaotic attractor is obtained by sweeping the frequency of excitation at a fixed AC amplitude of 4 V. Frequency sweeps at AC voltages smaller than 4 V were further studied by Seleim [71], who showed that the attractors shrink with smaller AC excitations. The complete picture of the bifurcation diagram is given in Figure 3.23 using the same

Poincaré section method used for the force sweep in the previous section, sampling the phase portrait orbit at the period of excitation starting from the maximum displacement.

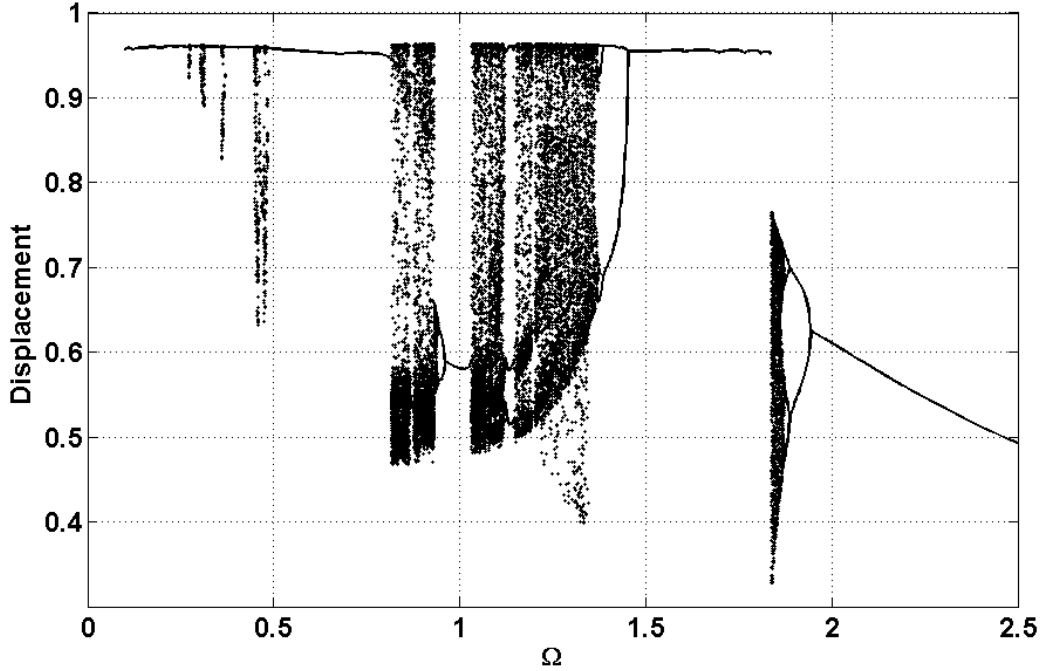


Figure 3.23: The bifurcation diagram sweeping the frequency of excitation at $V_{AC} = 4$ V, single-sided Poincaré sections obtained at the period of excitation.

An alternative method was employed to obtain the Poincaré sections used to construct the bifurcation diagram in Figure 3.24. The new Poincaré sections record the displacement magnitude as the orbit crosses the zero velocity axis. The bifurcation diagram in Figure 3.24 provides a better depiction of the orbit growth and the chaotic attractor. For the frequencies above the natural frequency of the lower equilibrium, $\omega_l = 1.98 \equiv 86$ kHz, there only exists lower-well periodic orbits. Once we decrease the frequency below the natural frequency, a cascade of period doubling bifurcations develops into the primarily one-well chaotic attractor. The bifurcation diagram shows the softening behavior typical for electrostatic actuators. The one-well chaos disappears by decreasing the frequency and changes to a periodic two-well orbit. Subsequently at a frequency of $\Omega = 1.45$, a period doubling cascade happens to the two-well orbit culminating in a two-well chaotic attractor. It continues while decreasing the frequency and a periodic window containing period three

orbits appear in the frequency range $[1.122 - 1.143]$.

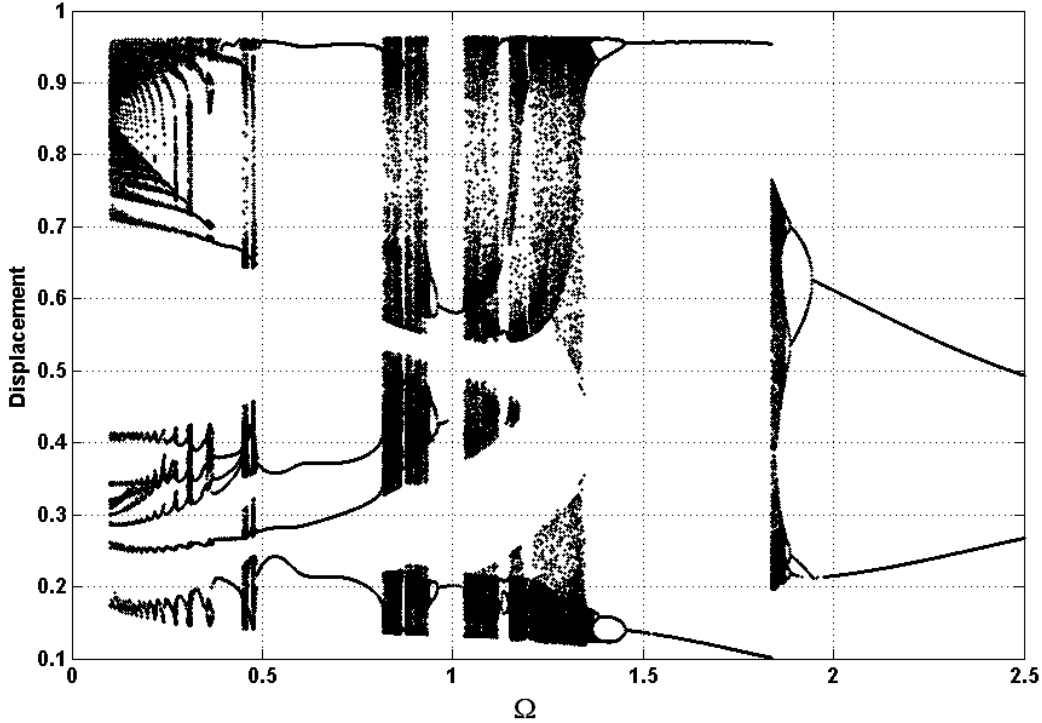


Figure 3.24: The bifurcation diagram sweeping the frequency of excitation at $V_{AC} = 4$ V, double-sided Poincaré sections obtained at the intersection with the zero velocity axis.

The chaotic attractor disappears to be replaced by a period one orbit in the lower well at $\Omega = 1.031$. In this range, the superharmonic resonance of order two $\Omega = \frac{\omega_L}{2}$ strengthens the regularity of the actuator oscillations, thereby eliminating the chaotic attractor and replacing it with a periodic orbit. A weaker softening behavior is also observed around this frequency that converts to a period doubling cascade and takes the orbit back to two-well chaos. The two-well chaos changes to superharmonic orbits that continues to exist down the frequency with occasional chaotic oscillations.

The appearance of large two-well orbits at low excitation frequencies compared to small one-well orbits at frequencies around the natural frequency of 1.98 can be explained by considering the total energy of the system. The total input energy of the system per cycle

is

$$E_{in} = 4 \int_0^{T_0/4} \vec{F}_e \cdot \vec{v} dt = 4F_e X \Omega \int_0^{T_0/4} \sin(\Omega t) \cos(\Omega t) dt = F_e X \cos 2\Omega t \Big|_0^{T_0/2} = -2F_e X \quad (3.56)$$

where \vec{F}_e is the electrostatic force vector, \vec{v} is the velocity response vector, X is the magnitude of displacement response, and T_0 is the period of excitation. Therefore, the input energy is constant versus frequency of excitation, while the kinetic energy per cycle is a linear function of the excitation frequency:

$$\begin{aligned} E_k &= 4m \int_0^{T_0/8} v^2 = 2mX^2\Omega^2 \int_0^{T_0/4} \cos^2(\Omega t) \\ &= 4mX^2\Omega^2 \left(\frac{t}{2} + \frac{\sin(2\Omega t)}{4\Omega} \right) \Big|_0^{T_0/8} = mX^2\Omega \left(\frac{\pi}{2} + 1 \right) \end{aligned} \quad (3.57)$$

Therefore, at low excitation frequencies, the kinetic energy is low, so the potential energy has to absorb the orbit energy via a large displacement variation over the orbit. As the excitation frequency increases, the kinetic energy absorbs most of the input energy and consequently the potential energy and the orbit displacement shrinks leading to one-well periodic orbits.

Inspecting the bifurcation diagram, Figure 3.24, we observed superharmonic resonances of order two at $\frac{\omega_l}{2} = 0.99$, three at $\frac{\omega_l}{3} = 0.66$, and six at $\frac{\omega_l}{6} = 0.33$. In Figure 3.25, the phase portraits and the FFT of these orbits are presented. The period for each orbit is the same as the period of excitation and the number of FFT peaks below and including the natural frequency reveals the order of the superharmonic resonances.

To illustrate the chaotic oscillation observed, the phase portraits, the Lyapunov exponents, the displacement time series and controller output voltage of the one-well chaotic attractor at $\Omega = 1.84$, and the two-well attractor at $\Omega = 1.081$ are shown in Figures 3.26 and 3.27 respectively. The one-well attractor is fully developed and located primarily in the lower well with occasional excursions over the saddle, marked by an \times in Figure 3.26 (a), as illustrated in the phase portrait and displacement time series in parts (a) and (c). The two-well attractor consists of oscillations in the lower well and between the two wells, but non that are exclusively in the upper well. The leading Lyapunov exponents are obtained by tracking the distance $d_1(t)$ between two trajectories in phase space starting from initial conditions at a distance $d_0 = 10^{-9}$ from each other. The Lyapunov exponents are

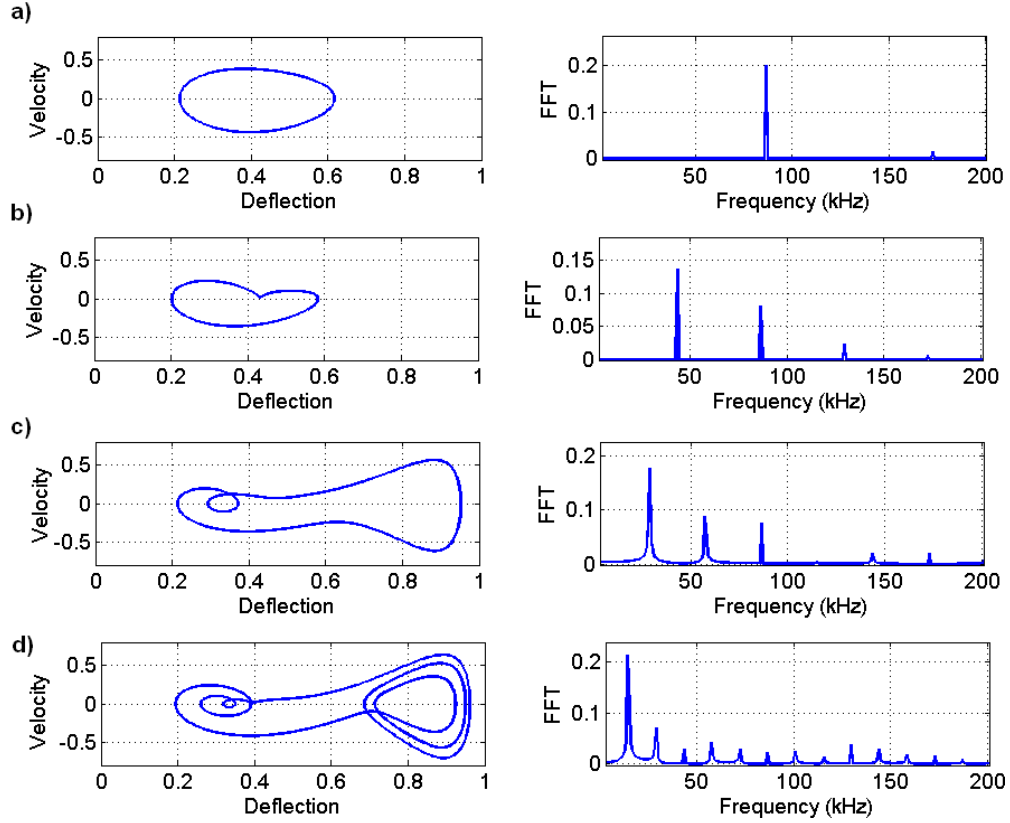


Figure 3.25: Phase portraits and FFT for the periodic orbits at the a) natural frequency of the lower equilibrium $\Omega = \omega_l = 1.98 \equiv 86 \text{ kHz}$ b) the superharmonic resonance of order two $\Omega = \frac{\omega_l}{2} = 0.99 \equiv 43 \text{ kHz}$ c) the superharmonic resonance of order three $\Omega = \frac{\omega_l}{3} = 0.66 \equiv 28 \text{ kHz}$ d) the superharmonic resonance of order six $\Omega = \frac{\omega_l}{6} = 0.33 \equiv 14 \text{ kHz}$.

found for synchronized points along the trajectories. The time evolution of the logarithm of the distance $d_1(t)$ normalized with respect to the initial distance are illustrated in Figures 3.26(b) and 3.27(b) by the dotted lines and their moving averages over 10 points are shown by solid lines. The slope of the solid curve during the chaotic attractor expansion is the leading Lyapunov exponent. It is found to be positive for both attractors proving that they are indeed chaotic [30].

We observe that the two-well chaotic attractor consumes 8 times larger controller voltage, 80 V vs. 10 V, than the voltage used by the one-well chaotic attractor as presented in part (d) of Figures 3.26 and 3.27. Thus, setting the controller to produce the one-well

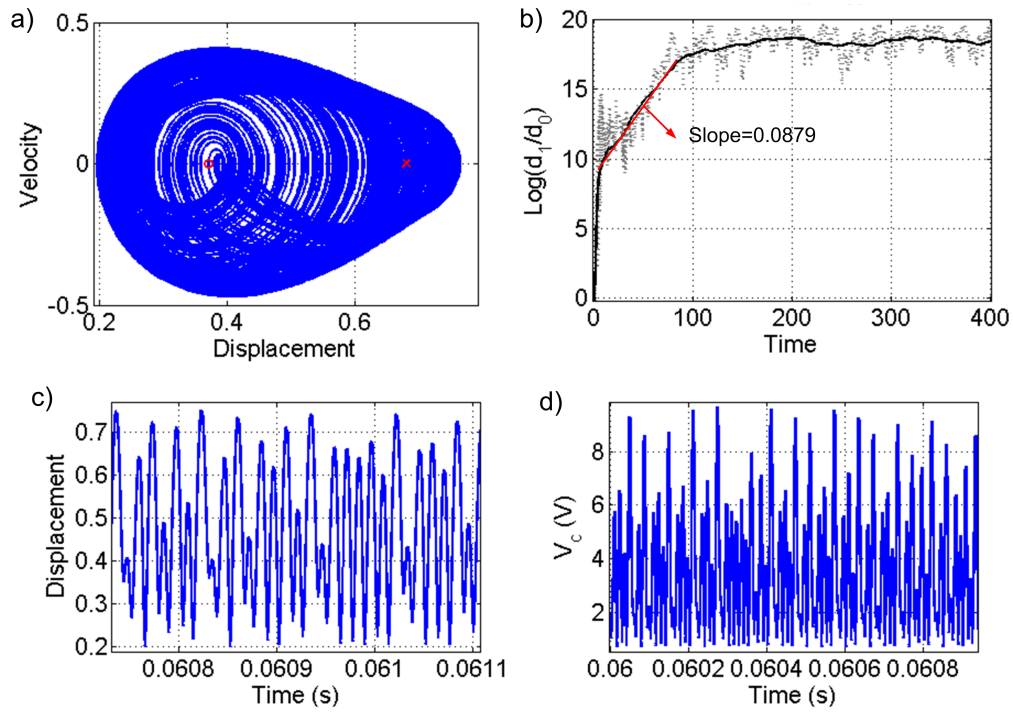


Figure 3.26: a) Phase portrait, b) Lyapunov exponent c) Displacement time history d) controller output voltage of the one-well chaotic attractor when $V_{AC} = 4$ V and $\Omega = 1.84$.

chaos reduces the demand on the circuit components. However, the creation of chaos using two potential wells may be beneficial where a large displacement signals are desired for detection purposes.

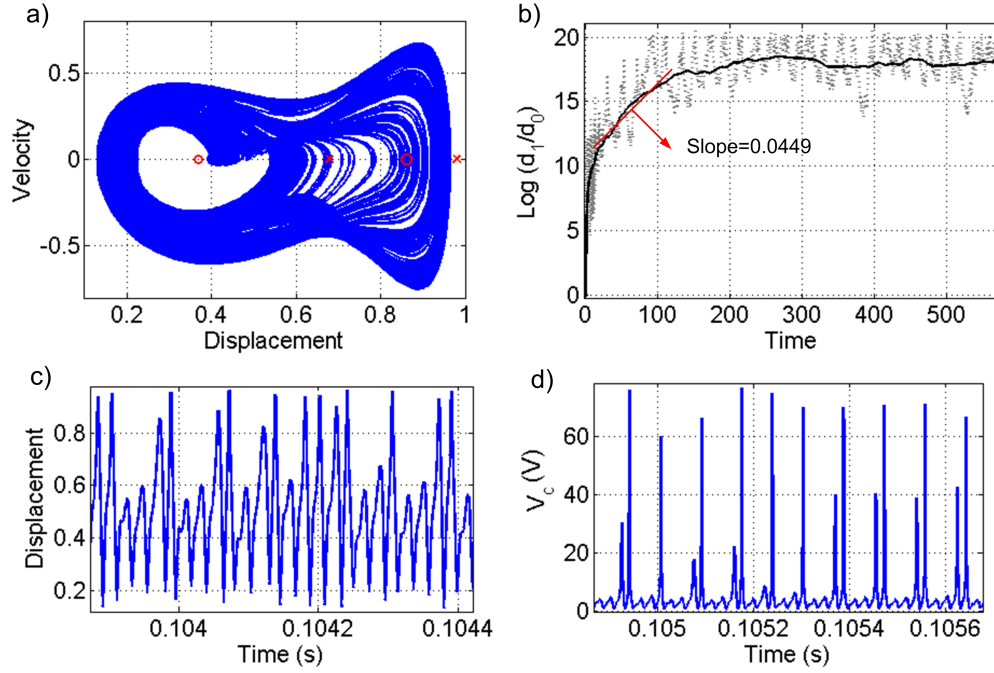


Figure 3.27: a) Phase portrait, b) Lyapunov exponent c) Displacement time profile d) controller output voltage of the two-well chaotic attractor when $V_{AC} = 4$ V and $\Omega = 1.081$.

3.6 Actuator Realization

The dimensions of the actuator were revised to allow us to use the standard POLYMUMPS fabrication technology provided by Canadian Microelectronics Corporation (CMC) Microsystems. Polysilicon beams were fabricated using poly 1 layer with nominal lengths of 125,150, and 170 μm and gap and thickness of 2 μm , the substrate electrodes were made of poly 0 layer. The static and dynamic simulations are then repeated for the actuator dimensions listed in Table 3.4. The controller parameters are optimized to reduce the operating voltages. Figure 3.28 presents the static profile for the beams with a nominal length of 150 μm . The bi-stability DC voltage range is between 18.3-19.16 V, the DC and AC working voltages are reduced from 110 V and 4 V to 18.5 V and 0.8 V, respectively compared to the actuator series I described in Table 3.1. At the DC voltage of 18.5, the

stable equilibrium points are located at 35% and 85.5% of the gap and the saddle is at 72% of the gap.

Table 3.4: Actuator Series II parameters

Parameter	Symbol	Value
Displacement Gain	Ψ	0.5 V
Voltage Gain	G	1.3
Beam Length	L	166 μm
Beam Width	b	10 μm
Beam Thickness	h	2.2 μm
Initial gap	d	2.1 μm
Damping coefficient	μ	0.56
Modulus of Elasticity	E	150 GPa
Controller damping	r	100

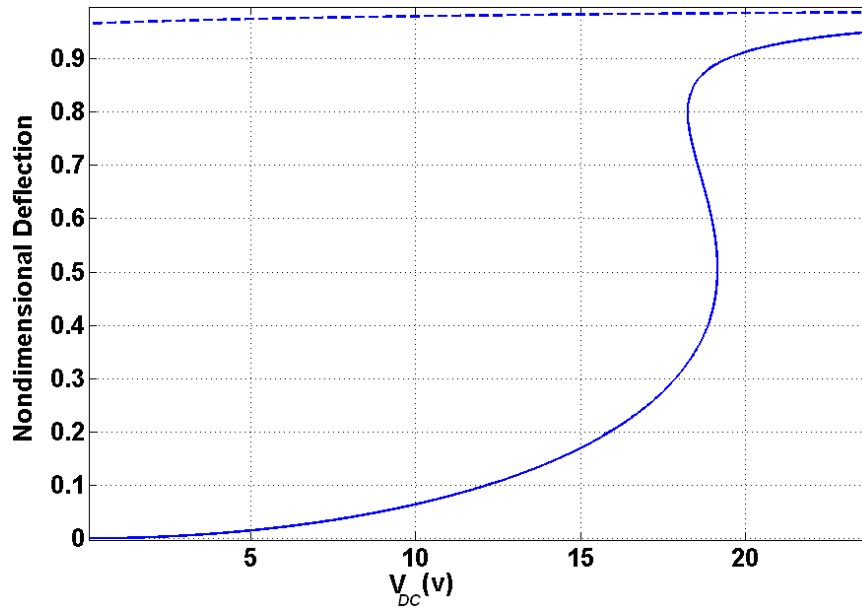


Figure 3.28: Static profile for the actuator series II in Table 3.4.

A frequency sweep for the actuator in Figure 3.28 is illustrated in Figure 3.29. The

Poincaré sections represent the displacement magnitude at the intersection of the orbit with the zero velocity axis. The results are qualitatively similar to what obtained in Figure 3.24. Decreasing the frequency from the natural frequency of the lower equilibrium, $\omega_l = 2.11$ equivalent to 62 kHz, the periodic orbits and period doubling cascade appear in the lower well. However, the one-well chaos rapidly switches to a two-well chaos at the excitation frequency of 2 and continues until the periodic orbit between the two wells arises at $\Omega = 1.878$. In the previous case, the one-well chaos converted to a two-well periodic orbit without evolving into two-well chaos. The period doubling cascade to two-well chaos continues down the frequency spectrum and superharmonic resonances appear in the neighborhood of the half of the natural frequency at $\frac{\omega_l}{2} = 1.05$. Chaos exists with periodic window intervals including period 10 at $\Omega = 1.432$, and period 4 at $\Omega = 1.344$. An example of period 4 is given in Figure 3.30. In this figure, the velocity and displacement profiles are shown in parts (b) and (d) respectively confirming the period 4 existence by having periods that are four times the excitation period, $1e - 4$ s vs. $2.53e - 5$ s. The controller voltage is also depicted in part (c) of the figure revealing that the controller yields a large displacement without exceeding a controller voltage of 15.2 V.

Two examples of the two-well chaotic attractor of actuator series II are also presented in Figures 3.31 and 3.32, where parts (b) and (d) reveal the infinite-period response of chaotic oscillations. The attractor presented in Figure 3.32 involves mostly two-well oscillations requiring controller output voltage of up to 18 V, while the chaotic attractor in Figure 3.31 involves mostly lower-well with maximum controller output voltage of 4.5 V. A significant advantages of the actuator series II is that the actuator demonstrates two-well chaos and displacements up to 90% of the gap at reduced controller voltage (as small as 4.5 V in part (d) of the Figure 3.31), while a similar behavior in the actuator series I required 80 V as in Figure 3.27.

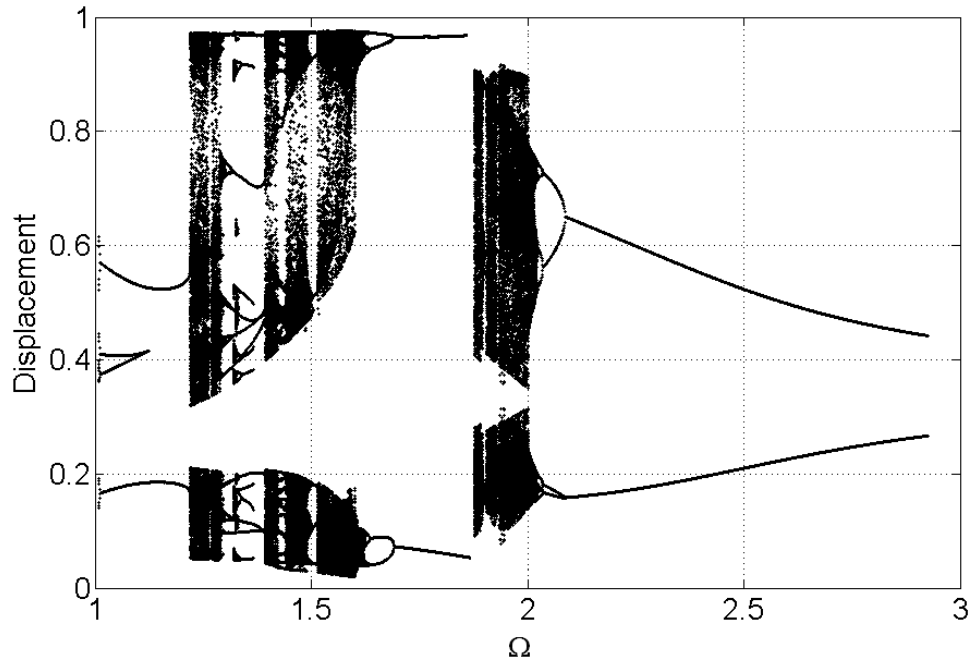


Figure 3.29: The bifurcation diagram sweeping the nondimensional frequency of excitation at fixed $V_{DC} = 18.5$ V, $V_{AC} = 0.8$ V for the actuator series II in Table 3.4.

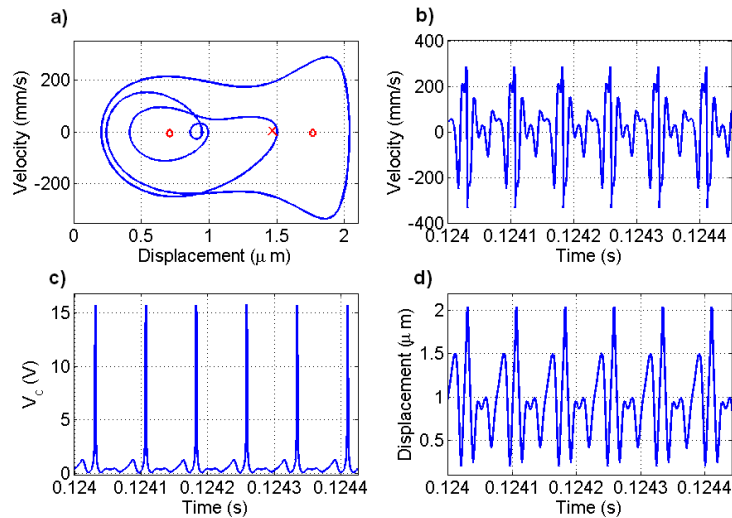


Figure 3.30: a) Phase portrait b) velocity time history c) controller output voltage d) displacement time history of the period four at $V_{DC} = 18.5$ V, $V_{AC} = 0.8$ V and $\Omega = 1.344 \equiv 34.5$ kHz for the actuator series II in Table 3.4.

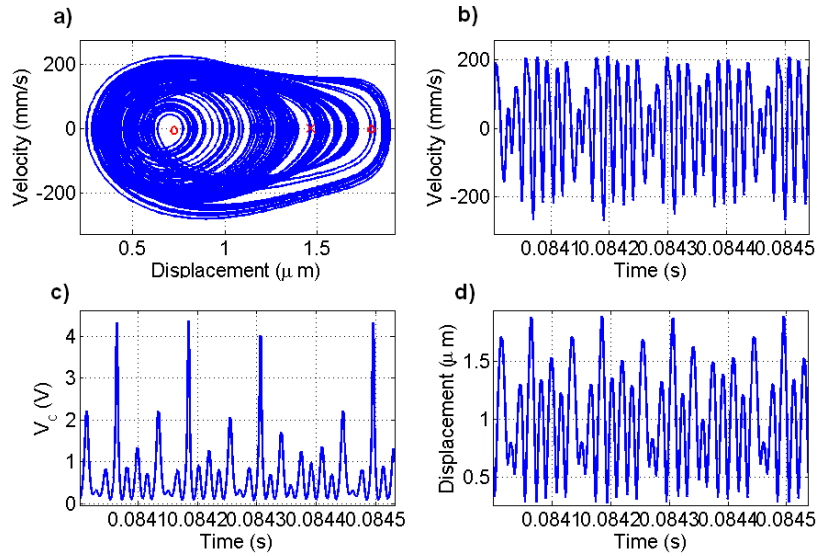


Figure 3.31: a) Phase portrait b) velocity time history c) controller output voltage d) displacement time history of the chaotic attractor at $V_{DC} = 18.5$ V, $V_{AC} = 0.8$ V and $\Omega = 1.975 \equiv 58$ kHz for the actuator series II in Table 3.4.

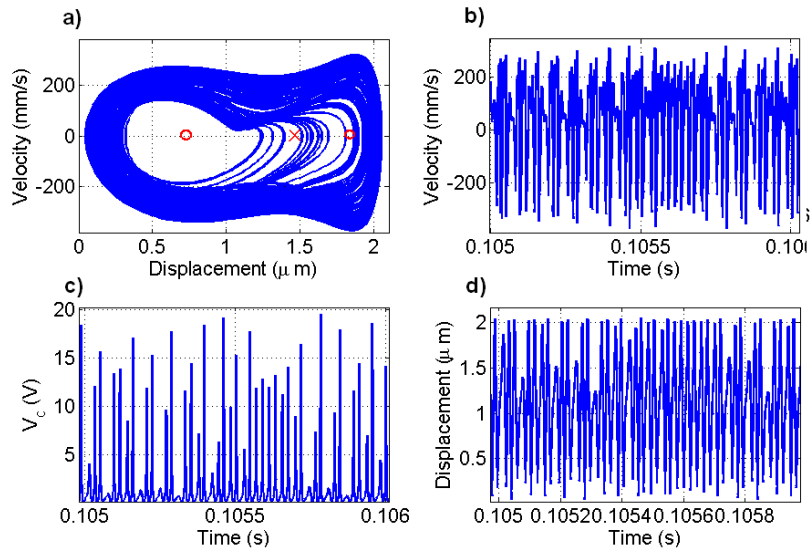


Figure 3.32: a) Phase portrait b) velocity time history c) controller output voltage d) displacement time history of the chaotic attractor at $V_{DC} = 18.5$ V, $V_{AC} = 0.8$ V and $\Omega = 1.58 \equiv 46.4$ kHz for the actuator series II in Table 3.4.

3.7 Summary

In this chapter, an extensive simulation study is conducted for an electrostatic actuator that yield both uniquely stable and bi-stable behavior using a voltage regulator. Nonlinear elements present in the mathematical model include a voltage regulator and the electrostatic forcing. Static and dynamic responses of the nonlinear system are explored. The static response shows that by setting the controller gains, the system can be configured as either a stable larger-stroke actuator or a bi-stable actuator. The larger-stroke actuator has an extended travel as much as 83% of the capacitor gap, much larger than the pull-in deflection of 45% of the open-loop electrostatic actuator beneficial to many optical sensor applications. The bi-stable system, on the other hand, is used to create multiple-frequency and chaotic micro-resonators potentially used in sensors with improved resolution. We found that bi-stability was necessary but not a sufficient condition for chaos. The excitation AC voltage amplitude and frequency had to be chosen properly to obtain chaos.

Both one-well and two-well chaotic attractors have been found. The excitation parameter boundaries of the chaotic attractors were obtained using force and frequency sweeps. Period doubling, reverse period doubling cascades and a banded one-well chaotic attractor were obtained in the force sweep. In addition, sweeping the frequency of excitation, we observed one-well and two-well chaotic attractors. A softening-type nonlinearity beside superharmonic resonances are observed in the response as we decrease the excitation frequency below the natural frequency.

Validation of the simulations are performed in the next chapter for the large-stroke actuator accompanying more detailed study of the system behavior. Due to the time limitation, the chaotic resonator was not tested experimentally, but the controller system was precisely designed in the current chapter to accommodate to the fabricated micro-actuator dimensions.

Chapter 4

Low Frequency Experiment

In this chapter, the closed loop system designed for the large-stroke actuator in Chapter 3 is implemented and the simulations are validated. The parameters of the closed loop model are determined from the open loop test and modifications are made to the closed loop system for low frequency testing. The modified low frequency controller is introduced [72] to bring the actuator to a high target position statically. Observations of the superharmonic resonances during testing that could lead to chaos are also reported at the end of this chapter.

4.1 Open Loop Actuator

4.1.1 Open Loop Experiment Configuration

The equipment used for open loop testing included a function signal generator, an oscilloscope, MEMS actuators, a vacuum pump, and a Polytech Microscope Scanning Vibrometer (MSV) 400. A picture of the experimental configuration is shown in Figure 4.1. The MEMS actuator and probes used for excitation were held stationary in place using the vacuum pump. The excitation voltage was provided by the internal generator of the MSV or the external function generator.

The actuator out of plane velocity was measured with the MSV which is comprised of a sensor head, a digital camera, a scanner unit, a decoder, a junction box, and a Personal

Computer (PC). A measurement laser beam is directed to the micro-actuator by a sensor head connected to the scanner unit. The incident laser beam is scattered because of the actuator motion; the scattered beam is allowed to interfere with a reference laser beam and the resulting interference pattern, which is proportional to the velocity of the actuator, is recorded by a photo detector inside the sensor head (see Figure 4.2). The interference signal is then converted to a voltage signal in the decoder which digitizes the signal and displays the corresponding velocity on the PC [73]. The vibrometer also contains a junction box to provide connections between different units and an external reference or trigger signal.

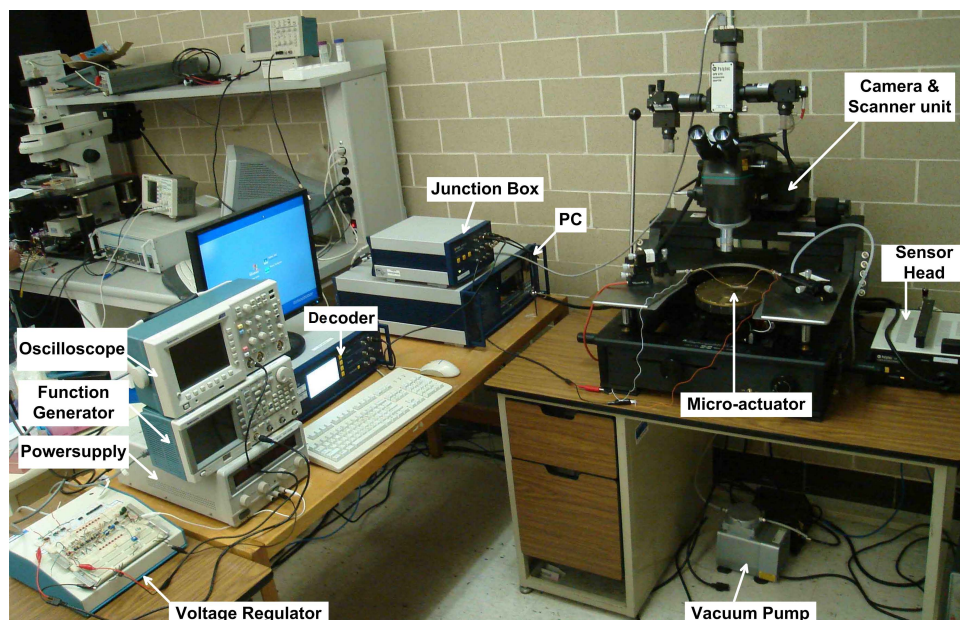


Figure 4.1: Experimental configuration.

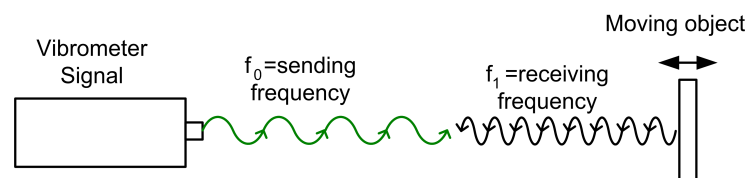


Figure 4.2: Doppler effect principle

The vibrometer enables velocity measurement in the range of $0.15 \mu\text{ m/s}$ to 10 m/s using

the velocity decoder. A displacement decoder can also be used to measure displacements in the range of 0.1 pm to 75 nm, which is small compared to actuator gaps of 2 μm .

All the tests were conducted in open air with all environmental disturbances present. Therefore, efforts were made to minimize the noise using data processing techniques.

4.1.2 Data Processing

The vibrometer is equipped with a Polytech Scanning Vibrometer (PSV) data processing software unit where the measurements are made and processed. To reduce the noise, synchronized time traces of velocity signals were averaged. The time traces had the same number of samples and were synchronized with the voltage excitation signal. Synchronization was necessary to average the data at the same phase achieved by using a trigger signal provided by the function generator.

The recorded velocity signal displayed on the vibrometer PC can easily be misrepresented because of aliasing if the data acquisition card does not collect enough samples per cycle. The aliasing effect, as illustrated in Figure 4.3, occurs because sampling at 1 Hz yields the same reconstructed signal for two signals with different frequencies of 0.1 Hz and 0.9 Hz. To avoid this erroneous effect, the sampling frequency was set much larger than the excitation frequency. For instance, for the excitation frequency of 10 kHz, the sampling frequency was set to 5.12 MHz, the resolution of which is 195 ns, thus collecting 512 data points in each cycle.

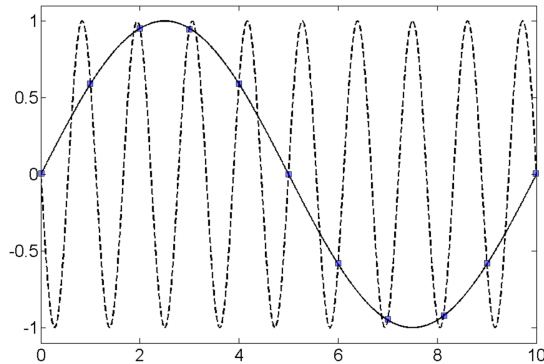


Figure 4.3: Two signals with frequencies of 0.1 Hz and 0.9 Hz appear identical under a sampling rate of 1 Hz. (Aliasing effect).

To improve accuracy in the frequency domain measurements complex averaging was used. For each time trace, a spectrum was obtained and the values at each frequency were averaged. Complex averaging consisted of averaging the imaginary and real parts of the FFT lines separately [73]. The voltage excitation signal was used as a reference signal to set the phase of the measured signal.

The resolution of the measured signal was also enhanced by optimizing the dynamic range for each test. The output signal of the velocity decoder is adjustable up to ± 10 V with available dynamic ranges of 5, 25, 125, and 1000 $mm/s/V$. For increasing accuracy, if the maximum expected output signal was 9 mm/s , the output signal range was set to 2 V and the dynamic range to 5 $mm/s/V$ to obtain maximum resolution and minimum noise.

4.1.3 Actuators

The MEMS devices being tested are cantilever beam electrodes made of polysilicon fabricated using POLYMUMPS surface micromachining technology. The beam layout and cross section are shown in Figure 4.4 parts (a) and (b) respectively. The structural layers of the actuators are Poly 0 with the thickness of 0.5 μm for the fixed electrode and Poly 1 with the thickness of 2 μm for the moving electrode. The sacrificial layer was phosphosilicate glass (PSG) with the thickness of 2 μm that was etched away to create the electrostatic gap. The probing pads were made of all structural layers of Poly 0, Poly 1, Poly 2, and gold metal with the dimensions of $100 \times 100 \mu m$. The ground pad of the fixed electrode and the voltage pad of the moving electrode were located 200 μm apart from each other. Actuators with lengths of 125, 150, and 175 μm and widths of 10 and 20 μm were designed to have natural frequencies between 56 to 150 kHz . In early designs, 200 μm long beams and common ground pads between actuators were used but were avoided in future designs. Longer beams could have lower natural frequencies, which was desirable for testing, but the beam tips were found to be curled downward in many cases. Common ground pads were used to save space on the chip but the voltage leakage to non-excited actuators caused pull-in in some cases. Images taken from a final design of actuators by a white-light optical profiler and SEM are shown in Figures 4.5 and 4.6, respectively.

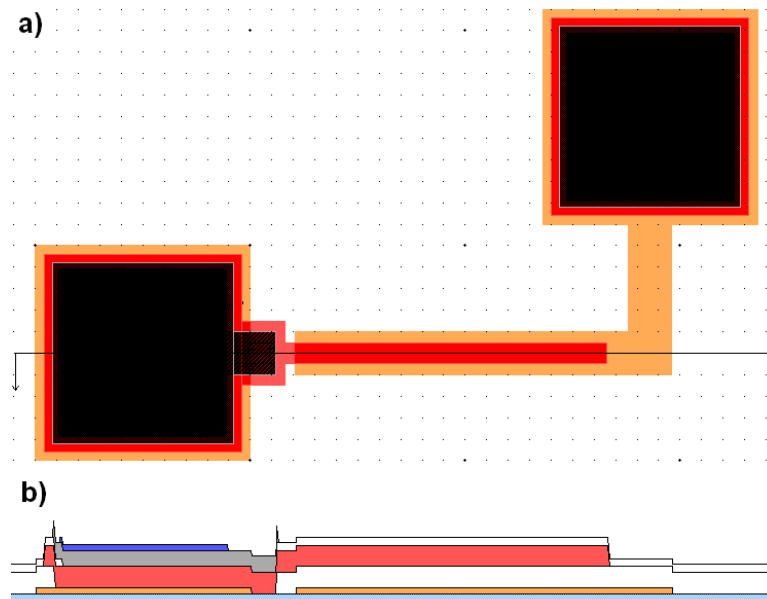


Figure 4.4: Layout of the actuators in MEMS Pro L-Edit software. a)Top view, b)cross section.

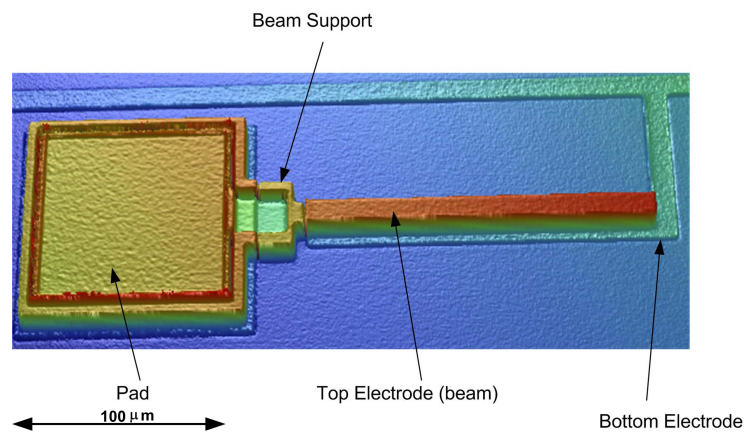


Figure 4.5: A white-light image of the electrostatic actuator by WYKO NT1100 Optical Profiler.

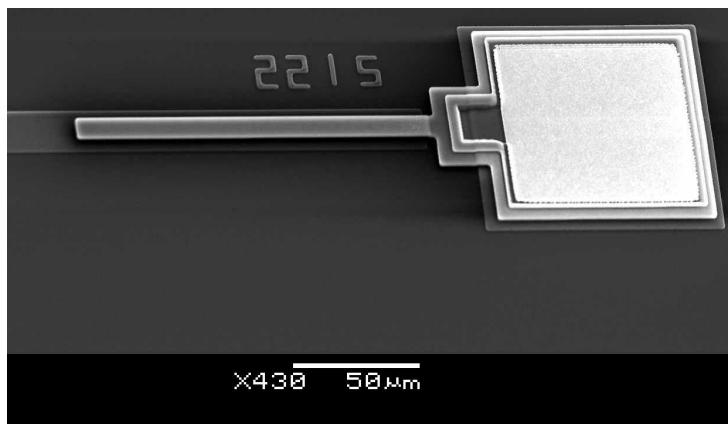


Figure 4.6: SEM image of the actuator fabricated with POLYMUMPS.

4.1.4 Parameter Identification

The beam parameters were identified experimentally in open-loop tests. A software macro was developed in PSV to excite the beam using a sinusoidal waveform at different frequencies and the Fast Fourier Transform (FFT) response peak was obtained. The peaks were recorded to find the frequency response of the beam. The frequency response was used to find the natural frequency of the beam and the damping coefficient and to estimate the capacitor gap. The chips used for testing contain beams with nominal lengths of 125, 150, and 175 μm . The parameters for each beam length were identified from frequency response tests. Figure 4.7 shows the frequency response curve for the 150 μm long beam. The amplitude of the response peaks rise by increasing the DC voltage at a constant AC voltage because of the increase in the electrostatic force, Eq. (2.1), which is proportional to the square of summation of DC and AC voltages.

As shown in Figure 4.7 the natural frequency drops as the DC voltage is increased. This effect is depicted in Figure 4.8 which shows the natural frequency as a function of DC voltage. The solid line shows the natural frequency obtained from solution of the eigenvalue problem obtained for Eq. (3.39), while the diamonds show the natural frequency measured from the frequency response peaks. From this graph, both the beam length and pull-in voltage can be identified. The beam support is assumed to be perfectly rigid in the simulation, while in reality the beam is connected to a wider post and the wide post is attached to a fixed pad (see Figure 4.5). In addition, under-etch occurs during the

wet etching step used to release the beam. Therefore, the effective beam length needs to be estimated experimentally to account for the flexibility in the support of the beam and the under-etch. That is done by finding the natural frequency at $V_{DC} = 0$ from:

$$\omega_n = \frac{f_n}{2\pi} \sqrt{\frac{EI}{\rho AL^4}} \quad (4.1)$$

where $f_n = 3.51518$ is the canonical natural frequency of the cantilever beam. Rearranging the above equation yields

$$L = \sqrt[4]{\frac{EI}{\rho A}} \sqrt{\frac{f_n}{2\pi\omega_n}} \quad (4.2)$$

substituting the second moment of area, $I = \frac{bh^3}{12}$ and the cross-sectional area $A = bh$ of a rectangular cross-section into the above equation, the effective beam length is simplified to

$$L = \sqrt[4]{\frac{Eh^2}{12\rho}} \sqrt{\frac{f_n}{2\pi\omega_n}} \quad (4.3)$$

where the beam thickness h can be estimated from an optical profilometer scan, such as shown in Figure 4.5. The effective beam length using the material properties listed in Table 4.1, thickness of $2.2 \mu\text{m}$, and the identified natural frequency of $\omega_n = 103.3 \text{ kHz}$ is then found to be $166.1 \mu\text{m}$. The pull-in voltage is also identified from Figure 4.8 where the natural frequency approaches zero. This figure reveals, from simulation, the magnitude of the pull-in voltage is 23.5 V .

The damping ratio is obtained from the compliance frequency response curve for the beam tip velocities in Figure 4.7 divided by individual frequencies. In the compliance graph of 4.9, the damping ratio is then

$$\zeta = \frac{\omega_a - \omega_b}{2\omega_p} \quad (4.4)$$

where ω_a , ω_b are the frequencies at which the magnitude of the response is $1/\sqrt{2}$ of the peak magnitude, and ω_p is the frequency at the peak. The damping ratio is obtained for voltages of $V_{DC} = 6 \text{ V}$, and $V_{DC} = 11.2 \text{ V}$ and was found to be 0.08 . Using the beam length, beam thickness, and damping ratio determined experimentally, equation (3.37) is solved numerically for voltage $V_{DC} = 9.07 \text{ V}$. The beam gap is estimated to be $2.1 \mu\text{m}$ to match the measured frequency response. The simulation result is shown by a solid line in Figure 4.10. The figure shows that the one-mode model with the experimentally identified parameters yields a good approximation of the open loop dynamic behavior.

Table 4.1: The electrostatic actuator material properties

Parameter	Symbol	Value
Density	ρ	2331 kg/m ³
Permittivity of air	ε	8.85×10^{-12} F/m
Modulus of Elasticity	E	150 GPa

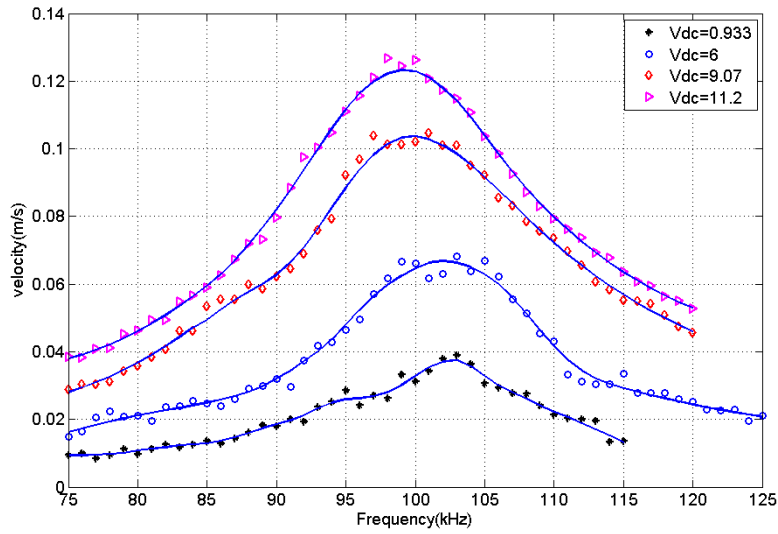


Figure 4.7: Frequency response of a beam with the nominal dimensions of $150 \times 10 \times 2 \mu\text{m}$ and a capacitor gap of $2 \mu\text{m}$ where the AC voltage is 2 V. Solid line shows the fitted data on the experimental results.

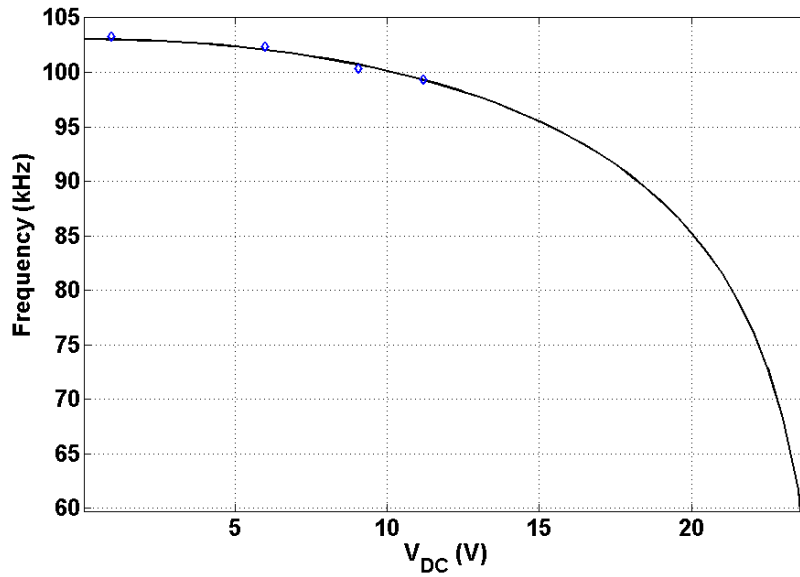


Figure 4.8: Natural frequency as a function of DC voltage for a beam with dimensions of $L = 166.1 \mu\text{m}$, $b = 10 \mu\text{m}$, $h = 2.2 \mu\text{m}$, and $d = 2.1 \mu\text{m}$: — Simulations, \diamond experimental results.

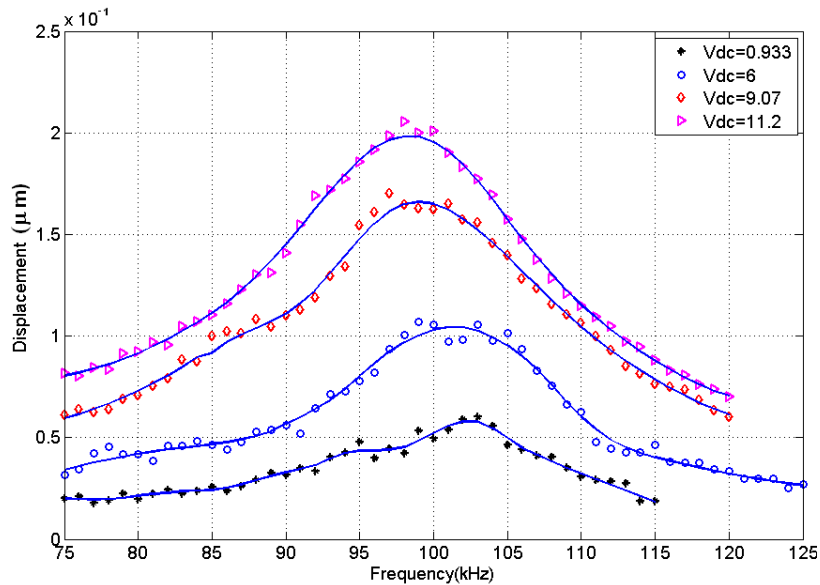


Figure 4.9: Compliance frequency response of a beam with dimensions of $150 \times 10 \times 2$ with gap of $2 \mu\text{m}$ when the applied AC voltage is 2 V.

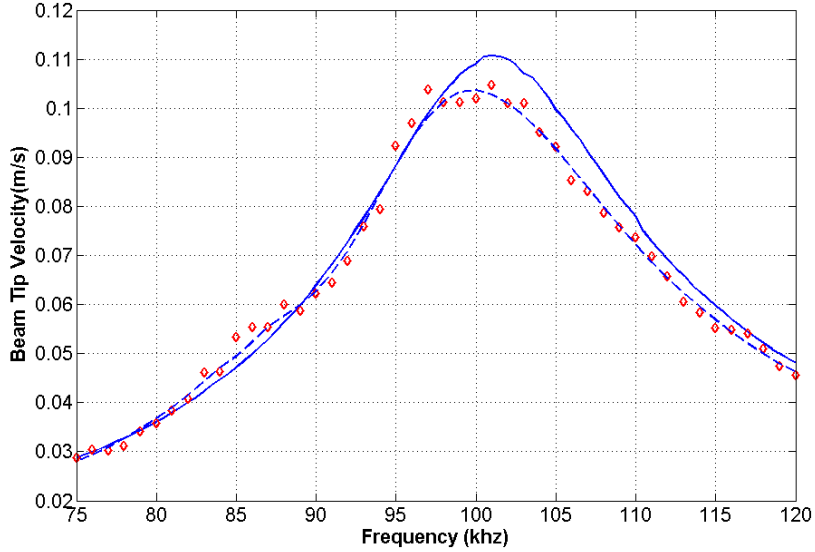


Figure 4.10: Frequency response of the beam tip velocity with dimensions of $L = 166.1 \mu\text{m}$, $b = 10 \mu\text{m}$, $h = 2.2 \mu\text{m}$, $d = 2.1 \mu\text{m}$ at $V_{DC} = 9.07 \text{ V}$, and $V_{AC} = 2 \text{ V}$: — Simulations, \diamond experimental results, - - fitted data on the experimental results.

The identification procedure was also performed for the beam with nominal length of $175 \mu\text{m}$. Figures 4.11 and 4.12 show the frequency response and compliance response respectively. As expected the $175 \mu\text{m}$ long beam in Figure 4.12 requires less voltage, 8.48 V versus 11.2 V , to reach the same amount of deflection, e.g. $0.2 \mu\text{m}$, compared to the shorter beam in Figure 4.9. The reason arises from the fact that the electrostatic force increases for a longer beam while the spring force decreases, thus the longer beam deflects more toward the bottom electrode at the same voltage. The beam thickness was found from the optical profiler scan to be $h = 1.9 \mu\text{m}$, and the capacitor gap is estimated as $d = 1.9 \mu\text{m}$ to match the simulation to the experimental results in Figure 4.13 which shows the natural frequencies as a function of DC voltage for the beam. The effective beam length was determined from this graph to be $L = 185 \mu\text{m}$ for the natural frequency at $V_{DC} = 0$, and the pull-in voltage was estimated to be 14 V at the zero frequency. The damping ratio was found to be $\zeta = 0.132$.

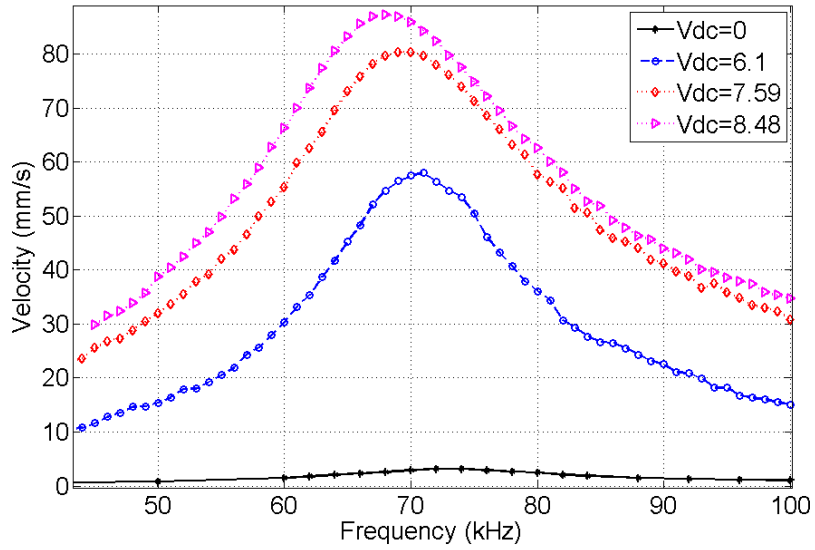


Figure 4.11: Frequency response of a beam with the nominal dimensions of $175 \times 10 \times 2 \mu\text{m}$ and a capacitor gap of $2 \mu\text{m}$ where AC voltage is 1.30-1.4 V.

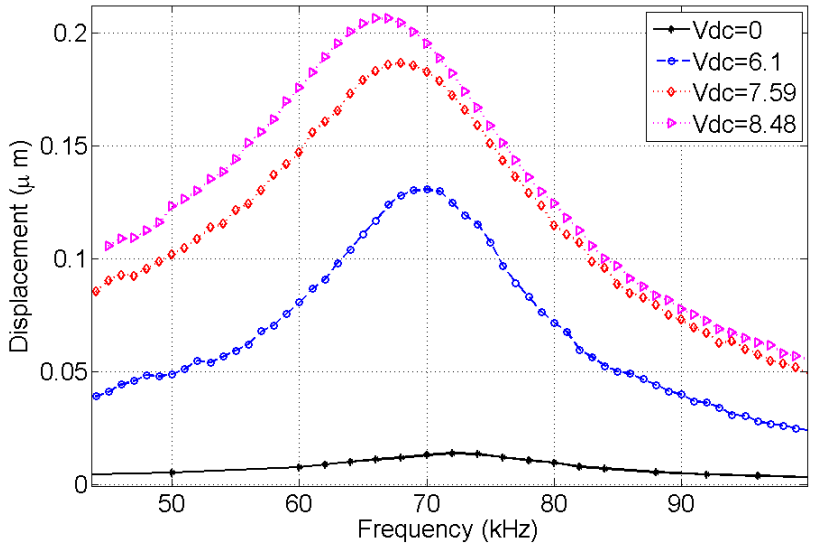


Figure 4.12: Compliance frequency response of a beam with dimensions of $175 \times 10 \times 2 \mu\text{m}$ and a capacitor gap of $2 \mu\text{m}$ where AC voltage is 1.30-1.4 V.

Parameter identification was also conducted for the $125 \mu\text{m}$ long beams. The peak nat-

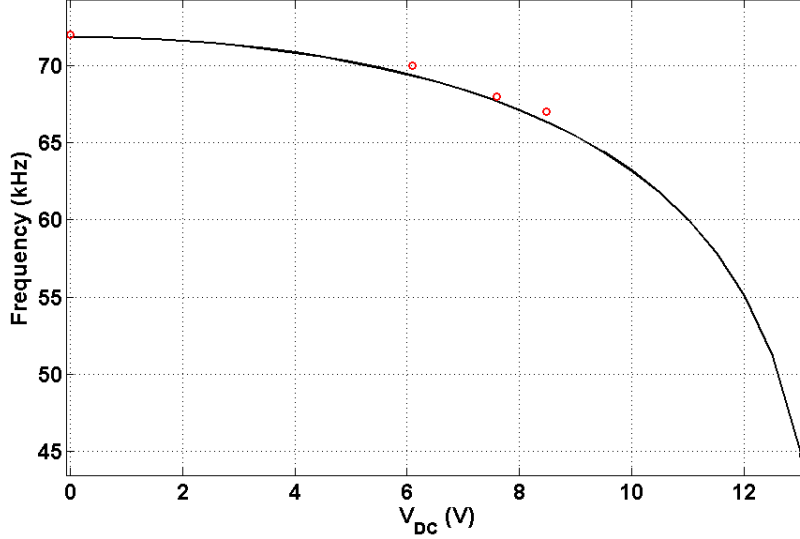


Figure 4.13: Natural frequency as a function of DC voltage for the beam with dimensions of $L = 185 \mu\text{m}$, $b = 10 \mu\text{m}$, $h = 1.9 \mu\text{m}$, and $d = 1.9 \mu\text{m}$:— Simulations, \circ experimental results.

atural frequency is plotted versus DC voltage in Figure 4.14. The beam was also tested by applying DC voltages and recording the beam tip displacement under an optical profilometer. The static deflection of the beam is illustrated in Figure 4.15, which confirms that the pull in voltage is around 25 V as predicted from the eigenvalue-problem simulations in Figure 4.14. Although the beams in these two figure have different width, they have the same pull-in voltage. This can be explained from the static equation of the beam (Eq. (3.42)), where the only parameter that is a function of beam dimensions is

$$\alpha = \frac{\varepsilon_0 b L^4}{2 E I d^3}. \quad (4.5)$$

In the above equation, the beam width b can be canceled out for rectangular cross sections with area moment of inertia $I = \frac{bh^3}{12}$, and hence the static profile is independent of the beam width. From the open loop frequency response, the beam dimensions are identified as $L = 125.6 \mu\text{m}$, $h = 1.9 \mu\text{m}$, with a gap of $d = 1.8 \mu\text{m}$ and the widths are $b = 10 \mu\text{m}$, and $b = 19 \mu\text{m}$ respectively in Figures 4.14 and 4.15. The damping ratio was calculated to be 0.053. The identified parameters from the open loop experiments are used in the closed-loop system model to validate the simulation results.

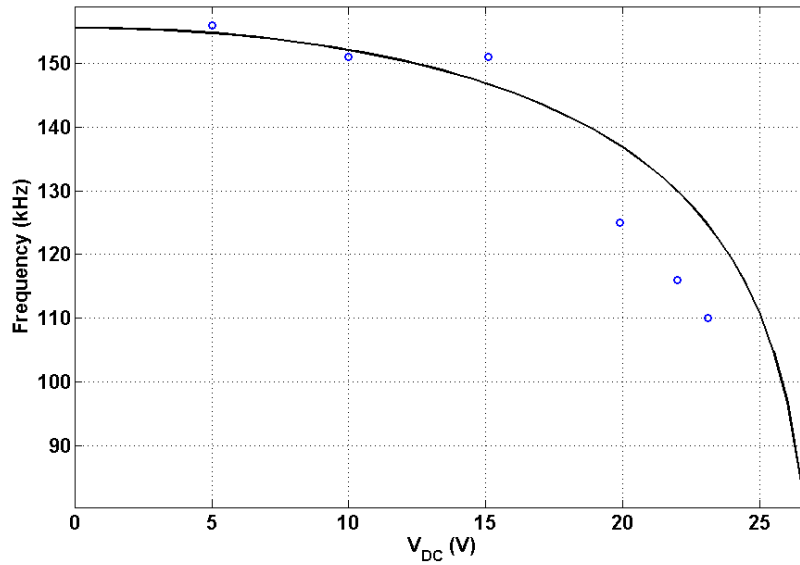


Figure 4.14: Natural frequency versus DC voltage beam for the with dimensions of $125.6 \times 10 \times 1.9 \mu\text{m}$ with a gap of $1.8 \mu\text{m}$ where AC voltage is 1.7-1.76 V. \circ : experimental results, $-$: simulations.

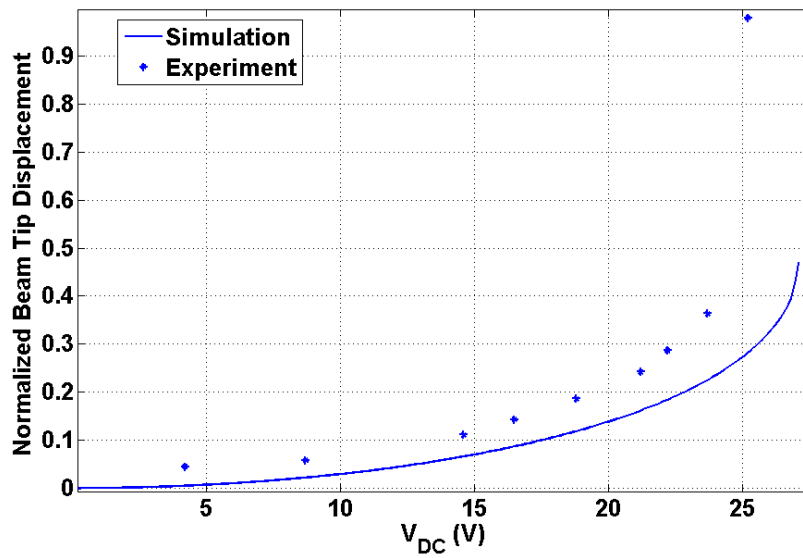


Figure 4.15: Static response for a beam with the dimensions of $125.6 \times 19 \times 1.9 \mu\text{m}$ with a gap of $1.8 \mu\text{m}$.

4.2 Closed Loop Actuator

4.2.1 Closed loop Experimental Set-up

A schematic of the feedback control system and the experimental configuration are illustrated in Figures 4.16 and 4.1, respectively. The closed loop system is implemented by adding a circuit that acts as a voltage regulator. The voltage regulator input was provided by a signal function generator, and the regulator op-amps were operated using two power supplies. The intermediate parameters were measured along the circuit and were displayed on the oscilloscope.

First, the beam tip velocity is measured with the vibrometer, the corresponding signal of which is passed through a high pass filter to eliminate a noise signal at 30 Hz generated by the vacuum pump used to hold the chip in place. Next, the filtered velocity signal is integrated in the circuit to find the displacement. The displacement signal is then used in the analog circuit to generate the control voltage V_c which is subtracted from the input voltage V_{in} , and the result is finally multiplied by G to generate the regulated voltage $G(V_{in} - V_c)$. The regulated voltage is applied to the actuator. It can either control the beam position to the stable regime to create a stable large-stroke actuator or drive the beam into nonlinear oscillations in the bi-stable regime, depending on the desired purpose.

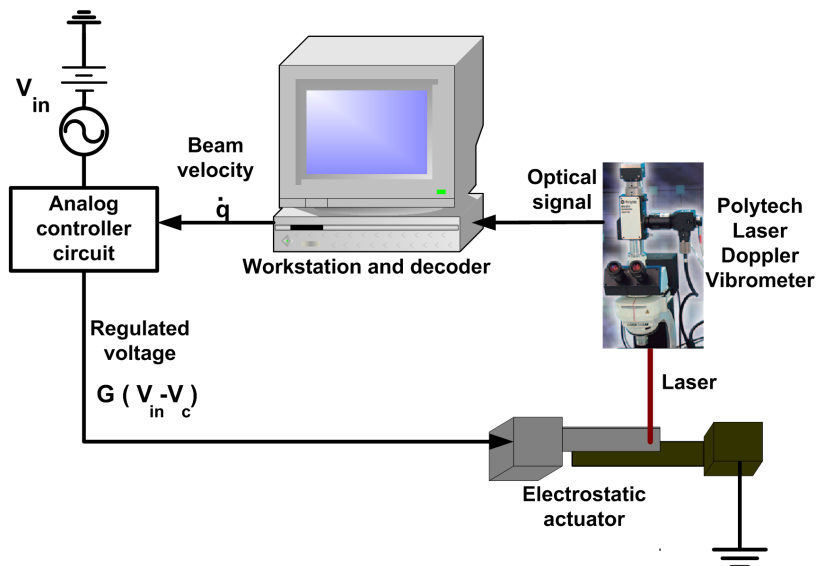


Figure 4.16: Schematic of the feedback control system

4.2.2 Large-Stroke Actuator

The voltage regulator is first tested for studying the stable system behavior. The stable actuator is obtained by setting the voltage regulator parameters to obtain a single stable equilibrium point over the gap distance as shown in Figure 4.17. In this figure, the solid line shows the location of the stable equilibrium point and the dashed line shows the location of the unstable saddle point.

The actuator is tested using a sinusoidal excitation signal designed to obtain a typical trajectory for read-write heads. The waveform varies sinusoidally between zero and a maximum voltage that corresponds to a desired static location in Figure 4.17. That means for the input voltages $V_{DC} = V_{AC}$. The simulation results in this figure were obtained by numerically solving the algebraic equation obtained by setting the time derivatives in Equation 3.45 to zero. The static profile reveals that the controller moves the saddle away from the stable equilibrium point as it is clear compared to the open loop system in Figure 3.3. The increased distance of the saddle from the stable equilibrium point enables the large stable operation of the actuator. The stable actuator operation from an undeflected position to a desired location is sought statically in applications such as AFM based memory devices to read and write the data or in programmable optical filters. In these applications, resonant and high frequency oscillations are not advantageous. Henceforth, choosing an excitation frequency around one fourteenth of the resonant frequency, large stable actuations are investigated quasi-statically.

Restricting the tests to low frequency allows for simplification of the control circuit. The controller Equation (3.45) can be rewritten in the Laplace domain as

$$sV_c = -rV_c + r\Psi\frac{q}{1-q} \quad (4.6)$$

and after rearranging it becomes

$$\frac{V_c}{\Psi\frac{q}{1-q}} = \frac{1}{1 + \frac{s}{r}} \quad (4.7)$$

The righthand side of Equation (4.7) is a low pass filter with a nondimensional cut off frequency of $\Omega = r$. When operating at much lower frequencies such that $\Omega \ll r$, in Eq. (4.7), the ratio $\frac{s}{r}$ approaches zero and thus it can be safely assumed that

$$V_c \approx \Psi\frac{q}{1-q} \quad (4.8)$$

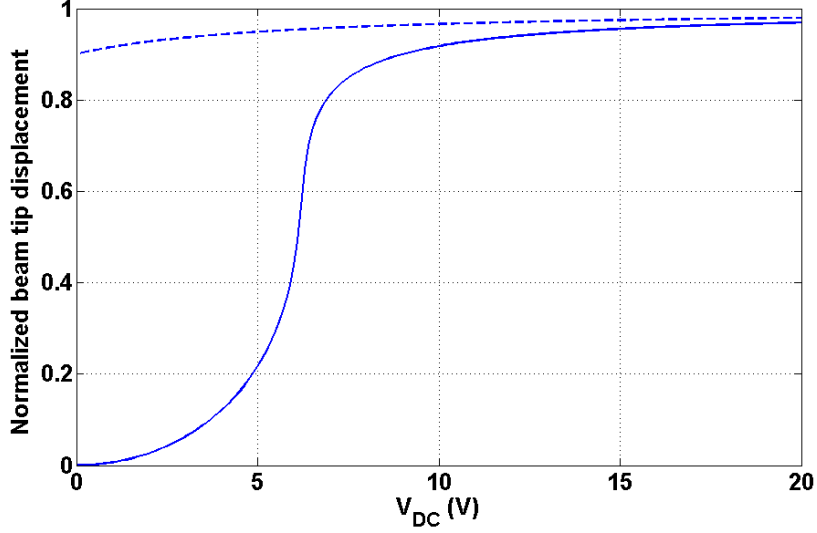


Figure 4.17: Closed loop displacement simulated response. Dashed line shows the location of unstable equilibrium points, the solid line shows the stable equilibrium location. (Beam dimension are $131 \times 20 \times 1.9 \mu\text{m}$, gap of $1.9 \mu\text{m}$, and controller parameters are $\Psi = 0.5 \text{ V}$, $G = 4.8$.)

Using the previous equation to generate the control voltage simplifies the implementation of the controller and allows for a more compact device. The revised system equations are then obtained:

$$\begin{cases} (\ddot{q} + \mu\dot{q} + \omega_1^2 q)(1 + c_1 q + c_2 q^2) = c_3 \alpha G^2 (V_{in} - V_c)^2 \\ V_c = \frac{q}{1 - q} \Psi \end{cases} \quad (4.9)$$

The controller function, the second of Equations (4.9), was implemented using analog electronics [71]. Despite the advantages of digital control such as easy code changes, an analog system is chosen because of its fast response. A challenge with analog systems though, is the difficulty in changing the controller function.

The block diagram of the controller is shown in Figure 4.18. In this figure, the voltage signal corresponding to the beam tip velocity \dot{q} measured by the vibrometer is integrated to find the displacement q . The displacement signal is scaled so that the entire electrostatic gap is equivalent to 1 V. Next, the displacement signal is subtracted from a constant voltage of 1 to evaluate $(1 - q)$, and division is performed to find $\frac{q}{1 - q}$. The result is multiplied

by the displacement gain Ψ to find the control voltage V_c . The final voltage $G(V_{in} - V_c)$ applied to the beam is then obtained after the subtraction of the control voltage from the input voltage V_{in} multiplying by the voltage gain G .

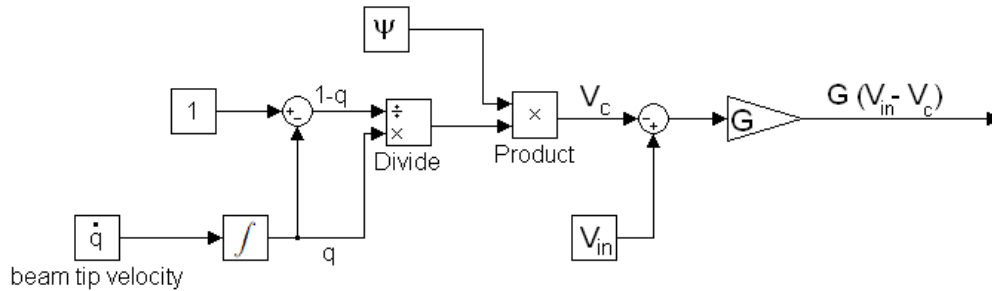


Figure 4.18: Block diagram of the low frequency controller.

The subtraction and multiplication are implemented using op-amps and the division is realized using the logarithmic characteristic of diodes. The schematic of the control circuit is shown in Figure 4.19. The locations of the input and output voltages, and parameters obtained at different points on the circuit, are indicated as well as some operational highlights of the circuit. The highlights, shown by dashed lines, include a high pass filter, an integrator, input amplifier, and voltage dividers. The high pass filter was added to the circuit to remove noise at 30 Hz produced by the vacuum pump used to hold the probes and the MEMS chip in place. The voltage dividers were also added to remove the DC shift in the input of the integrator caused by circuit imperfections and noise [71]. A picture of the realized circuit is presented in Figure 4.20.

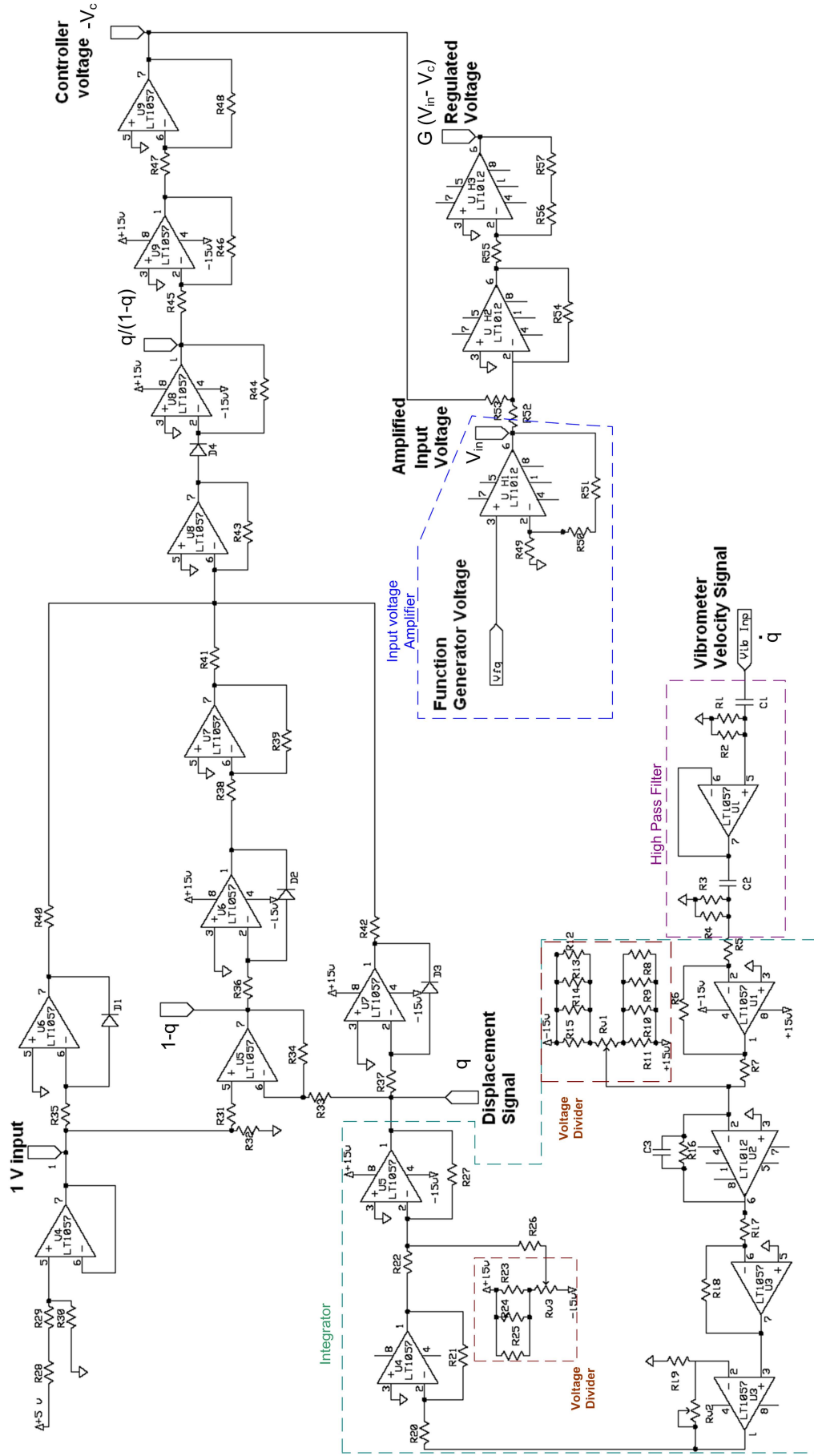


Figure 4.19: Schematic of the low frequency control circuit [8].

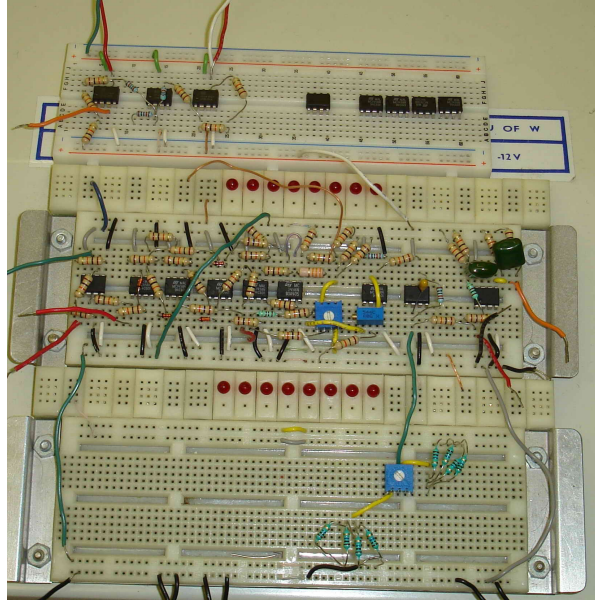


Figure 4.20: Picture of the low frequency control circuit.

The closed loop actuator was tested using a sinusoidal excitation voltage varying from zero to a maximum, according to $V_{in} = v(1 + \cos(\Omega t))$, corresponding to a target location. The maximum excitation of $2v$ corresponds to the horizontal axis of Figure 4.17, and the target location to the vertical axis. Figures 4.21 to 4.26 compare experimental and simulated dynamic responses revealing quasi-static actuation ranges up to 37%, 54%, 52%, 67%, 78% and 90% of the gap, respectively. Simulations were performed by numerically solving Eq. (4.9) using the beam parameters and the damping ratio identified in section 4.1.4. The frequency of excitation was 10 kHz, and compared to the beam natural frequency of 140 kHz, the motion was quasi-static. The damping ratio was 0.157, the pull-in voltage was 25 V, the beam length was 131 μm , the width was 20 μm , and the thickness was 1.9 μm . The gap was determined by matching the simulations to experimental results in the experiments. The capacitor gap was identified as $d = 1.82\mu\text{m}$, 1.75 μm , and 1.9 μm for the beams employed in the tests shown in Figures 4.21, 4.22, and 4.23-4.26, respectively. The first two figures are obtained using two beams on two different days, and the last four figures are obtained from testing a different beam on another day.

Figures 4.21 – 4.26 compare the simulation and experimental results. Experimental results in Part (a) of the figures presents the velocity measured by the vibrometer multiplied

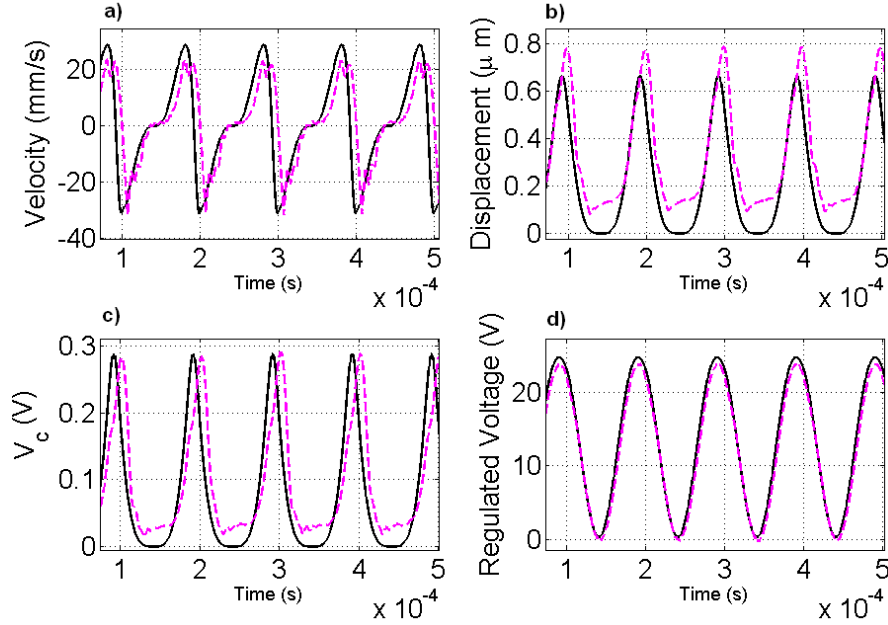


Figure 4.21: Closed-loop response to an excitation of $v = 2.7 \text{ V}$, $\omega = 10 \text{ kHz}$. $---$ measured, $-$ simulated. a) beam tip velocity, b) beam tip displacement up to 37%, c) controller voltage V_c , d) Regulated voltage $G(V_{in} - V_c)$. (Beam dimension are $131 \times 20 \times 1.9 \text{ } \mu\text{m}$, the gap is $1.82 \text{ } \mu\text{m}$, and the controller parameters are $\Psi = 0.5 \text{ V}$, $G = 4.8$.)

by a negative in the circuit as the direction of the assumed velocity was the reverse of the measured one, part (b) in these figures represents the displacement found from the integration of the velocity signal in the circuit, part (c) shows the measured controller voltage V_c , and part (d) illustrates the voltage applied to the actuator $G(V_{in} - V_c)$. Experimental results in part (a) and part (b) of the figures are filtered in MATLAB by local regression using weighted linear least squares and a 1st degree polynomial model that assigns lower weight to outliers in the regression. The method assigns zero weight to data outside six mean absolute deviations and had the span of 13% of the total data.

Good agreement between simulation and measured responses is observed for a broad range of actuation voltage. The smallest range is presented in Figure 4.21, where though the controller voltage does not exceed 0.3 V and the regulated voltage does not go beyond the open loop pull-in voltage of 25 V, the actuator traverses a trajectory that brings it to $0.67 \text{ } \mu\text{m}$ or 37% of the gap which is greater than the 33% limit for open loop systems. The results

shown in Figure 4.22 are for a beam of similar dimensions and the same excitation voltage as in Figure 4.21, but with a capacitor gap of $1.75 \mu\text{m}$ which is smaller than the $1.82 \mu\text{m}$ gap in Figure 4.21. As a result, the actuation increases from 37% to 54% or $0.95 \mu\text{m}$. The low signal to noise ratio for small displacements prevents the controlled motions from tracking the trajectory predicted by the troughs. However, as the displacement increases and the signal to noise ratio improves, the controller follows the desired trajectory well.

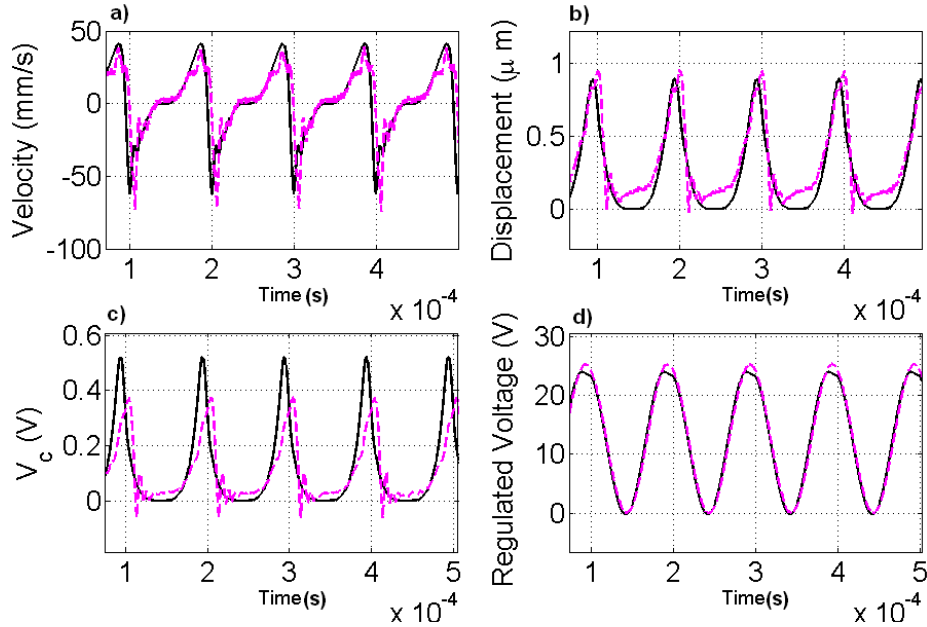


Figure 4.22: Closed-loop control response to excitation at $v = 2.69 \text{ V}$, $\omega = 10 \text{ kHz}$. $---$ measured, $-$ simulated: a) beam tip velocity, b) beam tip displacement up to 54%, c) controller voltage V_c , d) regulated voltage $G(V_{in} - V_c)$. (Beam dimension are $131 \times 20 \times 1.9 \mu\text{m}$, the gap is $1.75 \mu\text{m}$, and controller parameters are $\Psi = 0.5 \text{ V}$, $G = 4.8$.)

Keeping the excitation frequency constant at 10 kHz and increasing the peak voltage from 2.88 V to 3.2 V for a beam with a larger gap of $1.9 \mu\text{m}$, the travel ranges increase from 52% ($0.94 \mu\text{m}$) to 90% ($1.73 \mu\text{m}$) in Figures 4.23 to 4.26. This increase corresponds to a controller voltage rise from 0.45 V to 2.2 V as shown in part (c) of these figures and to the changes in the regulated voltage shape in part (d). The qualitative change in the regulated voltage originates from the increase of controller voltage V_c in sub-figure (c) as the beam displacement reaches its maximum in sub-figure (b). Because the controller voltage peak and the input voltage peak have the same phase, there is a voltage drop at

the peak of the regulated voltage across the capacitor $G(V_{in} - V_c)$ shown in Figure 4.26 (d). The voltage drop at the peak of the regulated voltage plays an important role in controlling the actuator. As the actuation voltage increases in the open loop actuator, the electrostatic force increases causing more deflection in the beam which rapidly increases the electrostatic force even more until the 30% deflection point where the pull-in normally occurs. The voltage regulator, on the other hand, drops the voltage and the electrostatic force as the displacement increases helping to balance with the mechanical spring force and making the large displacement feasible. At the maximum displacement, the actuator stops and its velocity reverses direction in sub-figure (a) as the mechanical force dominates the electrostatic force and the beam returns to the undeflected position. It is noted that the signal to noise ratio weakens in sub-figure (b) as the input voltage increases, though that affects the oscillation that takes place around the undeflected position and not around the large actuation points.

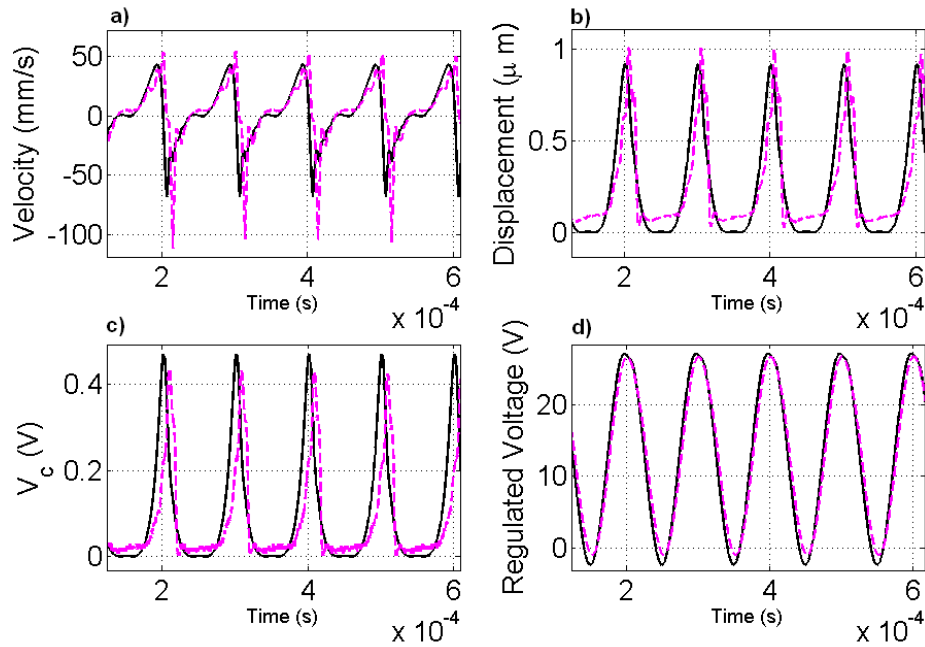


Figure 4.23: Closed loop response to excitation at $v = 2.88 V, \omega = 10kHz$. $---$ measured, $-$ simulated: a) beam tip velocity, b) beam tip displacement up to 52%, c) controller voltage V_c , d) regulated voltage $G(V_{in} - V_c)$. (Beam dimension are $131 \times 20 \times 1.9 \mu m$, the gap is $1.9 \mu m$, and controller parameters are $\Psi = 0.5 V, G = 4.8$.)

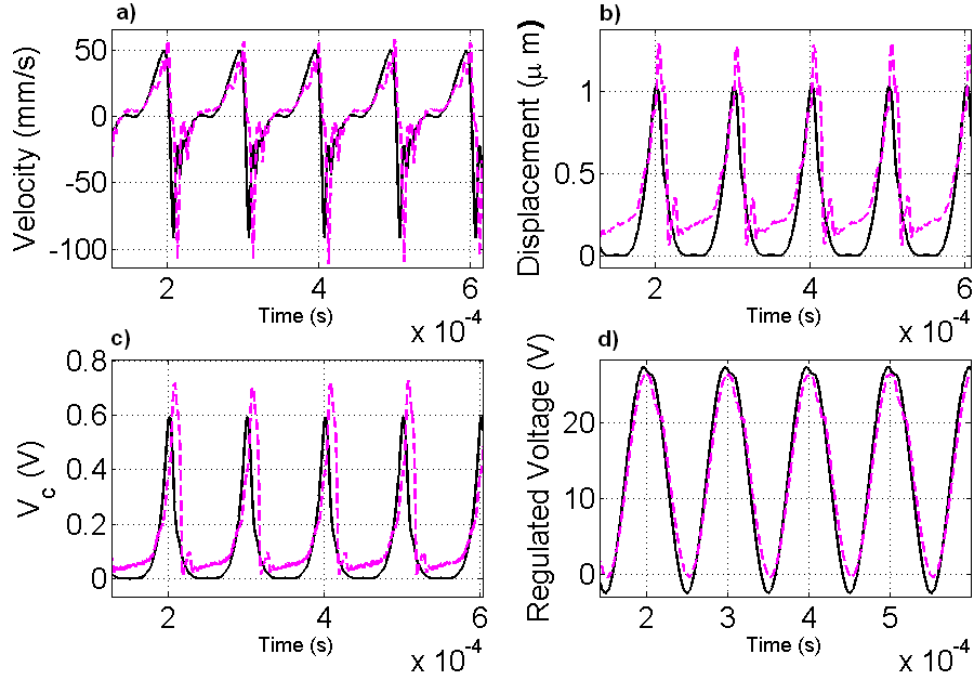


Figure 4.24: Closed loop response to excitation at $v = 2.92 \text{ V}$, $\omega = 10 \text{ kHz}$. $---$ measured, $-$ simulated. a) beam tip velocity, b) beam tip displacement up to 67%, c) controller voltage V_c , d) Regulated voltage $G(V_{in} - V_c)$. (Beam dimension are $131 \times 20 \times 1.9 \text{ } \mu\text{m}$, the gap is $1.9 \text{ } \mu\text{m}$, and controller parameters are $\Psi = 0.5 \text{ V}$, $G = 4.8$.)

The beam tip comes to within 400 nm and 100 nm of the substrate surface for the trajectories shown in Figures 4.25 and 4.26, respectively. This proximity is desirable for reading and writing in probe based high capacity data storage devices [9] using miniaturized AFM arrays.

Observing the displacement profiles, it is observed that more oscillations appear as the actuator reverses its direction of motion away from the higher peaks. These oscillations modulate the displacement and velocity profiles with oscillations at the natural frequency of the beam ω_1 . They occur because of the sudden motion reversal at the peak. On the other hand, the oscillations are not present at the counter motion reversal in the trough because of our choice of input signal which guaranties a trough wide enough for the initial oscillations to die out and a gradual motion reversal. The modulated oscillations are not seen in the predicted path as the model uses a linear viscous damping term to represent

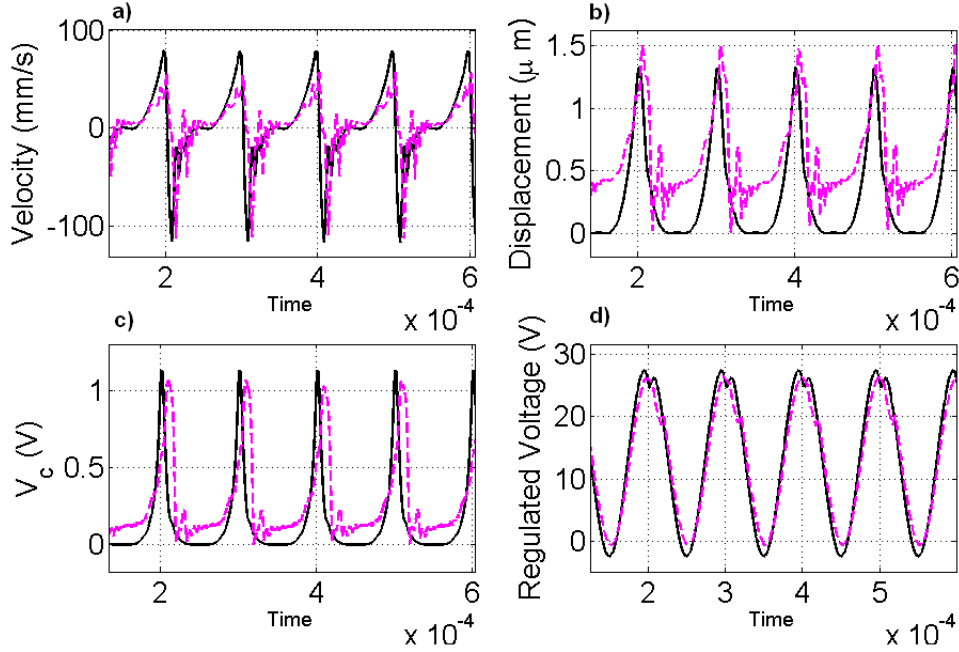


Figure 4.25: Closed loop response to excitation at $v = 3 \text{ V}$, $\omega = 10 \text{ kHz}$. $---$ measured, $-$ simulated. a) beam tip velocity, b) beam tip displacement up to 78%, c) controller voltage V_c , d) regulated voltage $G(V_{in} - V_c)$. (Beam dimension are $131 \times 20 \times 1.9 \mu\text{m}$, the gap is $1.9 \mu\text{m}$, and controller parameters are $\Psi = 0.5 \text{ V}$, $G = 4.8$.)

the dissipation mechanisms in the actuator. In averaging out the highly nonlinear effects of squeeze-film damping, it overestimates the amount of damping present for the small oscillations in the trough around the undeflected position. The same nonlinear damping effect is clear in the simulated velocity matching the minimum negative velocities but not the maximum positive velocities in Figures 4.25 and 4.26. This difference in the simulated and measured velocity results grows as the actuation range increases. These limitations notwithstanding, the actuator reaches its target at the peak with minimal delay. Further, unlike the leveraged bending method, the regulated voltages are around 27 V at the largest slightly larger than the pull-in voltage of 25 V.

As is seen in Figures 4.25(d) and 4.26(d), at the peak voltage drop there exists a small phase difference between the simulations and experiments that is caused by the internal delay of the op-amps in the controller circuit. This phase shift might be minimized using

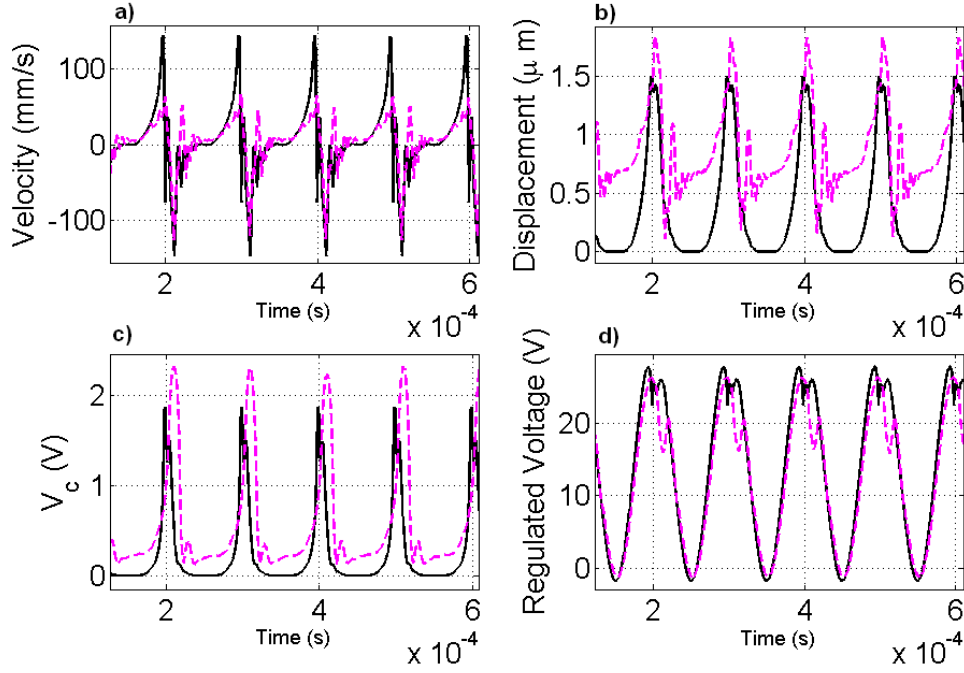


Figure 4.26: Closed loop response to excitation at $v = 3.2 \text{ V}$, $\omega = 10 \text{ kHz}$. $---$ measured, $-$ simulated: a) beam tip velocity, b) beam tip displacement up to 90%, c) controller voltage V_c , d) regulated voltage $G(V_{in} - V_c)$. (Beam dimension are $131 \times 20 \times 1.9 \text{ } \mu\text{m}$, the gap is $1.9 \text{ } \mu\text{m}$, and controller parameters are $\Psi = 0.5 \text{ V}$, $G = 4.8$.)

more precise non-inverting op-amps. However, the large actuation ranges are not affected by the small controller phase delay.

The ultimate positions reached at different peak voltages are summarized in Figure 4.27 as well as the static deflection derived setting the time derivatives in Equation (4.9) to zero and numerically solving the resulting algebraic system. Figure 4.27 reveals a good agreement between the static simulation results and the quasi-static experimental measurements, thereby justifying the basic assumption underlying the simplified controller development.

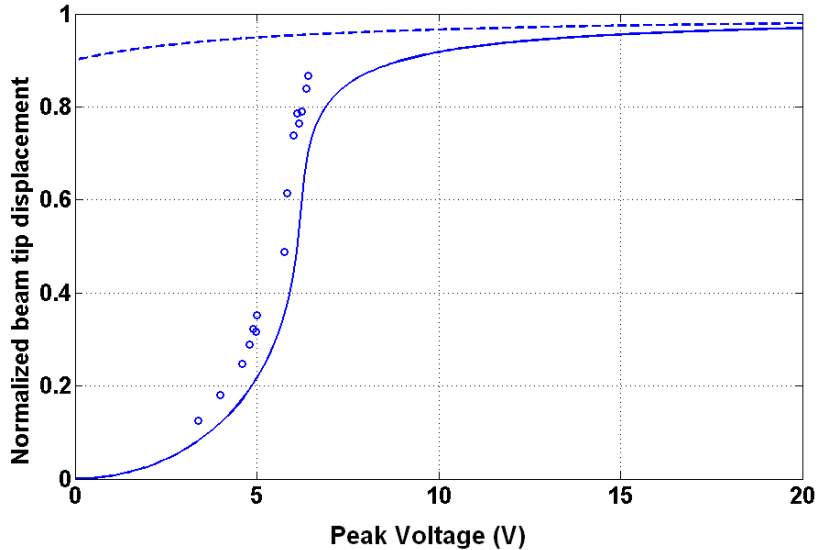


Figure 4.27: Peak actuator displacement versus peak voltage ($2v$). $--$ simulated unstable equilibrium points, $-$ simulated stable equilibrium points, \circ experimental results. (Beam dimension are $131 \times 20 \times 1.9 \mu\text{m}$, gap of $1.9 \mu\text{m}$, and controller parameters are $\Psi = 0.5 \text{ V}$, $G = 4.8$.)

4.3 Virtual regulator

Examining the response of the actuator to the controlled voltage, we postulated that applying the regulated voltage waveform obtained from the simulation directly to the beam without using the analog regulator could lead to similar results. The experimental setup consisted exclusively of the micro-beam, a signal generator, and a vibrometer to measure the beam tip velocity and an analog integrator. Simulations were performed using the closed loop control model to generate the customized voltage signal. The signal generator was then used to produce the customized waveform, the beam velocity response was measured using the vibrometer and the velocity was integrated using the analog integrator to find the beam displacement. The results are depicted in Figure 4.28, where the customized voltage signal is shown in part (c). Exciting the beam with the proposed waveform not only eliminates the need for the external feedback circuit but also allows an actuation range as large as 75% of the gap, which is significantly larger than the traditional open loop limit of 33% of the gap.

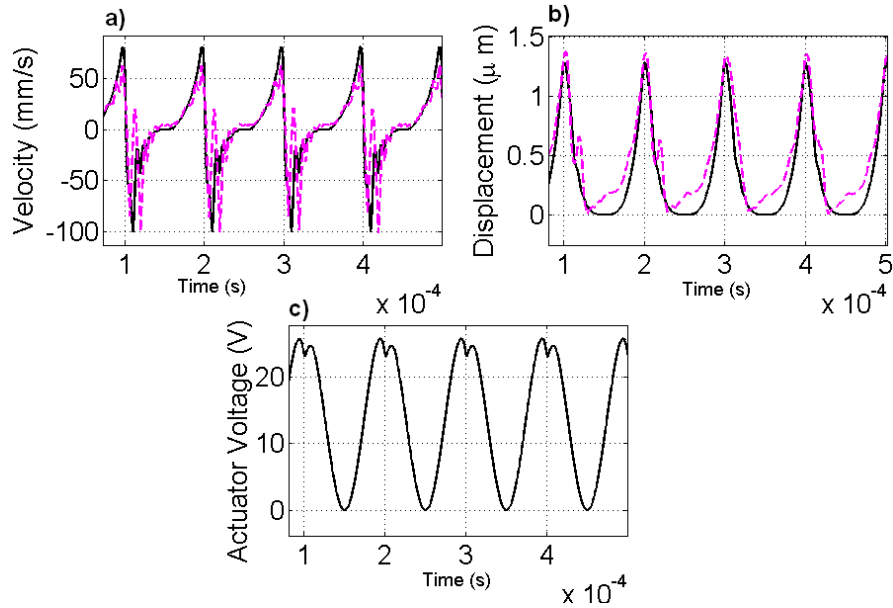


Figure 4.28: Beam open loop response to a modified input waveform: a) Beam tip velocity b) Beam tip displacement c) Actuator input voltage. $--$ measured, $-$ simulated response to excitation at $v = 3\text{ V}$, $\omega = 10\text{ kHz}$ for a beam with dimensions of $131 \times 20 \times 1.9\ \mu\text{m}$ with the gap of $1.82\ \mu\text{m}$, and controller simulated parameters of $\Psi = 0.5\text{ V}$, $G = 4.8$.)

The low frequency controller was also used to study the superharmonic resonances of the actuator.

4.4 Superharmonic Resonances

During testing of the closed loop low frequency actuator, superharmonic resonances were detected as predicted in Chapter 3. The results are shown in Figures 4.29 to 4.31. Part (a) represents the beam tip velocity measured by the vibrometer and multiplied by a negative in the circuit, part (b) displays the beam tip displacement integrated from the velocity signal in the analog circuit. Part (c) is the FFT of 2^{12} velocity data points obtained after the experiment was done using MATLAB, and part (d) is the phase portrait obtained from plotting the measured velocity versus the integrated displacement. The beam under test has the nominal dimensions of $175 \times 10 \times 2$ with a gap of $2\ \mu\text{m}$ and the natural frequency

of 80 kHz . All experiments were conducted on the same day. Superharmonic resonances are verified by the FFT sub-figure (c), where a train of FFT peaks extending from the excitation frequency to the natural frequency peak exists and the number of peaks reveal the order of superharmonic resonance. The superharmonic resonances of order 8, 6, and 5 are reported at excitation frequencies of 10, 13, and 15.7 kHz respectively with the same voltage excitation magnitudes. The superharmonic orbits shown in part (d) of the figures expand along the displacement and velocity axes as the frequency increases and the order of superharmonic drops. As it is noted the maximum displacement recorded at the maximum frequency of 15.7 kHz is as large as 60% of the gap in Figure 4.31 (b). The stretch along the displacement axis also corresponds to higher dynamic amplification of the input and less noise due to larger signal to noise ratio.

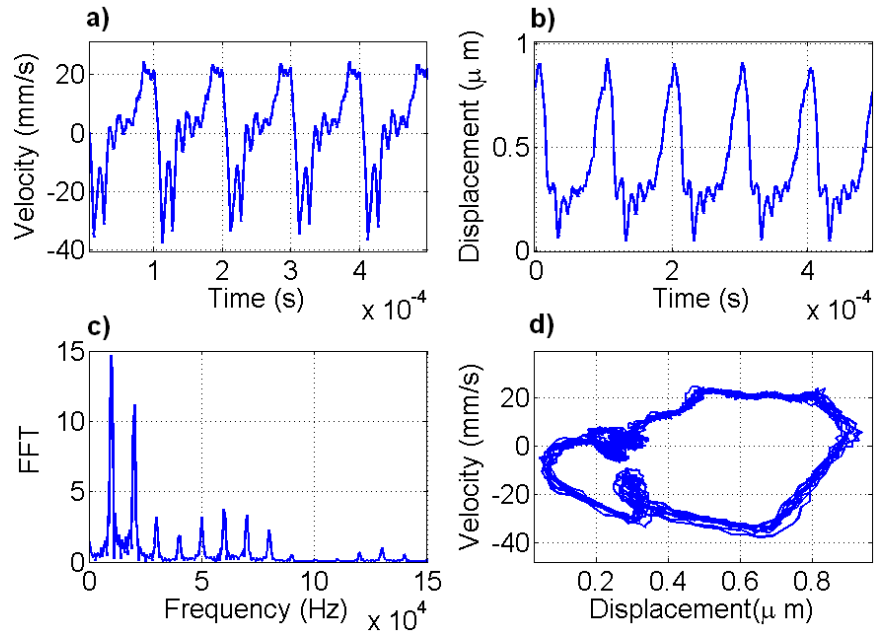


Figure 4.29: The superharmonic resonance of order 8 obtained when the controller parameters are $G = 2$, $\Psi = 0.5\text{ V}$, and the excitation is $v = 3.56\text{ V}$, $\omega = 10\text{ kHz}$. a) beam tip velocity, b) beam tip displacement, c)Fast Fourier Transform of the tip velocity, d) Phase portrait.

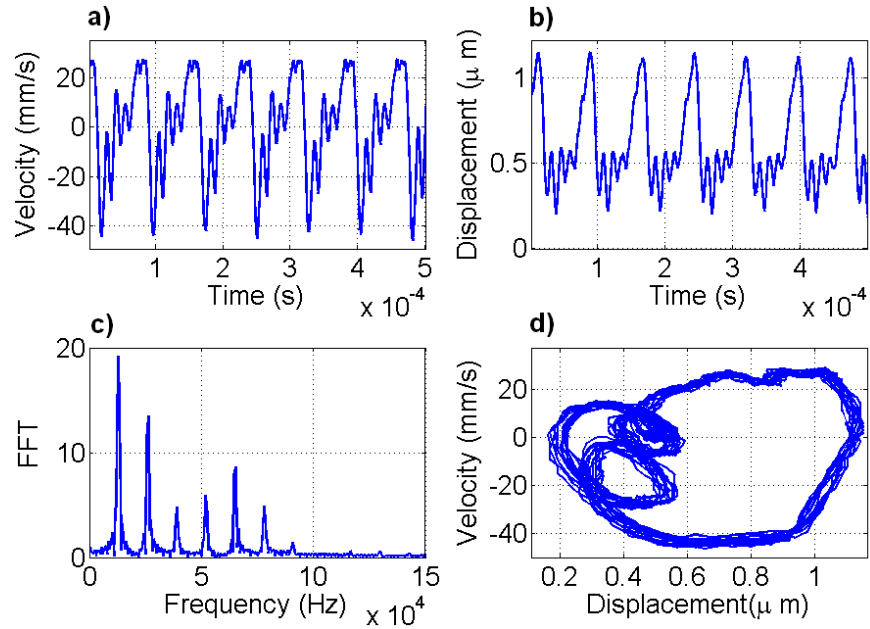


Figure 4.30: The superharmonic resonance of order 6 obtained when the controller parameters are $G = 2$, $\Psi = 0.5$ V, and the excitation is $v = 3.56$ V, $\omega = 13$ kHz. a) beam tip velocity, b) beam tip displacement, c) Fast Fourier Transform of the tip velocity, d) Phase portrait.

Testing a similar beam with a different natural frequency of 85 kHz, the superharmonic resonance of order 4 was observed as shown in Figure 4.32 at an excitation frequency of 21.36 kHz. Although the excitation voltage is lower than the previous set of tests, the evolution of the phase portrait is comparable with the previous three cases of superharmonic resonance. In Figure 4.29, there exists three loops, two of them merge and expand as the frequency increases in Figure 4.31, and finally the two twists unite in superharmonic of order 4 in Figure 4.32.

The superharmonic resonances recorded constitute, to the best of our knowledge, the first instance of this nonlinear resonance being observed and analyzed in MEMS electrostatic actuators. Exciting the system at one frequency, the system is responding at multiple frequencies. The route to chaos is changing the frequency with smaller increments close to one of the superharmonic resonances, which was not possible for us. The frequency was also limited to 22 kHz because beyond this frequency the attenuation caused by the op-amps

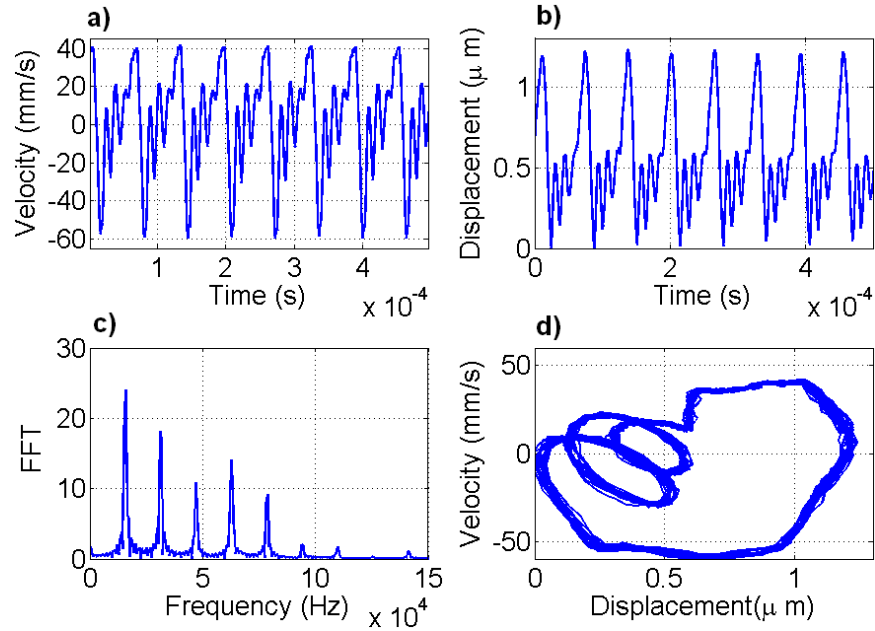


Figure 4.31: The superharmonic resonance of order 5 obtained when the controller parameters are $G = 2$, $\Psi = 0.5$ V, and the excitation is $v = 3.55$ V, $\omega = 15.7$ kHz. a) beam tip velocity, b) beam tip displacement, c) Fast Fourier Transform of the tip velocity, d) Phase portrait.

and diodes was significant. The attenuations are because of the bandwidth gain product defined in the op-amp data sheets. Therefore, we were limited in the operation frequency range. Future work can include using op-amps with a larger frequency bandwidth.

Superharmonic resonance was also observed in the open loop system for excitation at integer fractions of the natural frequency. The beam had the nominal dimensions of $175 \times 10 \times 2$ and a gap of $2 \mu\text{m}$ with a natural frequency of 80 kHz. The test was conducted using the internal function generator of the vibrometer. The DC voltage was held constant at 5 V. The FFT of the velocity responses was recorded by the PSV software of the vibrometer. Superharmonic resonances of order 6 to 3 in descending order are depicted in parts (a) to (d) of Figure 4.33. The orders of the superharmonics are clear from the number of pronounced peaks in the FFT including the natural frequency peak at 80 kHz. The presence of the peak at the fractions of the natural frequency and peak at the natural frequency are indicative of the superharmonic resonance.

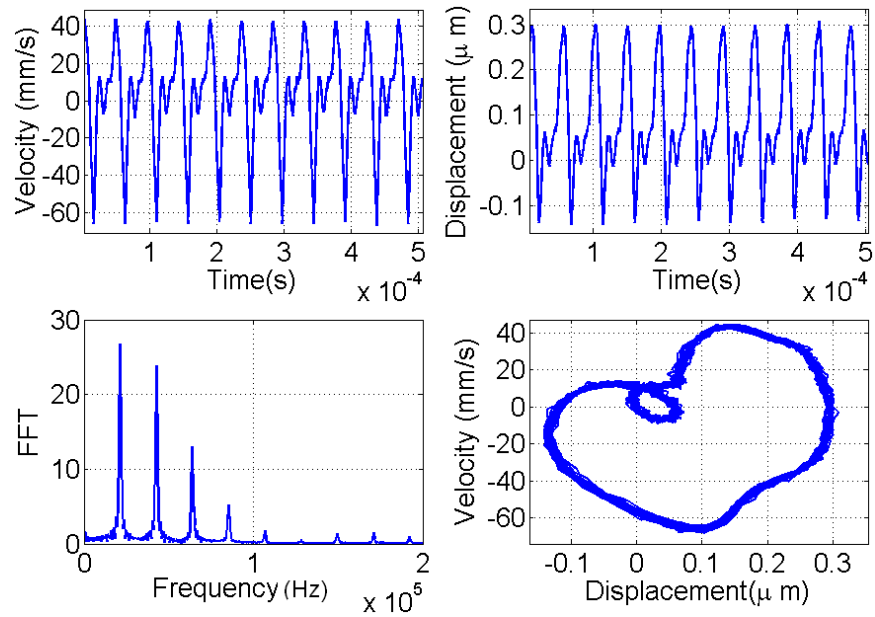


Figure 4.32: The superharmonic resonance of order 4 obtained when the controller parameters are $G = 2$, $\Psi = 0.5 V$, and the excitation is $v = 2.78 V$, $\omega = 21.36 kHz$. a) beam tip velocity, b) beam tip displacement, c) Fast Fourier Transform of the tip velocity, d) Phase portrait.

Although the superharmonic resonance in the open loop is beneficial as less equipment is needed to produce the resonance, the superharmonics of the closed loop system could be preferred as the FFT peaks appeared for each frequency are more noticeable and comparable in magnitude indicating the larger kinetic energy that can be detected more effectively.

Superharmonic resonances of the implemented closed loop actuator did not lead to chaos as the electronic components were not designed to support frequencies beyond 22 kHz. Using electronic components that can support higher frequencies without attenuation and generators that have small frequency resolution enables developing the chaotic micro-resonator from the modified closed loop actuator. The application of the chaotic resonator can be in secure communication devices [56], where sending and receiving a signal in a broad range of frequencies rather than a single frequency are desirable.

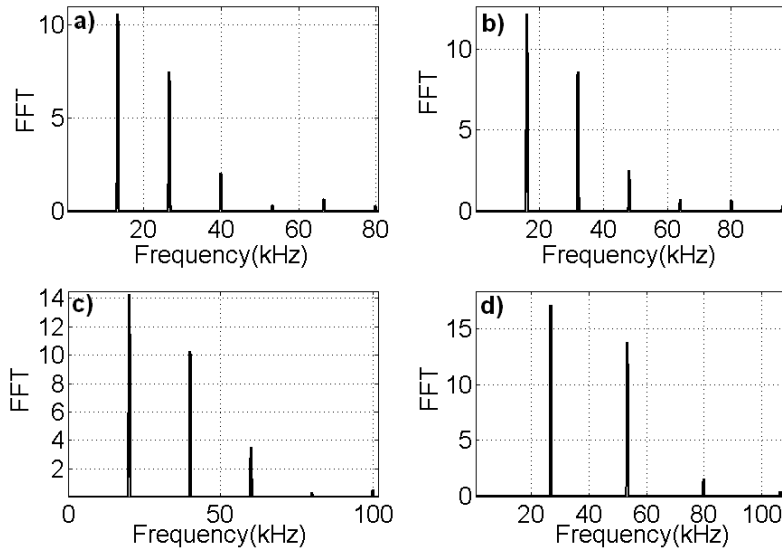


Figure 4.33: The superharmonic resonances of an actuator with the nominal dimensions of $175 \times 10 \times 2 \mu\text{m}$ and a gap of $2 \mu\text{m}$ a) order 6 obtained at $V_{DC} = 5.2 \text{ V}$, $V_{AC} = 4.7 \text{ V}$, $\Omega = 13.3 \text{ kHz}$, b) order 5 obtained at $V_{DC} = 5.2 \text{ V}$, $V_{AC} = 4.16 \text{ V}$, $\Omega = 16 \text{ kHz}$, c) order 4 obtained at $V_{DC} = 5.2 \text{ V}$, $V_{AC} = 3.88 \text{ V}$, $\Omega = 20 \text{ kHz}$, d) order 3 obtained at $V_{DC} = 5.2 \text{ V}$, $V_{AC} = 3.32 \text{ V}$, $\Omega = 26.6 \text{ kHz}$.

4.5 Summary

In this chapter, the large stroke actuator developed from adding a controller to the open loop actuator in Chapter 3 was implemented. The actuator model parameters were identified from open loop experiments and the simulations were validated by experimental results. The controller was modified for the low frequency test to command the actuator to a higher position quasi-statically. Stroke actuation as large as 90% of the gap was achieved by decreasing the electrostatic force, and thus balancing it with the mechanical restoring force as the moving electrode approaches the fixed electrode.

Likewise, the travel range of the open loop actuator was increased using a customized waveform input. The micro-beam actuator is excited with a waveform generated using a model of the closed loop system. Exciting the beam with the proposed waveform not only eliminates the need for any external feedback system but also allows actuation as large as 75% of the gap. It should be emphasized that both regulators do not impose further

requirements and can operate in open air under environmental disturbances. Further, for practical deployment of the actuator, the vibrometer can be replaced by a piezoresistor to sense the beam position and the actuator placed with the analog controller on a CMOS chip.

Superharmonic resonances were also reported for the first time both for open loop and closed loop electrostatic actuators. Chaotic oscillations exist within very fine tolerances of the excitation frequency for superharmonic resonances. Hence, the superharmonic resonances are important observation as they could lead to chaos by modifying electronic components of the circuit to support higher frequency oscillations and by using function generators with smaller frequency resolution.

Chapter 5

Quadratic Resonator Model

Investigating the behavior of the voltage regulator for the chaotic resonator developed in Chapter 3, a new regulator function is derived to improve the performance of the chaotic resonator [74]. Not only the voltage requirement of the proposed actuator is much less than the previous one, but also the controller is more robust. Derivation of the new regulator function and its static and dynamic analysis follow.

5.1 New Regulator Function

The governing static equation for the previously used controller is Eq. 3.49 for one-mode approximation. This equation describes the balance of the mechanical force and the electrostatic force using the regulated voltage. The left hand side of the equation is the spring force multiplied by the denominator of the electrostatic force and the right hand side is the square of the difference of the input voltage and the regulated voltage. The equation can be solved graphically by plotting both sides of the equation as functions of q_1 , Figure 5.1. Three intersections occur in the domain $q_1 \leq 1$ representing three equilibrium points, two of which are stable nodes and one is an unstable saddle. The two stable equilibrium points create the two-well potential field that was used to create chaos. The same goal can be achieved using a different controller function as long as they produce three intersections or more.

Using a simple quadratic function as a voltage regulator instead of a hyperbola, we

found four intersections (equilibrium points) as depicted in Figure 5.2. The equilibrium equation for the new actuator can be written using one-mode approximation as

$$\omega_1^2 q_1 (1 + c_1 q_1 + c_2 q_1^2) = c_3 \alpha G^2 (V_{in} - (n_0 + n_1 q_1 + n_2 q_1^2))^2 \quad (5.1)$$

where n_0, n_1, n_2 are the coefficients of the quadratic function. The equilibrium points obtained using the quadratic controller include two stable and two unstable equilibrium points. The static equilibrium points at different applied voltages are derived in section 5.3. In terms of implementation, the proposed quadratic controller circuit will have lower noise as the singularity present in the previous controller as the beam approaches the bottom electrode is eliminated in this design.

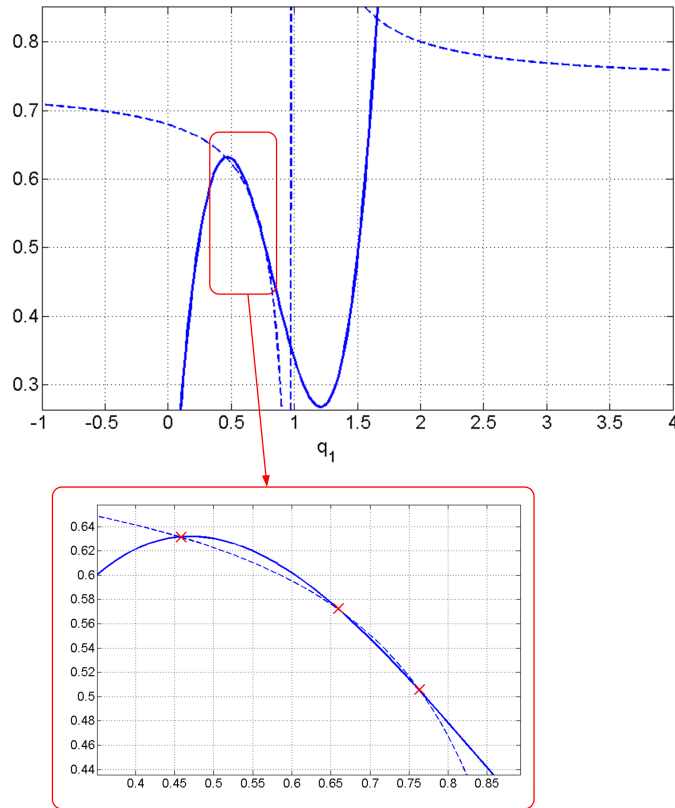


Figure 5.1: Graphical solution of Eq. 3.49 showing the balance of mechanical force and the regulated electrostatic force and a zoom at $V_{in} = 140.5 V$ for actuator parameters: Beam dimensions $200 \times 80 \times 4.5 \mu m$ and a gap of $3 \mu m$, controller gains $\Psi = 6 V$, $G = 0.65$, Modulus of Elasticity $E = 166 GPa$, Density $\rho = 2331 \frac{kg}{m^3}$. — left side of the equation, -- right side of the equation

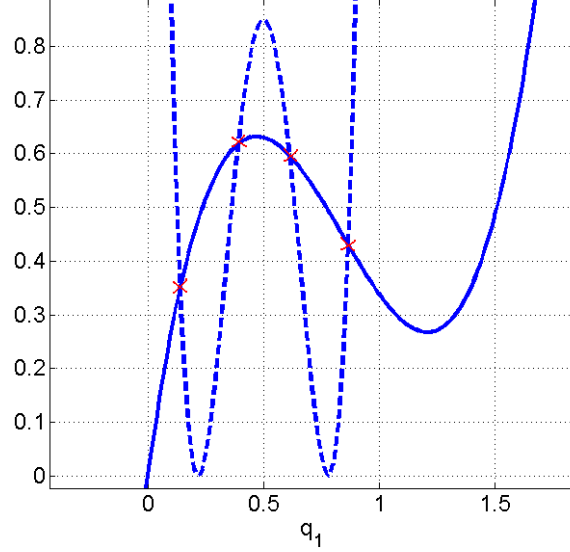


Figure 5.2: Graphical solution of Eq. 5.1 showing the balance of the mechanical force and the regulated electrostatic force at $V_{in} = 15 V$ for actuator parameters: Beam dimensions $200 \times 80 \times 4.5 \mu m$ and a gap of $3 \mu m$, quadratic function coefficients $n_0 = -205.2 V$, $n_1 = 1291.4 V$, $n_2 = -1293.6 V$, Modulus of Elasticity $E = 166 GPa$, Density $\rho = 2331 \frac{kg}{m^3}$. – left side of the equation, -- right side of the equation.

5.2 Actuator Model

The configuration of the electrostatic actuator system is the same as that shown in Figure 4.16 comprising of a cantilever beam above a fixed electrode and a voltage regulator. The normalized partial differential equation of motion of the actuator (Eq.3.43) is rewritten as

$$\ddot{w}(1-w)^2 + w^{(4)}(1-w)^2 + \mu\dot{w}(1-w)^2 = \alpha(V_{in} - V_c)^2 \quad (5.2)$$

where all parameters are defined in section 3.1, and the controller voltage V_c rate of change function is composed of a quadratic function of the normalized beam tip deflection $w(1)$ and an integrator with a constant gain K_I :

$$\dot{V}_c = -K_I \left(V_c - \frac{a_0 + a_1 w(1) + a_2 w^2(1)}{\sqrt{\alpha}} \right) \quad (5.3)$$

where a_0 , a_1 , a_2 are constant coefficients chosen to obtain four equilibrium points such that the first and last equilibrium points are as close as possible to the beam and the fixed

electrode, respectively. The rationale for this choice will be explained in section 5.4.1. To obtain the static and dynamic responses of the actuator, the partial differential equation of motion Eq. (5.2), is converted to an ordinary differential equation using separation of variables and Galerkin's method using one mode shape of the beam as described in section 3.1. For the one-mode case, $w(1) = q_1$. Two ordinary differential equations are thus obtained:

$$\begin{cases} (\ddot{q}_1 + \mu\dot{q}_1 + \omega_1^2 q_1)(1 + c_1 q_1 + c_2 q_1^2) = c_3 \alpha (V_{in} - V_c)^2 \\ \dot{V}_c = -K_I \left(V_c - \frac{a_0 + a_1 q_1 + a_2 q_1^2}{\sqrt{\alpha}} \right) \end{cases} \quad (5.4)$$

where ω_1 is the first natural frequency of the beam, and c_1 , c_2 , and c_3 are found from applying Galerkin's method. To implement the electronic circuit of the controller, the second equation is rewritten to include dimensional time:

$$\dot{V}_c = -\frac{K_I}{T} \left(V_c - \frac{a_0 + a_1 q_1 + a_2 q_1^2}{\sqrt{\alpha}} \right) \quad (5.5)$$

where the value of the integrator gain $\frac{K_I}{T}$ is given in Table 5.1. The coefficients in the above equation are chosen to be realizable in an electronic circuit and V_c has a maximum range of 35 V (-15 V to 20 V) as illustrated in Figure 5.3, which is 2.28 times less than the previous controller (Figure 3.27).

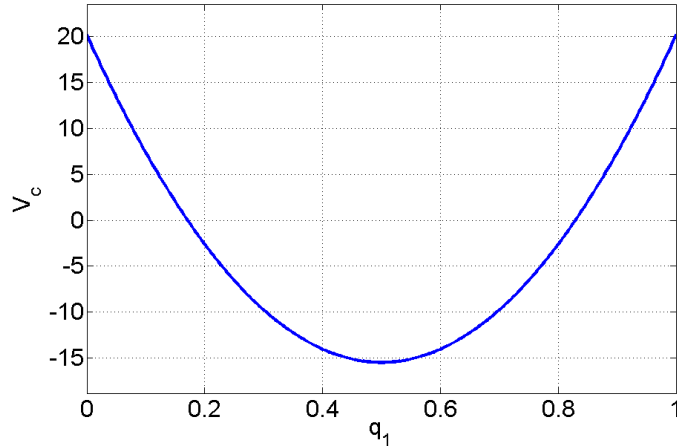


Figure 5.3: Controller output voltage V_c as a function of the nondimensional gap when controller coefficients are $\frac{a_0}{\sqrt{\alpha}} = 20.1939$ V, $\frac{a_1}{\sqrt{\alpha}} = 142.6973$ V, $\frac{a_2}{\sqrt{\alpha}} = 142.6973$ V.

The actuator parameters are identified experimentally. The natural frequency of the

cantilever beam has been found experimentally to be 99.38 kHz and the beam length was determined to be 157 μm . The other parameters are given in Table 5.1.

Table 5.1: Actuator parameters

Parameter	Symbol	Value
Density	ρ	2331 $\frac{\text{kg}}{\text{m}^3}$
Beam Length	L	157.4 μm
Beam Width	b	10 μm
Beam Thickness	h	1.9 μm
Initial Gap	d	1.9 μm
Nondimensional Damping Coefficient	μ	0.6153
Permittivity of Free Space	ε_0	8.85E-12 $\frac{\text{F}}{\text{m}}$
Modulus of Elasticity	E	150 GPa
Integrator Gain	K_I/T	0.1776 $\frac{1}{\text{s}}$

5.3 Static Analysis

To study the behavior of the actuator, the location of the equilibrium points and their stability conditions should be known. The location of the equilibrium points, the static response, is found from Eq. (5.4) by equating the time derivatives to zero and solving the resulting algebraic equation numerically for a given DC voltage. The stability of the points are found by linearizing Eq. (5.4) around the equilibrium points and finding the eigenvalues. The static response for the two new quadratic designs of the controller are illustrated in Figures 5.4 and 5.5 and the eigenvalues at $V_{in} = 2$ V in Figure 5.5 are listed in Table 5.2.

It can be concluded from Figure 5.5, and Table 5.2 that points 1 and 3 are stable equilibrium points and points 2 and 4 are saddles. In other words, the first and the third branches of the static profile are the loci of stable equilibrium points and the second and fourth branches are the loci of the saddles. The nondimensional natural frequency of the lower and upper equilibrium points (1 & 3) are 5.72 and 3.02 corresponding to 161.7 kHz and 85.37 kHz, respectively.

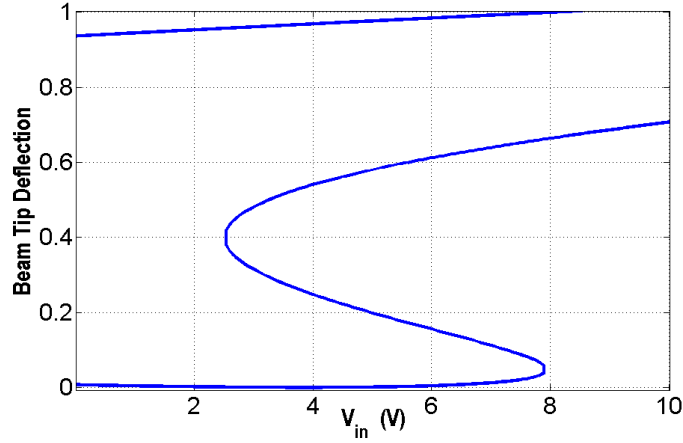


Figure 5.4: Nondimensional deflection of the beam tip versus input DC voltage when controller coefficients are $\frac{a_0}{\sqrt{\alpha}} = 3.8697 \text{ V}$, $\frac{a_1}{\sqrt{\alpha}} = -88.0195 \text{ V}$, $\frac{a_2}{\sqrt{\alpha}} = 104.78 \text{ V}$ (first design).

The bi-stability region for the first design is 5.3 V, which is about the same size as shown in Figure 3.11, but the bi-stability range for the second design in Figure 5.5 is as large as 20.95 V. The advantage of the quadratic controller design is also lower bi-stability operating voltages: 2.6 V to 7.9 V for the first design and 1.75 V to 22.7 V for the second design. The minimum operating DC voltages show significant reduction in comparison to the 110 V in Figure 3.11 and 18.5 V in Figure 3.28 reducing the demand on the electronic components in the regulator circuit. The two alternative designs are valuable with regard to different design objectives. The first design is suitable for limited input voltage less than

Table 5.2: Eigenvalues of the equilibrium points at $V_{in} = 2 \text{ V}$ using the second controller design

#	q_1	Eigenvalue 1	Eigenvalue 2
1	0.066	-0.308+5.72i	-0.308-5.72i
2	0.458	2.43	-3.04
3	0.555	-0.308+3.02i	-0.308-3.02i
4	0.962	15.89	-16.51

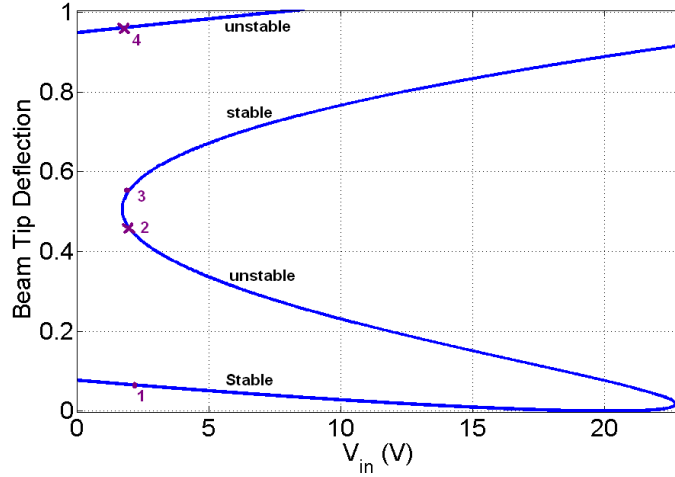


Figure 5.5: Nondimensional deflection of the beam tip versus input DC voltage when controller coefficients are $\frac{a_0}{\sqrt{\alpha}} = 20.1939 V$, $\frac{a_1}{\sqrt{\alpha}} = 142.6973 V$, $\frac{a_2}{\sqrt{\alpha}} = 142.6973 V$ (second design).

8 V. On the other hand, the second design is suitable for larger potential wells that can reach 90% of the gap.

The quadratic controller has also the advantage of tunability in terms of the size of the potential wells of the actuator. This property can be seen by comparing Figures 5.4 and 5.5. At low voltages, the upper equilibrium point is close to the lower saddle, while the lower equilibrium is far from the saddle indicating a larger lower well. As the voltage increases, this situation reverses and the upper well becomes larger than the lower well basin.

5.4 Dynamic Analysis

The steady-state dynamic response of the actuator to $V_{in} = V_{DC} + V_{AC} \cos \Omega t$ is found by solving Eq. (5.4) numerically for 5000 periods of excitation and retaining the last 128 periods. Bifurcation diagrams are also found revealing the excitation amplitude and frequency ranges where chaos occurs.

Exciting at the nondimensional frequency of 3.2, corresponding to 90.4 kHz, which is between the natural frequency of the two equilibrium points, chaos occurs at an AC

amplitude of $V_{AC} = 1$ V (Figure 5.6). Figure 5.6 shows that the motion develops in the lower well, then grows to exceed the potential hump (saddle) and cross to the upper well before suddenly coming back to the lower well to repeat the process. This behavior is intermittency route to chaos, which is different from the period doubling route to chaos found in Chapter 3. In this case, chaos appears subsequent to a subcritical period-doubling bifurcation. In the former case, chaos appears subsequent to a cascade of supercritical period-doubling bifurcations. The chaotic motion developed in this case is mostly in the lower well and between the two wells as the phase portrait and times series of the deflection show. Thus the effect of the second well is minimized. It is because the upper-well is shallow, that is the saddle and the second stable equilibrium are very close (Figure 5.5). The controller voltage is changing between 10 to 19 V and it is less than half of the voltage required by the previous controller for same ranges of oscillation in Figure 3.32.

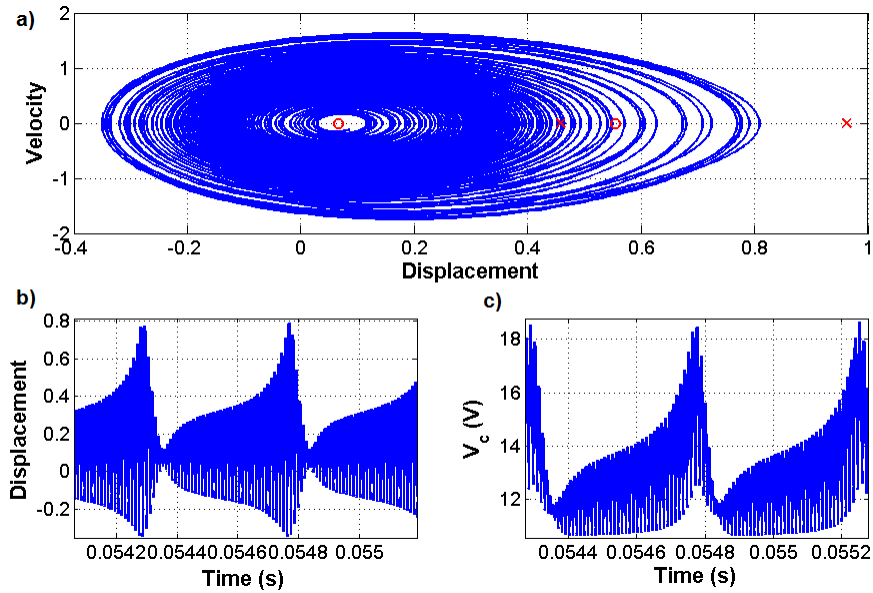


Figure 5.6: a) Phase portrait of chaotic oscillation , b) Nondimensional beam tip displacement, c) Controller output voltage V_c , for the second design and $\frac{K_I}{T} = 0.1776 \frac{1}{s}$, at $V_{DC} = 2$ V, $V_{AC} = 1$ V, $\Omega = 90.4$ kHz. (Crosses show the location of saddles and circles show the location of nodes.)

5.4.1 Force Sweep

Observing chaotic attractors mainly in the lower-well led us to seek chaotic attractors that are limited strictly to one well at small DC voltages. Therefore, the force sweeps are obtained at zero DC voltage keeping the excitation frequency constant.

A single stable equilibrium is available at $V_{DC} = 0$ located at 0.08 of the gap with a natural frequency of 164 kHz . Force sweeps, Figure 5.7, are obtained for excitation frequencies of $\Omega = 90.4 \text{ kHz}$, $\Omega = 91.8 \text{ kHz}$, $\Omega = 93.22 \text{ kHz}$, and $\Omega = 94.64 \text{ kHz}$. Eqs. (5.4) are solved numerically for 5000 periods of AC excitation and the last 128 periods are sampled at the period of excitation starting from the maximum displacement.

The bifurcation diagrams illustrate the progression from periodic motion to intermittent chaos. The intermittent chaos disappears beyond a voltage limit where the orbit grows and touches the unstable manifold of the saddle and pull-in happens. At the lowest frequency of $\Omega = 90.4 \text{ kHz}$, there is a hysteric jump in the amplitude before chaos occurs as the AC voltage increases. This frequency is close to the threshold frequency of 89.84 kHz for the appearance of chaos, below it, the chaotic motion vanishes.

The higher the frequency is, the larger is the threshold of AC voltage for the chaotic motions. The reason is that the kinetic energy is higher for larger frequencies making the potential energy and displacement smaller for a constant input energy. That means, orbits at higher frequencies require more voltage to become chaotic before approaching the manifold of the saddle and disappearing. Similarly, the chaotic orbit grows along the displacement axis as the frequency decreases, which is clear comparing the largest orbits at each frequency. In other words, chaotic orbits at higher frequencies expands along the velocity axis more, touches the unstable manifold sooner, thus expanding less along the displacement axis. The AC voltage range that produces chaotic motion also decreases at the largest shown frequency of $\Omega = 94.64 \text{ kHz}$ for the same reason. Therefore, it is concluded that operating at the threshold frequency is desirable to create a chaotic resonator with the largest chaotic displacement signal that makes signal detection easier.

The chaotic attractor with the widest footprint along the displacement axis is illustrated in Figure 5.8 at the frequency of 90.4 kHz and $V_{DC} = 0 \text{ V}$, $V_{AC} = 1 \text{ V}$. The displacement chaotic signal in part (b) shows vibrations up to 82% of the gap in the positive direction as well as 35% of the gap in the negative direction. Such large motions are possible by making the saddle very close to the fixed electrode, and making the stable equilibrium

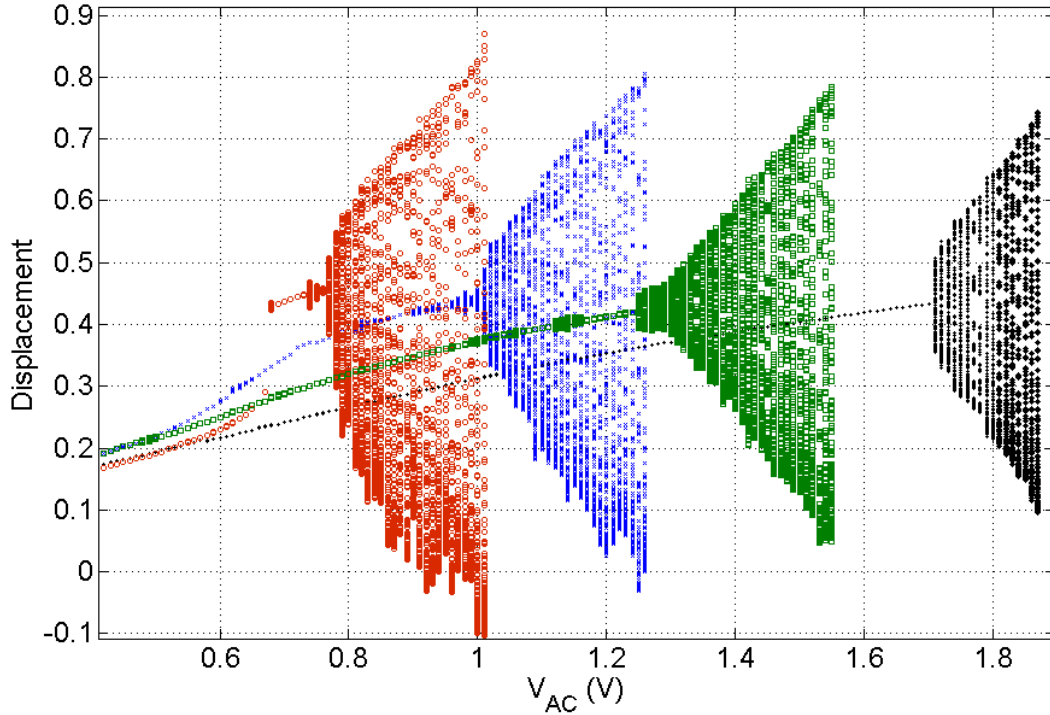


Figure 5.7: Bifurcation diagram constructed from a force sweep of V_{AC} at $V_{DC} = 0$ at four different fixed frequencies. \circ $\Omega = 90.4kHz$, \times $\Omega = 91.8kHz$, \square $\Omega = 93.22kHz$, and \cdot $\Omega = 94.64kHz$

close to the undeflected beam position (See Figure 5.5). It is also noted that even as the oscillations approach the electrode, the controller voltage shown in Figure 5.8 (c) is limited to the range 8 V to 17 V. Hence, the quadratic controller made the total displacement signals as large as 117% of the gap requiring the controller output voltage as small as 9 V, while using the previous controller, actuation was only feasible up to 90% of the gap with the price of controller voltage as large as 18 V (Figure 3.32). Lower controller voltages reduce the demand on the circuit components.

Furthermore, such large attractors of the quadratic controller could indicate the controller robustness as it shows the system survives the irregular but bounded chaotic oscillations covering almost a large area of phase space. The quadratic regulator can also control the attractor size and location by setting the DC voltage (Figure 5.4), the AC voltage and frequency (Figure 5.7).

In addition, the input voltage to the system for large chaotic attractors does not require any DC voltage, compared to 18.5 V DC (Figure 3.28) for the previous controller. Eliminating DC voltage prevents the leakage current into the isolation layers of the actuator and avoids drift of the measured parameter values over time. On the other hand, the lowest input AC voltage for large oscillations compared to the previous controller stays similar in the range of 0.78 V to 1.01 V.

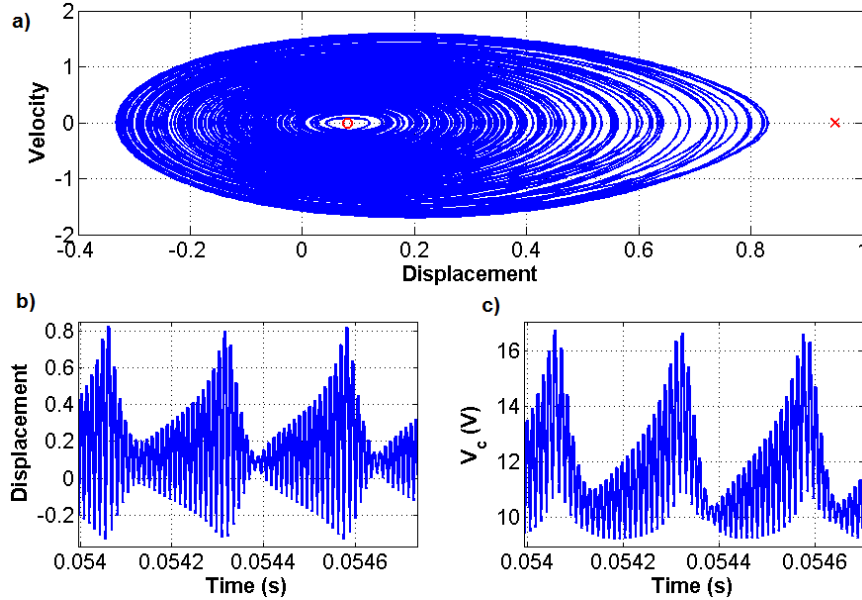


Figure 5.8: a) Phase portrait of chaotic oscillation , b) nondimensional beam tip deflection, c) controller output voltage V_c , for the second design and $\frac{K_I}{T} = 0.1776 \frac{1}{s}$, at $V_{DC} = 0$ V, $V_{AC} = 1$ V, and $\Omega = 90.4 kHz$. The cross shows the location of saddle and the circle shows the location of stable equilibrium point.

5.4.2 Frequency Sweep

The frequency response curves shown in Figures 5.9 and 5.10 are obtained by sweeping the frequency of excitation at two fixed AC voltages of $V_{AC} = 1.23$ V, and $V_{AC} = 1$ V, respectively. The results are obtained by solving Eqs. (5.4) numerically for 5000 periods of AC excitation and sampling the last 128 periods at the period of excitation starting from the maximum displacement. Decreasing the excitation frequency in the first case from 113

kHz, the displacement amplitude increases until chaos appears through an intermittency route at 93.51 kHz and continues down to 91.8 kHz. Below that, large motion disappears as the attractor orbit becomes very large, touches the unstable manifold of the saddle and goes to infinity (dynamic pull-in), in a process known as the escape from a potential well [20]. The escape region, where there is no solution, exists down to the frequency of 85.3 kHz, below which the system response continues to be periodic all the way down.

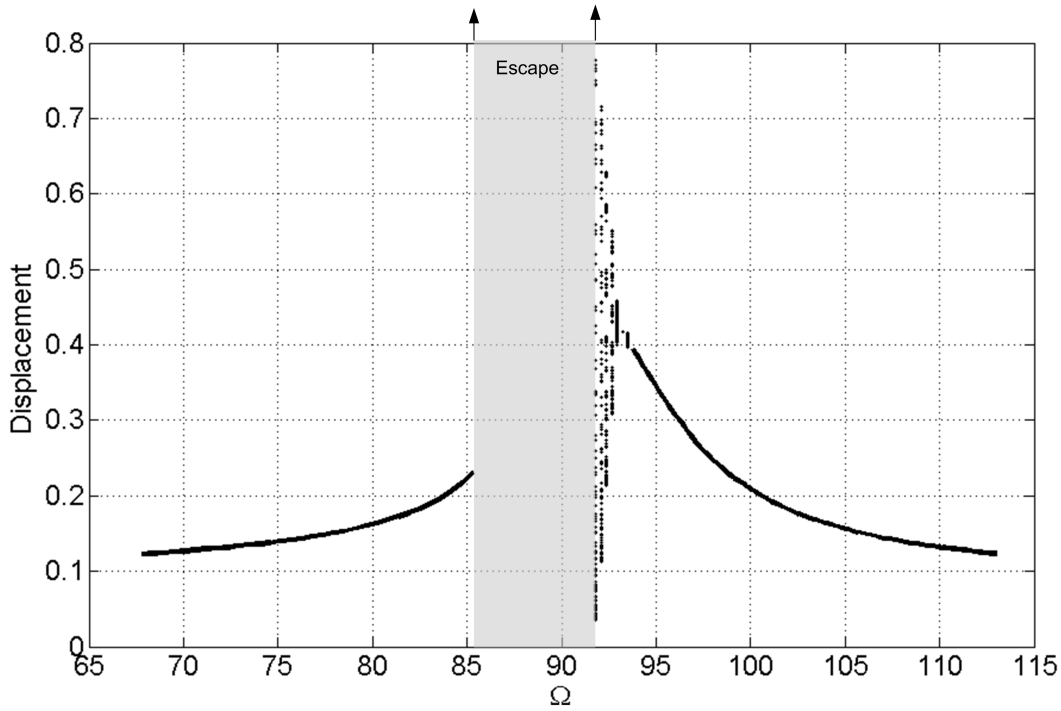


Figure 5.9: Bifurcation diagram constructed from a frequency sweep at $V_{AC} = 1.23$ V and $V_{DC} = 0$.

Both frequency sweeps reveal softening-type of response with a small chaotic region. Comparing the two bifurcation diagrams, the escape region shrinks, the threshold frequency for chaos drops, while the largest attractor grows for lower AC excitation. Lowering down the AC excitation voltage eventually eliminates the escape region and the chaotic region to be replaced by multi-valued periodic responses and hysteric jump observed in the force sweep. The largest chaotic attractors shown in Figures 5.9 and 5.10 correspond to the largest attractors in Figure 5.7 for frequencies of 91.8 kHz and 90.4 kHz, respectively.

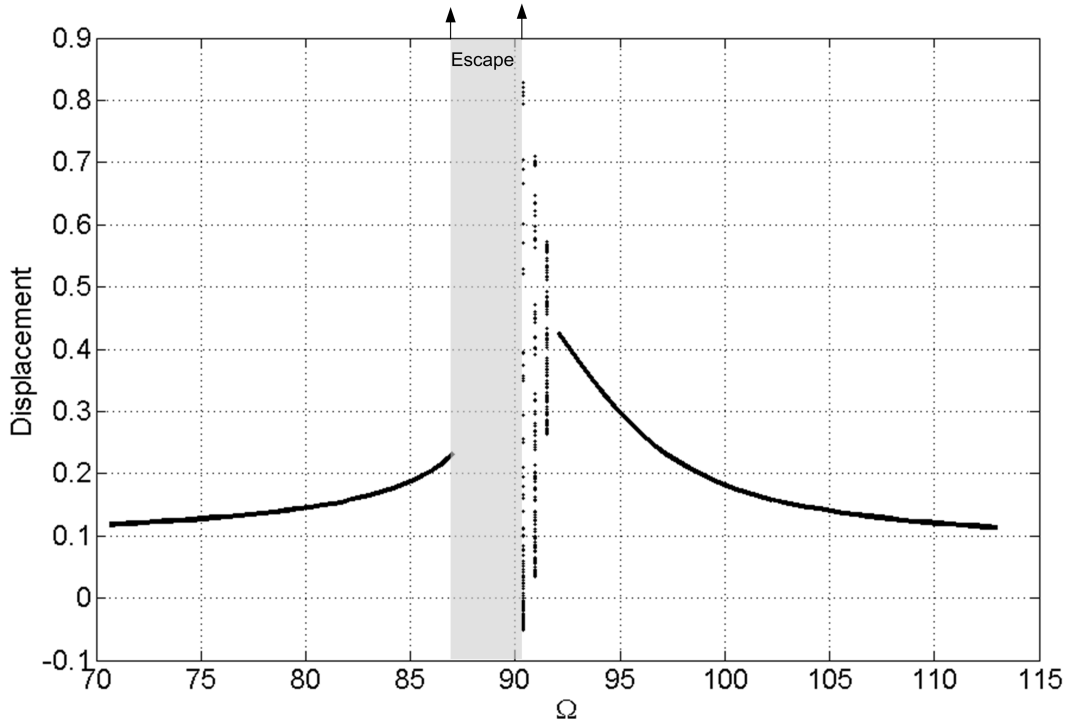


Figure 5.10: Bifurcation diagram constructed from a frequency sweep at $V_{AC} = 1$ V and $V_{DC} = 0$.

5.4.3 Information Entropy

Information entropy is used as a metric to verify the attractor in Figure 5.8. The size of a box containing the attractor is obtained and is divided to small cubes of size $\epsilon = 0.0002$. Then a Poincaré section of the attractor is found by sampling at the period of excitation starting from the maximum displacement. The number of points in each cube is counted (N_i) and divided by the total number of points on the Poincaré section (N_0) to get $P_i = \frac{N_i}{N_0}$. The information entropy is then calculated based on [75]:

$$I(\epsilon) = - \sum^N P_i \log P_i \quad (5.6)$$

where N is the total number of cubes. The system is fully predictable when all points are located in one cell and therefore $I = 0$. Any value between 0 and 1 is a measure of the unpredictability of a chaotic attractor.

The information entropy is obtained for the attractor of Figure 5.8 starting from different initial conditions in the phase space. The results are presented in Figure 5.11. In this figure, information entropies are between 0.732 and 0.737, which proves that the oscillations are chaotic. The figure also reveals that there is a common information entropy of 0.7324 for 23 out of 26 initial conditions with a small variation of less than 0.005 for the other three initial conditions.

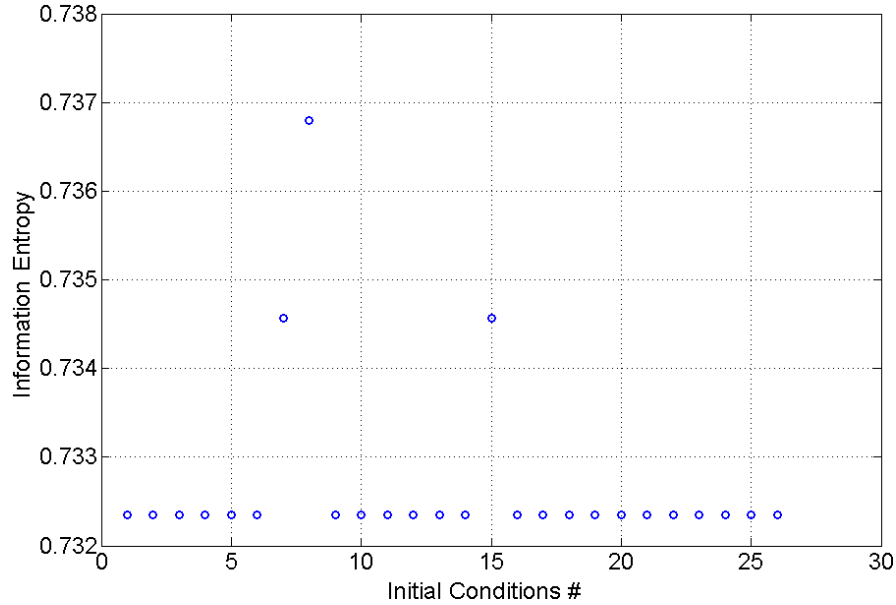


Figure 5.11: Information entropy for the chaotic attractor of the second design $\frac{K_I}{T} = 0.1776 \frac{1}{s}$ at $V_{DC} = 0$ V, $V_{AC} = 1$ V, and $\Omega = 90.4 kHz$. The initial conditions are q_0 at equal increments between $[0.28-0.66]$, \dot{q}_0 is constant at 0.1, and $V_{c0} = 0$ V.

Information entropy is also found for an attractor located at $V_{AC} = 1.8$ V in Figure 5.7 using the same initial conditions of Figure 5.11. The calculated information entropies are illustrated in Figure 5.12, which shows a common value of 0.732 for 23 out of 26 initial conditions and small variation for the other three initial conditions. The information entropy was also obtained for other attractors and it was observed that there was a dominant value of 0.732 for all attractors that does not depend on the excitation frequency or amplitude.

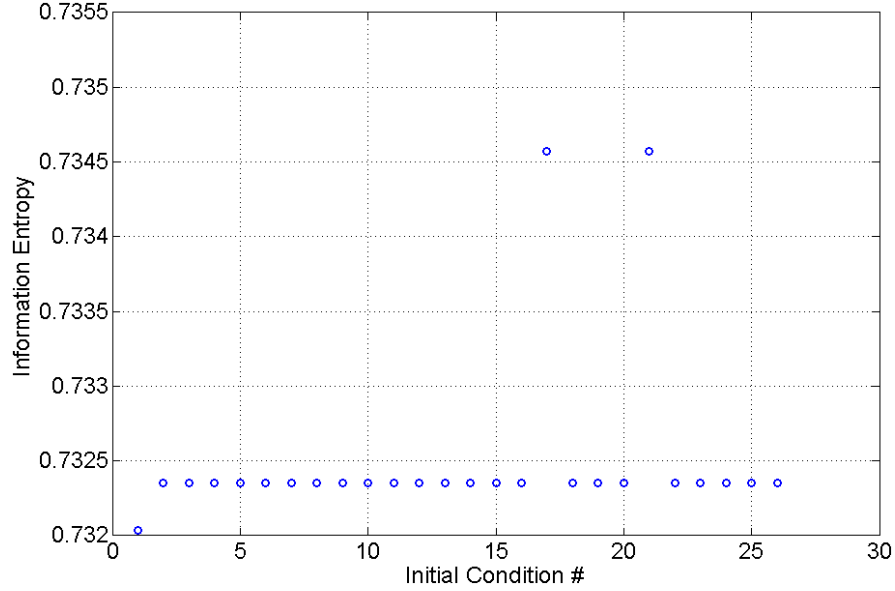


Figure 5.12: Information entropy for the chaotic attractor of the second design $\frac{K_I}{T} = 0.1776 \frac{1}{s}$ at $V_{DC} = 0$ V, $V_{AC} = 1.8$ V, and $\Omega = 94.64 kHz$. The initial conditions are q_0 at equal increments between $[0.28-0.66]$, \dot{q}_0 is constant at 0.1, and $V_{c0} = 0$ V.

5.5 Summary

In this chapter, a voltage regulator with a quadratic control function is developed for an electrostatic actuator to make a large stroke chaotic resonator. Bifurcation diagrams are obtained by sweeping the magnitude and frequency of excitation. The quadratic controller demonstrates valuable advantages over the previously studied controller. Not only the the quadratic regulator improves the system handling of noise, but also it requires no input DC voltage that avoids leakage current in the isolation layers of MEMS. The regulator drives the beam to vibrate in the positive and negative directions for a total range of 117% of the gap, extended from 90% in the previous case. It requires only half of the previous regulator output voltage, thus decreasing the load on the circuit components. The large oscillations of the quadratic resonator are important as they are bounded in the phase space, thus making detection easier which suitable for use in sensing applications. The size and location of the chaotic attractors are also controllable setting DC, AC magnitude and

frequency. Furthermore, the resonator is potentially robust as it demonstrates a stable response over a large area of the phase space.

Finally a metric of chaos, namely information entropy, is used to prove that the observed long period orbits are indeed chaotic and to measure their irregularity. It was found the chaotic attractors have a dominant information entropy of 0.732 that does not depend on the excitation frequency and magnitude and is a characteristic of the chaotic process in the quadratic resonator.

Chapter 6

Concluding Remarks

6.1 Thesis Contributions

Contributions of this thesis are summarized as follows:

1. Development of a nonlinear micro-resonator

A comprehensive study of the nonlinear behavior of a chaotic micro-cantilever resonator was presented using a previously introduced control law. The model of the micro-oscillator was improved from a lumped model to a multi degree of freedom model based on the mode shapes of the micro-cantilever resonator. The developed mathematical model was capable of complex dynamic analysis in seconds much faster than the commercial FEM tools more suitable for static analysis. The actuator can be configured as either a large-stroke actuator or a bi-stable actuator. The bi-stable actuator was used to create a chaotic resonator. The excitation voltage and frequency ranges where chaotic attractors appear were illustrated in bifurcation diagrams. A chaos metric, Lyapunov exponent, was used to the existence of chaos. The investigation of the nonlinear resonator revealed excitation frequency and voltage ranges for periodic, multiple period, one-well, and two-well chaos as well as superharmonic resonances. This study is valuable not only to avoid nonlinear responses in some applications, but also to benefit from the rich inherent nonlinear behavior of the micro-oscillator in developing the next generation of nonlinear mass detection sensors.

In addition, a new control law was introduced in this thesis for a chaotic micro-resonator that not only yielded robust and bounded large oscillations that could easily be detected, but also required less voltage that placed less demand on the electronic components of the regulator. These properties make the resonator suitable to use in different sensors. Further, the quadratic regulator circuit is expected to have less noise as the singularity in the previous control law is eliminated. The chaotic micro-resonator was created using one-well potential field and extended over 117% of the gap. The bifurcation diagram of the chaotic resonator revealed large areas of one-well chaotic oscillation from an intermittency for different frequencies of excitation.

2. Development of a large-stroke actuator

To achieve the large quasi-static actuation ranges required for applications such as AFM-based memory devices, the control law was simplified into low-frequency version. The low-frequency actuator was simulated, fabricated and tested using an electronic control circuit to regulate the voltage of a micro-cantilever resonator. The actuator parameters were determined experimentally. The actuation range of the electrostatic actuator was extended quasi-statically to 90% of the gap larger than the largest previously recorded travel range of 60%. The model used for simulations predicted the system responses with good accuracy. Using the input waveform generated from the closed loop simulation, the open loop actuation was also extended to 75% of the gap. The open loop actuator with the extended stable operation is attractive due to its minimal system requirements. These large-stroke actuators are advantageous in many applications such as optical filters, sensors, AFM surface metrology systems. The large-stroke actuator also showed superharmonic resonances both in open loop and closed loop and which are reported for the first time in this study.

6.2 Thesis Publications

6.2.1 Journal papers

1. **S. Towfighian**, G. R. Heppler, E. M. Abdel- Rahman, “Analysis of a chaotic electrostatic Micro-oscillator”. *Journal of Computational and Nonlinear Dynamics*, January

2011, Volume 6, Issue 1, 011001 (10 pages).

2. A. Seleim, **S. Towfighian**, E. Delande, E. M. Abdel- Rahman, G. R. Heppler, “Dynamic Analysis of a Close-Loop Controlled Chaotic MEMS Resonator”, *Journal of Nonlinear Dynamics*, Submitted, June 2010.
3. **S. Towfighian**, A. Seleim, E. M. Abdel- Rahman, G. R. Heppler, “A Low-Frequency large travel-range electrostatic micro-actuator”, *Journal of Micromechanics and Microengineering*, Submitted, January 2011.

6.2.2 Conference papers

1. **S. Towfighian**, E. Abdel- Rahman, G. R. Heppler, “Simulation of the Static Response of a Chaotic Micro-actuator”, *Engineering Science and Mechanics Conference*, Blacksberg, VA, May 2008.
2. **S. Towfighian**, E. M. Abdel-Rahman, and G. R. Heppler, “Static and dynamic analysis of a bi-stable micro-actuator”, IMECE2008-67553, *Proceedings of ASME International Mechanical Engineering Congress and Exposition*, Nov. 2008, Boston, MA, USA, pp. 1-11.
3. **S. Towfighian**, G. R. Heppler, E. M. Abdel- Rahman, “Quadratic controller for a chaotic micro-resonator”, *Proceedings of Microsystems and Nanoelectronics Research Conference (MNRC 2nd)*, Oct. 2009, Ottawa, Canada, pp. 69-72.
4. **S. Towfighian**, A. Seleim, E. M. Abdel- Rahman, G. R. Heppler, “Experimental validation for an extended stability electrostatic actuator”, DETC2010-28983, *Proceedings of the ASME 2010 International Design Engineering Technical Conferences*, Aug. 2010, Montreal, Canada.
5. **S. Towfighian**, G. R. Heppler, E. M. Abdel- Rahman, “A low voltage controller for a chaotic micro resonator”, DETC2010-28990, *Proceedings of the ASME 2010 International Design Engineering Technical Conferences*, Aug. 2010, Montreal, Canada.

6.3 Future Work

Future work to extend the research in this thesis should include

- Extending the mathematical model for the electrostatic actuator to include the squeeze-film damping effect.
- Implementing the two proposed chaotic resonators using control circuits similar to those described in Chapter 4.
- Converting the superharmonic resonances of the large-stroke actuator in Chapter 4 to chaotic oscillation by using the high-frequency controller.
- using the metrics of chaos such as Lyapunov exponents, and information entropy for the chaotic resonator in mass sensing applications.
- Applying the large-stroke electrostatic actuators developed in this thesis to optical filters, optical modulators, and AFM probes.

APPENDICES

Appendix A

Publisher Permission

The following letters are the permissions obtained from ASME for including the published papers in this PhD thesis.

FW: ASME PUBLICATIONS PERMISSION REQUEST FORM SUBMISSION

Beth Darchi <DarchiB@asme.org>

Thu, Jan 13, 2011 at 11:48 AM

To: "sh.towfighian@gmail.com" <sh.towfighian@gmail.com>

Dear Mr. Towfighian:

It is our pleasure to grant you permission to use ASME paper "STATIC AND DYNAMIC ANALYSIS OF A BISTABLE MICRO-ACTUATOR," by S. Towfighian, E. M. Abdel-Rahman, and G. R. Heppler, Paper Number MECE2008-67553, cited in your letter for inclusion in a Doctoral Thesis entitled [A Large-Stroke Electrostatic Micro-Actuator](#) to be published by University of Waterloo.

As is customary, we ask that you ensure full acknowledgment of this material, the author(s), source and ASME as original publisher on all printed copies being distributed.

Many thanks for your interest in ASME publications.

Sincerely,

Beth Darchi

Permissions & Copyrights

ASME, 3 Park Avenue

New York, NY 10016

T: 212-591-7700

F: 212-591-7841

E: darchib@asme.org

REVISED: FW: ASME PUBLICATIONS PERMISSION REQUEST

Beth Darchi <DarchiB@asme.org>

Fri, Jan 14, 2011 at 2:56 PM

To: Shahrzad Towfighian <sh.towfighian@gmail.com>

Dear Mr. Towfighian:

It is our pleasure to grant you permission to use ASME paper "Analysis of a chaotic electrostatic Micro-oscillator," by S. Towfighian, G. R. Heppler, E. M. Abdel- Rahman, Journal of Computational and Nonlinear Dynamics, Volume 6, Issue 1, 2011, cited in your letter for inclusion in a Doctoral Thesis entitled A Large-Stroke Electrostatic Micro-Actuator to be published by University of Waterloo.

As is customary, we ask that you ensure full acknowledgment of this material, the author(s), source and ASME as original publisher on all printed copies being distributed.

Many thanks for your interest in ASME publications.

Sincerely,

Beth Darchi
Permissions & Copyrights
ASME, 3 Park Avenue
New York, NY 10016
T: 212-591-7700
F: 212-591-7841
E: darchib@asme.org

References

- [1] S. Liu, A. Davidson, and Q. Lin. Simulation studies on nonlinear dynamics and chaos in a MEMS cantilever control system. *Journal of Micromechanics and Microengineering*, 14(7):1064–1073, 2004.
- [2] E. S. Hung. *Positioning, control, and dynamics of electrostatic actuators for use in optical and RF systems*. PhD thesis, Massachusetts Institute of Technology, 1998.
- [3] S. Chung. Design and fabrication of 10×10 micro-spatial light modulator array for phase and amplitude modulation. *Sensors and Actuators A: Physical*, 78(1):63–70, 1999.
- [4] E.S. Hung and S. D. Senturia. Extending the travel range of analog-tuned electrostatic actuators. *Journal of Microelectromechanical Systems*, 8(4):497–505, 1999.
- [5] S. H. Strogatz. *Nonlinear dynamics and Chaos : with applications in physics, biology, chemistry, and engineering*. Westview Press, USA, 1994.
- [6] L. N. Virgin, T. C. Lyman, and R. B. Davis. Nonlinear dynamics of a ball rolling on a surface. *American Journal of Physics*, 78(3):250, 2010.
- [7] B. I. Epureanu, L. S. Tang, and M. P. Paidoussis. Exploiting chaotic dynamics for detecting parametric variations in aeroelastic systems. *AIAA Journal*, 42(4):728–735, 2004.
- [8] A. Seleim. “private communications”, 2010.
- [9] M. S.-C. Lu and G. K. Fedder. Position control of parallel-plate microactuators for probe-based data storage. *Journal of Microelectromechanical Systems*, 13(5):759–769, Oct. 2004.

- [10] F. Sugihwo, M.C. Larson, and J. S. Harris. Micromachined widely tunable vertical cavity laser diodes. *Journal of Microelectromechanical Systems*, 7(1):48–55, 1998.
- [11] B. Borovic, C. Hong, A. Q. Liu, L. Xie, and F. L. Lewis. Control of a MEMS optical switch. In *43rd IEEE Conference on Decision and Control (CDC)*, Nassau, Bahamas.
- [12] R. L. Knipe. Challenges of a digital micromirror device: modeling and design. In *Proceedings of the SPIE - The International Society for Optical Engineering*, volume 2783, pages 135–145, Besancon, France, 1996.
- [13] P. F. Van Kessel, L. J. Hornbeck, R. E. Meier, and M. R. Douglass. A MEMS-based projection display. 86(8):1687–1704, 1998.
- [14] M.R. Douglass. A surface micromachined miniature switch for telecommunications applications with signal frequencies from dc to 4 ghz. In *Proceedings of the 36th IEEE International Reliability Physics Symposium*, Reno, Nevada.
- [15] P. Vettiger, G. Cross, M. Despont, U. Drechsler, U. Durig, B. Gotsmann, W. Haberle, M. A. Lantz, H.E. Rothuizen, R. Stutz, and G.K. Binnig. The “millipede“ - nanotechnology entering data storage. *IEEE Transactions On Nanotechnology*, 1(1):39–55, 2002.
- [16] J. J. Yao and M. F. Chang. A surface micromachined miniature switch for telecommunications applications with signal frequencies from dc to 4 ghz. In *The 8th International Conference on Solid-State Sensors and Actuators and Eurosensors IX.*, Stockholm, Sweden.
- [17] E.K. Chan and R. W. Dutton. Electrostatic micromechanical actuator with extended range of travel. *Journal of Microelectromechanical Systems*, 9(3):321–328, 2000.
- [18] R. Guardia, A. Dehe, R. Aigner, and L. M. Castaner. Current drive methods to extend the range of travel of electrostatic microactuators beyond the voltage pull-in point. *Journal of Microelectromechanical Systems*, 11(3):255–263, 06 2002.
- [19] S.-H. Yin and B.I. Epureanu. Experimental enhanced nonlinear dynamics and identification of attractor morphing modes for damage detection. *Journal of Sound and Acoustics*, 129(6):763–770, Dec. 2007.

- [20] M. I. Younis and F. Alsaleem. Exploration of new concepts for mass detection in electrostatically-actuated structures based on nonlinear phenomena. *Journal of Computational and Nonlinear Dynamics*, 4(2):021010–1–15, 2009.
- [21] D. H. S. Maithripala, J. M. Berg, and W. P. Dayawansa. Control of an electrostatic microelectromechanical system using static and dynamic output feedback. *Transactions of the ASME. Journal of Dynamic Systems*, 127(3):443–450, 09 2005.
- [22] J. I. Seeger and B. E. Boser. Charge control of parallel-plate, electrostatic actuators and the tip-in instability. *Journal of Microelectromechanical Systems*, 12(5):656–671, 10 2003.
- [23] J. Chen, W. Weingartner, A. Azarov, and R. C. Giles. Tilt-angle stabilization of electrostatically actuated micromechanical mirrors beyond the pull-in point. *Journal of Microelectromechanical Systems*, 13(6):988–997, 2004.
- [24] C. G. Agudelo, M. Packirisamy, G. Zhu, and L. Saydy. Nonlinear control of an electrostatic micromirror beyond pull-in with experimental validation. *Journal of Microelectromechanical Systems*, 18(4):914–923, 2009.
- [25] Y. Zhao, E H T. Francis, F. C. Siong, and G. Zhou. Stabilization of dual-axis micromirrors beyond the pull-in point by integral sliding mode control. *Journal of Micromechanics and Microengineering*, 16(7):1242–1250, July 2006.
- [26] D. Piyabongkarn, Y. Sun, R. Rajamani, A. Sezen, and B. J. Nelson. Travel range extension of a MEMS electrostatic microactuator. *IEEE Transactions on Control Systems Technology*, 13(1):138–145, 01 2005.
- [27] K. O. Owusu and F. L. Lewis. Solving the "pull-in" instability problem of electrostatic microactuators using nonlinear control techniques. In *2nd IEEE International Conference on Nano/Micro Engineered and Molecular Systems*, Bangkok, Thailand, Jan. 2007.
- [28] Mohammad Nikpanah, Youyi Wang, Frank Lewis, and Ai Liu. Real time controller design to solve the pull-in instability of MEMS actuator. In *10th International Conference on Control, Automation, Robotics and Vision*, Hanoi, Vietnam, Dec 2008.

- [29] D. H. S. Maithripala, B. D. Kawade, J. M. Berg, and W. P. Dayawansa. A general modelling and control framework for electrostatically actuated mechanical systems. *International Journal of Robust and Nonlinear Control*, 15(16):839–857, 11 2005.
- [30] F.C. Moon. *Chaotic and Fractal Dynamics*. Wiley–Interscience Publication, New York, 1992.
- [31] P. J. Holmes. A nonlinear oscillator with a strange attractor. *Phil. Trans. Roy. Soc. London*, A292:419–448, 1979.
- [32] F. C. Moon and P. J. Holmes. A magnetoelastic strange attractor. *Journal of Sound and Vibration*, 65(2):275–296, 1979.
- [33] B.I. Epureanu and S.-H. Yin. Identification of damage in an aeroelastic system based on attractor deformations. *Computers & Structures*, 82(31–32):2743–51, Dec. 2004.
- [34] B. I. Epureanu, S. H. Yin, and M. M. Derriso. High-sensitivity damage detection based on enhanced nonlinear dynamics. *Smart Materials and Structures*, 14(2):321–327, April 2005.
- [35] S. Ghafari. *A Fault Diagnosis System for Rotary Machinery Supported by Rolling Element Bearings*. PhD thesis, University of Waterloo, 2007.
- [36] K.M. Cuomo, A.V. Oppenheim, and S.H. Strogatz. Synchronization of lorenz-based chaotic circuits with applications to communications. In *IEEE Transactions on Circuits and Systems II: Analog and Digital Signal Processing*, volume 40, pages 626–633, Oct. 1993.
- [37] A. Hashmi and B.I. Epureanu. Sensitivity resonance and attractor morphing quantified by sensitivity vector fields for parameter reconstruction. *Nonlinear Dynamics*, 45(3–4):319–335, 2006.
- [38] K. Park, Q. Chen, and Y.C. Lai. Energy enhancement and chaos control in micro-electromechanical systems. *Physical Review*, 77:026210–1–6, 2008.
- [39] S.D. Senturia. *Microsystems Design*. Kluwer Academic Publishers, Boston, 2001.

- [40] J. R. Gilbert, R. Legtenberg, and S.D. Senturia. 3D coupled electro-mechanics for MEMS: applications of CoSolve-EM. In *Proceedings of the IEEE Micro Electro Mechanical Systems (MEMS)*, pages 122–127, Amsterdam, Neth., 1995.
- [41] E. K. Chan, K. Garikipati, and R. W. Dutton. Characterization of contact electromechanics through capacitance-voltage measurements and simulations. *Journal of Microelectromechanical Systems*, 8(2):208–217, 1999.
- [42] P. M. Zavracky, S. Majumder, and N. E. McGruer. Micromechanical switches fabricated using nickel surface micromachining. *Journal of Microelectromechanical Systems*, 6(1):3–9, March 1997.
- [43] A. C. J. Luo and F. Y. Wang. Chaotic motion in a micro-electro-mechanical system with non-linearity from capacitors. *Communications in Nonlinear Science and Numerical Simulation*, 7(1-2):31–49, 2002.
- [44] Y. Zhang and Y. Zhao. Numerical and analytical study on the pull-in instability of micro-structure under electrostatic loading. *Sensors and Actuators, A (Physical)*, 127(2):366–380, 2006.
- [45] M. I. Younis, E.M. Abdel-Rahman, and A. H. Nayfeh. A reduced-order model for electrically actuated microbeam-based MEMS. *Journal of Microelectromechanical Systems*, 12(5):672–680, October 2003.
- [46] E. Buks and B. Yurke. Mass detection with a nonlinear nanomechanical resonator. *Physical Review E*, 74(4):46619–461–9, Oct. 2006.
- [47] W.G. Conley, A. Raman, C. M. Krousgrill, and S. Mohammadi. Nonlinear and non-planar dynamics of suspended nanotube and nanowire resonators. *Nano Letters*, 8(6):1590–1595, 2008.
- [48] Q. Chen, L. Huang, Y. C. Lai, C. Grebogi, and D. Dietz. Extensively chaotic motion in electrostatically driven nanowires and applications. *Nano letters*, 10(2):406–413, Feb. 2010.
- [49] M. Basso, L. Giarré, M. Dahleh, and I. Mezic. Numerical analysis of complex dynamics in atomic force microscopes. In *Proceedings of IEEE International Conference on control Applications*, pages 1026–1030, Trieste, Italy, Sep. 1998.

- [50] M. Ashhab, M.V. Salapaka, M. Dahleh, and I. Mezic. Melnikov-based dynamical analysis of microcantilevers in scanning probe microscopy. *Nonlinear Dynamics*, 20(3):197–220, Nov. 1999.
- [51] M. Ashhab, M.V. Salapaka, M. Dahleh, and I. Mezic. Dynamical analysis and control of microcantilevers. *Automatica*, 35(10):1663–1670, Nov. 1999.
- [52] S. I. Lee, S. W. Howell, A. Raman, and R. Reifenberger. Nonlinear dynamics of microcantilevers in tapping mode atomic force microscopy: A comparison between theory and experiment. *Physical Review B (Condensed Matter and Materials Physics)*, 66(11):115409/1–10, 09 2002.
- [53] A. Raman and S. Hu. Chaos in dynamic atomic force microscopy. In *2006 International Symposium on Nonlinear Theory and its Applications*, pages 911–14, Bologna, Italy, 2006.
- [54] F. Jamitzky, M. Stark, W. Bunk, W.M. Heckl, and R.W. Stark. Chaos in dynamic atomic force microscopy. *Nanotechnology*, 17(7):S213–S220, Apr 2006.
- [55] J. Bienstman, J. Vandewalle, and R. Puers. Autonomous impact resonator: A new operating principle for a silicon resonant strain gauge. *Sensors and Actuators, A (Physical)*, 66(1-3):40–49, 1998.
- [56] Y. C. Wang, S. G. Adams, J. S. Thorp, N. C. MacDonald, P. Hartwell, and F. Bertsch. Chaos in MEMS, parameter estimation and its potential application. *IEEE Transactions on Circuits and Systems I: Fundamental Theory and Applications*, 45(10):1013–1020, 1998.
- [57] S. K. De and N.R. Aluru. Complex nonlinear oscillations in electrostatically actuated microstructures. *Journal of Microelectromechanical Systems*, 15(2):355–369, Apr. 2006.
- [58] B.E. DeMartini, H.E. Butterfield, J. Moehlis, and K.L. Turner. Chaos for a microelectromechanical oscillator governed by the nonlinear mathieu equation. *Journal of Microelectromechanical Systems*, 16(6):1314–1323, 2007.

- [59] Y. Zhang, Y. S. Wang, Z. H. Li, Y. B. Huang, and D. C. Li. Snap-through and pull-in instabilities of an arch-shaped beam under an electrostatic loading. *Journal of Microelectromechanical Systems*, 16(3):684–693, 2007.
- [60] S. Krylov. Lyapunov exponents as a criterion for the dynamic pull-in instability of electrostatically actuated microstructures. *International Journal of Non-Linear Mechanics*, 42(4):626–642, 2007.
- [61] S. Krylov, B. R. Ilic, D. Schreiber, S. Seretensky, and H. Craighead. The pull-in behavior of electrostatically actuated bistable microstructures. *Journal of Micromechanics and Microengineering*, 18(5):1–20, May 2008.
- [62] K. Das and R. C. Batra. Pull-in and snap-through instabilities in transient deformations of microelectromechanical systems. *Journal of Micromechanics and Microengineering*, 19(3):1–19, 20090101 2009.
- [63] Jeffrey F. Rhoads, Steven W. Shaw, Jeff Moehlis, Barry E. Demartini, Kimberly L. Turner, and Wenhua Zhang. Nonlinear response of parametrically-excited mems. In *DETC2005: ASME International Design Engineering Technical Conferences and Computers and Information in Engineering Conference*, volume 1 A, pages 453–461, 2005.
- [64] W-M Zhang and G. Meng. Nonlinear dynamic analysis of electrostatically actuated resonant mems sensors under parametric excitation. *IEEE Sensors Journal*, 7(3):370–380, 03 2007.
- [65] T. Saif. On a tunable bistable MEMS: Theory and experiment. *Journal of Microelectromechanical Systems*, 9(2):157–170, June 2000.
- [66] M. Sulfridge, T. Saif, N. Miller, and M. Meinhart. Nonlinear dynamic study of a bistable MEMS: Model and experiment. *Journal of Microelectromechanical Systems*, 13(5):725–731, October 2004.
- [67] S. Towfighian, G. R. Heppler, and E. M. Abdel-Rahman. Analysis of a chaotic electrostatic micro-oscillator. *Journal of Computational and Nonlinear Dynamics*, 6(1):011001–10, Jan 2011.

- [68] A. H. Nayfeh, M. L. Younis, and E. M. Abdel-Rahman. Reduced-order models for MEMS applications. *Nonlinear Dynamics*, 41(1-3):211–236, August 2005.
- [69] A.H. Nayfeh, M.I. Younis, and E.M. Abdel-Rahman. Dynamic pull-in phenomenon in mems resonators. *Nonlinear Dynamics*, 48(1–2):153–63, Apr. 2007.
- [70] F. Najjar, A. H. Nayfeh, E. M. Abdel-Rahman, S. Choura, and S. El-Borgi. Nonlinear analysis of mems electrostatic microactuators: Primary and secondary resonances of the first mode. *submitted to Journal of Vibration and Control*, 2008.
- [71] A. Seleim. Design and implementation of a controller for an electrostatic MEMS actuator and sensor. Master’s thesis, University of Waterloo, 2010.
- [72] S. Towfighian, A. Seleim, E. M. Abdel-Rahman, and G. R. Heppler. Experimental validation for an extended stability electrostatic actuator. In *Proceedings of the ASME 2010 International Design Engineering Technical Conferences*, pages DETC2010–28983, Montreal, QC, Canada, 2010.
- [73] *Polytec scanning Vibrometer: theory manual*, 2008.
- [74] S. Towfighian, G. R. Heppler, and E. M. Abdel-Rahman. A low voltage controller for a chaotic micro resonator. In *Proceedings of the ASME 2010 International Design Engineering Technical Conferences*, pages DETC2010–28990, Montreal, QC, Canada, 2010.
- [75] F. C. Moon. *Chaotic Vibrations: An Introduction for Applied Scientists and Engineers*. A Wiley-Interscience publication, New York, 1987.